T H E U N I V E R S I T Y O F M I C H I G A N

COLLEGE OF ENGINEERING
Department of Aeronautical and Astronautical Engineering

Final Technical Report

A SIMPLIFIED FALLING-SPHERE METHOD FOR UPPER-AIR DENSITY PART II. DENSITY AND TEMPERATURE RESULTS FROM EIGHT FLIGHTS

J. W. Peterson
H. F. Schulte
E. J. Schaefer

Approved: L. M. Jones

UMRI Project 2215

under contract with:

DEPARTMENT OF THE AIR FORCE
AIR FORCE CAMBRIDGE RESEARCH CENTER
GEOPHYSICS RESEARCH DIRECTORATE
M/F CONTRACT NO. AF 19(604)-999
and
NATIONAL SCIENCE FOUNDATION GRANT Y/10.20/249

administered by:

THE UNIVERSITY OF MICHIGAN RESEARCH INSTITUTE ANN ARBOR

May 1959

TABLE OF CONTENTS

	Page
LIST OF TABLES	v
LIST OF FIGURES	vi
ABSTRACT	x
THE UNIVERSITY OF MICHIGAN PROJECT PERSONNEL	xi
1. INTRODUCTION	1
2. SPHERE	2
2.1. Sphere Balance	2
2.2. Intervalometer and Accelerometer	3
2.3. Pulse-Forming Circuitry	4
2.4. Pulse Modulator	5
2.5. Transmitter	6
2.6. Sphere Antenna	8
2.7. Power Supplies and Control Circuits	9
3. NOSE CONE	10
4. TELEMETERING GROUND STATION	10
4.1. Antennas	11
4.2. RF Pre-amplifiers	12
4.3. Receivers	12
4.4. Pulse Chassis	12
4.5. Timing Signals	14
4.6. Data Recorders	14
5. FLIGHT-DATA PLAYBACK SYSTEM	15
6. FLIGHT-SIGNAL-STRENGTH DATA	16
7. DATA REDUCTION AND RESULTS	17
7.1. Data Analysis Procedures	18
7.2. Results	21
7.3. Sources of Error	21
7.4. Data Quality	23

TABLE OF CONTENTS (Concluded)

	Page
8. RECOMMENDATIONS	25
9. ACKNOWLEDGMENTS	25
APPENDIX I. Trajectory Analysis Equations	26
APPENDIX II. Effect of Accelerometer Error on the Trajectory Analysis	29
REFERENCES	30

LIST OF TABLES*

I	Data on Spheres and Accelerometers
II	Flights of Small-Sphere Experiment
III	Results of AM 6.01
IV	Results of AM 6.09
V	Results of AM 6.10
VI	Results of AM 6.12
VII	Results of AM 6.02
VIII	Results of SM 2.10
IX	Results of AM 6.03
X	Results of AM 6.05
XI	Summary of Accelerometer Error Calculations

*Tables and figures appear at end of report.

LIST OF FIGURES*

1. Photographs of sphere with slot antenna.
2. Construction of sphere
3. Block diagram of sphere experiment.
4. Schematic of sphere circuitry.
5. Transmitter schematic
6. Photograph of transmitter.
7. Sphere antenna.
8. Sphere-antenna radiation pattern.
9. Sphere-antenna radiation pattern.
10. Antenna test tower.
11. Nose-cone assembly.
12. Photograph of sphere in support structure.
13. Photograph of assembled nose cone.
14. Schematic of sphere-ejection system in nose cone.
15. Ejection timer and circuit (bottom side).
16. Ejection timer and circuit (top side).
17. Photograph of ground station.
18. Ground antenna.
19. Ground-antenna radiation pattern.
20. Ground-antenna radiation pattern.

*Tables and figures appear at end of report.

LIST OF FIGURES

21. Pre-amplifier.

22. Modification of receiver circuit.

23. Pulse-chassis schematic.

24. Block diagram of flight-data playback system.

25. Section of typical Brush record.

26. Signal strength vs. time and altitude (AM 6.02).

27. Velocity, Mach number, drag acceleration, and density vs. time and altitude (AM 6.02).

28. Signal strength vs. time and altitude (SM 2.10).

29. Velocity, Mach number, drag acceleration, and density vs. time and altitude (SM 2.10).

30. Signal strength vs. time and altitude (AM 6.03).

31. Velocity, Mach number, drag acceleration, and density vs. time and altitude (AM 6.03).

32. Signal strength vs. time and altitude (AM 6.05).

33. Velocity, Mach number, drag acceleration, and density vs. time and altitude (AM 6.05).

34. Drag acceleration vs. time used to obtain peak time (AM 6.01).

35. Drag acceleration vs. time used to obtain peak time (AM 6.09).

36. Drag acceleration vs. time used to obtain peak time (AM 6.10).

37. Drag acceleration vs. time used to obtain peak time (AM 6.12).

38. Drag acceleration vs. time used to obtain peak time (AM 6.02).

39. Drag acceleration vs. time used to obtain peak time (SM 2.10).

40. Drag acceleration vs. time used to obtain peak time (AM 6.03).

41. Drag acceleration vs. time used to obtain peak time (AM 6.05)

42. Sphere and radiosonde densities compared (AM 6.01).

43. Sphere and radiosonde densities compared (AM 6.09).

44. Sphere and radiosonde densities compared (AM 6.10).

45. Sphere and radiosonde densities compared (AM 6.12).

46. Sphere and radiosonde densities compared (AM 6.02).

47. Sphere and radiosonde densities compared (SM 2.10).

48. Sphere and radiosonde densities compared (AM 6.03).

49. Sphere and radiosonde densities compared (AM 6.05).

50. C_D as a function of Mach number and Reynolds number.

51. Empirical drag coefficient functions.

52. Ambient density vs. altitude (AM 6.01).

53. Ambient density vs. altitude (AM 6.09).

54. Ambient density vs. altitude (AM 6.10).

55. Ambient density vs. altitude (AM 6.12).

56. Ambient density vs. altitude (AM 6.02).

57. Ambient density vs. altitude (SM 2.10).

58. Ambient density vs. altitude (AM 6.03).

59. Ambient density vs. altitude (AM 6.05).

60. Ambient temperature vs. altitude (AM 6.01).

61. Ambient temperature vs. altitude (AM 6.09).

62. Ambient temperature vs. altitude (AM 6.10).

LIST OF FIGURES (Concluded)

63. Ambient temperature vs. altitude (AM 6.12).

64. Ambient temperature vs. altitude (AM 6.02).

65. Ambient temperature vs. altitude (SM 2.10).

66. Ambient temperature vs. altitude (AM 6.03).

67. Ambient temperature vs. altitude (AM 6.05).

68. Typical sphere trajectories compared with vacuum trajectories.

ABSTRACT

The development and use of the small-sphere method for synoptic measurement of upper-air density and temperature is described. The results from flights carried out during the IGY program are given.

THE UNIVERSITY OF MICHIGAN PROJECT PERSONNEL
(Both Full-Time and Part-Time)

Allen, Harold F., Ph.D., Research Engineer
Bartman, Frederick L., M.S., Research Engineer
Filsinger, Edward A., Instrument Maker
Finkbeiner, Richard G., Electronic Technician
Fischbach, Frederick F., B.S., Research Associate
Gleason, Kermit L., Instrument Maker
Hansen, William H., B.S., Research Engineer
Harrison, Lillian M., Secretary
Harwit, Martin O., M.S., Research Assistant
Henry, Harold F., Electronic Technician
Howe, Carl E., Ph.D., Assistant in Research
Jew, Howard, M.A., Research Assistant
Jones Leslie M., B.S., Project Supervisor
Kimel, Harry W., Jr., Technician
Liu, V. C., Ph.D., Research Engineer
Malkani, Sundru J., M.S., Assistant in Research
Otterman, Joseph, Ph.D., Research Engineer
Pattinson, Theodore R., Electronic Technician
Peterson, John W., M.S., Research Associate
Reddy, Gopal K., M.S., Assistant in Research
Robinson, Douglas A., Technician
Samborski, Cassimere, Instrument Maker
Schaefer, Edward J., M.S. Research Engineer
Schulte, Hal F., Jr., M.S.E., Associate Research Engineer
Speake, Neal McC., M.S., Assistant in Research
Titus, Paul A., B.S., Research Associate
Wenk, Norman J., B.S., Research Engineer
Whybra, Melvin G., M.A., Technician

1. INTRODUCTION

This is the final report of a project carried on in the Department of Aeronautical and Astronautical Engineering of The University of Michigan, the purpose of which was to develop and use a simplified falling-sphere method for measuring upper-air density and temperature on a synoptic basis. Density (and hence temperature) are calculated by means of the drag equation applied to a free-falling sphere which contains an omni-directional accelerometer. The sphere is ejected from a Nike-Cajun rocket at approximately 35 miles altitude during the up-leg portion of its trajectory. Its velocity is sufficient to attain a peak altitude of about 100 miles. For background the reader is referred to Technical Report No. 2215-10-T, June, 1956,[1] of this contract, which describes the first version of the small-sphere experiment including the aerodynamics of the method, the accelerometer, rocket, ground station, etc. In the present report those items which were used in later flights with only minor modifications are not described again. The major modifications were in the electronics of the sphere-to-ground-station telemeter system which arose from the decision to use a pulse-position (time) code modulation for telemetering the accelerometer data. In this method a 10-μsec, 400-Mc pulse with a peak power of about 32 watts is transmitted at the instant the accelerometer bobbin is released, and a second such pulse is transmitted at the instant of bobbin contact. The pulses are received and recorded along with an accurate time-base on multichannel magnetic tape at the ground station. The pulse system permits direct playback of the recorded telemetered data into electronic counters for display of the accelerometer times.

Ten flights of the new version of the small-sphere experiment were carried out as part of the IGY or pre-IGY program of the U. S. National Committee for the International Geophysical Year. These are summarized in a table in the report. Financial support for the sphere work was derived primarily from AFCRC; however, some support during the program was also received from the National Science Foundation.

The first (non-IGY) tests of the sphere experiment used the Nike-Deacon rocket described in the first report. Ten IGY firings used the Nike-Cajun rocket (in addition to which one sphere was carried in Aerobee SM2.10). For a description of this vehicle, the reader is referred to a report entitled The Nike-Cajun Sounding Rocket.[2]

Preliminary results and a brief discussion of the sphere measurements were presented at the 5th Reunion of CSAGI in Moscow in August, 1958.[3]

Some refinements of the sphere experiment in the direction of extending the accelerometer range and computerizing data reduction are being carried out on Air Force Contract No. AF 19(604)-2415.

2. SPHERE

Although the 7-in.-diameter sphere (described in Ref. 1) was retained, a number of design modifications were made to accommodate the pulse-type telemetering system. The most significant physical change was the adoption of a flush-mounted boxed-in slot antenna in place of the equatorial ring formerly used to insulate the two sphere halves, which acted as a type of dipole antenna. Figures 1 and 2 show details of the sphere components and assembly. The equatorial center section, which contains the slot antenna, is fabricated of dural with a Teflon fairing covering the antenna aperture for aerodynamic smoothness.

The sphere is pressurized as before with Neoprene O-rings placed between the sphere halves, at the two poles, the pressurizing port, the battery monitor plug, and the electrical function switch. Since the antenna itself is vented to the atmosphere, a pressurized coaxial fitting provides antenna feed from the internal transmitter and maintains sphere pressure integrity.

Table I is a summary of various characteristics of all the spheres and accelerometers constructed for the program.

2.1. SPHERE BALANCE

The error in acceleration as measured by the accelerometer which is caused by an initial velocity on release of the bobbin is given by

$$\delta a_{v_o} = 200\ v_o/at^2 \qquad (1)$$

where

δa_{v_o} = % error in acceleration due to v_o
v_o = initial velocity
a = acceleration
t = time

If the bobbin is not centered on the center of rotation of the falling, spinning sphere, an initial velocity $v_o = \omega r$ will be imparted to the bobbin because of spin (ω = spin rate and r = displacement of the bobbin center from the center of rotation). It is assumed that the falling sphere will rotate about its center of gravity. In the presence of large aerodynamic forces this may not be an accurate assumption, but a compensating factor is that the effect of initial velocity is reduced at large accelerations. For the transit distance

used in these accelerometers (3/16 in.), at 0.01 g there will be a maximum error of 1% in acceleration per rps per 0.001 in. of center displacement.

The method of measuring sphere balance is described in the previous report. The results for all spheres are shown in Table I. Sphere B of rocket DAN 2 was measured but not corrected. Although it was rather poorly balanced, the scatter in the upper-air data was small. This was probably due to a low spin rate. The spheres used in the Rushmore firings were balanced reasonably well about 3 axes. The spheres used in the Churchill firings were balanced quite well about the axis parallel to the rocket spin axis and reasonably well about all axes. The latter two groups of spheres had scatter in the upper-air data ranging from little to much and this is presumably attributable to spin rate. The balancing weights used in one of the Churchill spheres are seen in Figs. 1c and 1d.

2.2. INTERVALOMETER AND ACCELEROMETER

The complete falling-sphere instrumentation system is shown in block-diagram form in Fig. 3. The intervalometer in the upper left-hand corner consists of a 6-volt d-c gear-reduction motor (Globe Industries Type MM-24-83F) with an output shaft speed of approximately 0.9 rpm. A cam on the motor shaft closes a set of normally open contacts for approximately 150 millisec once each shaft revolution. During flight, this switch closure energizes the accelerometer "pick-up fingers" which position the bobbin in the center of the accelerometer cavity. When the contacts open, a large counter emf caused by the collapsing magnetic field appears across the switch contacts. This voltage pulse, which constitutes the accelerometer "start pulse," is capacitively coupled into the pulse-forming circuitry which is discussed in the next section. As the magnetic field decays, the positioning fingers are rapidly accelerated away from the bobbin, and it is free to accelerate to the cavity wall. Electrical contact is maintained with the bobbin by two 0.001-in.-diameter gold "cat's whisker" wires which exert negligible restraining force on the bobbin. When the bobbin first contacts the cavity wall, it closes a circuit which generates the "stop pulse." This procedure is repeated once each 0.9 sec by the intervalometer.

The accelerometers used in the flights of this report were essentially the same as the one described in the previous report. Tests were carried out at 1 g, approximately 0.01 g, and approximately 5 g. At 1 g the local value for gravity is known. Approximately 0.01 g is applied to the accelerometer by attaching it to a heavy streamlined bullet and allowing the two to fall with a small retarding force being applied by means of an attached thread which is wrapped around a low-friction pulley whose moment of inertia is known. Approximately 5 g are applied by means of a centrifuge. The various means of checking the accelerometers were described in the first report.[1] Excellent agreements ($\approx 0.5\%$) between the accelerations measured by the accelerometers and those calculated as being applied by the testing method were obtained at 1 g and 5 g. In the case of the low accelerations (≈ 0.01 g) the discrepancies are as high as 8%. This figure does not, however, necessarily represent error

in the accelerometer. Some difficulty was experienced in keeping the pulley free of friction in the low-acceleration tests and it is thought that the discrepancies are more apt to be in the testing method than in the accelerometers. The results of the accelerometer tests are given in Table I. At each of three accelerations ("ONE G," "LOW ACCEL," "HIGH ACCEL") there are three values: in the first column is the acceleration as measured by the accelerometer; in the second, the acceleration as measured (and applied) by the testing method; and in the third, the difference between the two.

The precision indices in the table are as follows:

(1) In all columns marked "ACCEL" the precision indices are standard deviations in an average of 13 tries (not less than 5, not more than 20) to measure with the accelerometer the accelerations applied to it.

(2) In the column "ONE G, METHOD" it is assumed that the acceleration of gravity is known without error. Systematic errors in the accelerometers are obtained by comparing the "ACCEL" column with the "METHOD" column.

(3) In the column "LOW ACCEL, METHOD" the precision indices shown are standard deviations propagated by error theory through the equations relating the acceleration to the moment of inertia of the pulley. The precision index for the moment of inertia is a standard deviation calculated from the standard deviations in measuring the times in the "small mass" method for moment of inertia. See the previous report.[1]

(4) In the column "HIGH ACCEL, METHOD" the precision indices are standard deviations propagated by error theory through the equations relating the acceleration to the centrifuge factors, i.e., length of arm, speed of rotation, error in readings. The latter precision indices are again standard deviations.

2.3. PULSE-FORMING CIRCUITRY

Figure 4 is a diagram of all pulse, control, and power-supply circuits contained in the sphere. The pulse-forming circuitry section is enclosed within the dotted-line section labeled "thyratron board" in the upper left-hand section of the figure. The start and stop pulses referred to above are coupled into this section by capacitors C_8 and C_1, respectively.

V_1 and V_2 are two subminiature type 5643 tetrode thyratrons used to generate the trigger pulses for the pulse-modulator tube V_3. The need for V_1 and V_2 is apparent when the character of the input signals to them is considered. The start pulse is a positive-going pulse of approximately 75 volts amplitude. This causes V_2 to conduct and discharge C_2 through the 22-K common cathode resistor R_4. The cathode quickly rises to approximately B+ potential, and this positive-going pulse is differentiated by C_3 and R_7 and applied to the grid of V_3. The 1-megohm resistor R_5 in the plate of V_2 is so large that conduction cannot be

sustained, and thus V_2 extinguishes at the end of the interval determined by the 220-μsec R_4-C_2 time constant and the B+ voltage of 150 volts. The junction diode D_1 (Transitron type SU-18) in series with C_8 and R_6 is a voltage reference Zener diode with an operating potential of 18 volts. This diode prevents a spurious start pulse from being generated. It was observed on several occasions that, after some use, the intervalometer switch S_3 had a tendency to bounce shortly after initial closure, thus generating a pulse of 8-10 volts in amplitude. If not blocked by a diode of this type, the pulse would cause premature triggering of V_2.

During normal operation, V_1 is always in the conducting state just prior to the conduction of V_2. When V_2 fires, the cathode of V_1 is raised above its plate potential and conduction ceases. Since the grid of V_1 is returned to a negative voltage through R_2, it maintains V_1 cutoff, as its cathode potential falls to zero when V_2 extinguishes. V_1 remains cut off until the accelerometer bobbin contacts the wall of the cavity. At this point, the grid is raised to ground potential through C_1, and V_1 fires. The cathode potential rises rapidly to approximately +18 volts and remains there. The waveform is again differentiated by the C_3-R_7 combination and applied to the grid of V_3. This is the stop pulse. It will be noted that the ratio of R_3 and R_4 was chosen to maintain V_1 conducting until V_2 fires. This prevents the generation of additional stop pulses because of bobbin "bounce" which is to be expected prior to bobbin pick-up for the next cycle of operation.

One additional factor in the grid circuit of V_1 is worthy of note. It was stated above that when V_2 fires and V_1 extinguishes because of its rising cathode potential, the negative bias applied to the grid of V_1 by R_2 prevents it from refiring as its cathode voltage decays to zero. This is true only when the d-c resistance in the grid of V_1 is not too high. If R_2 is 1 megohm, for example, the small grid current that flows through R_2 during conduction allows the grid to assume cathode potential. C_1 in turn becomes charged, and, although V_1 does extinguish momentarily, when V_2 extinguishes and the cathode voltage falls, C_2 must discharge through R_2 and R_1. The net result is that the grid of V_1 becomes positive with respect to its cathode and the tube refires. Bobbin contact cannot cause a stop pulse to be transmitted now because V_1 is already conducting. Lowering R_2 to 100 K eliminates this difficulty.

2.4 PULSE MODULATOR

The pulse modulator used here is a typical radar-type pulser, using a lumped constant delay line with resonant charging accomplished by inductance L_1 and holdoff diode D_2. Thyratron V_3 acts as a switch which, when triggered by the start or stop pulse, discharges the 10-μsec delay line through the pulse transformer T_1. The 500-volt 10-μsec secondary pulse thus generated constitutes the B+ pulse voltage applied to the plates of the transmitter tubes. A typical pulse cycle can be described by considering the circuit action immediately after delay line discharge. At this time, the plate of V_3 is at

ground potential, and V_3 is extinguished. The delay line now begins to charge through L_1, D_2, and the primary of the pulse transformer T_1. The charging time is long with respect to 10 μsec because of the large inductance of L_1. When the delay line reaches B+ potential, current cannot cease instantaneously; and as the magnetic field of L_1 decays, a voltage is induced in L_1 which is approximately equal to the B+ voltage. The polarity is such that it adds to B+. Diode D_2 conducts and charges the line to approximately twice B+ voltage. The diode is now reversed biased, and further oscillations in L_1 quickly damp out. This charging cycle is completed in less than 5 millisec, at which time V_3 is again ready for triggering and discharge of the delay line. The R_8-C_4 network in the cathode of V_3 serves as a protective bias for the thyratron, so that if spurious trigger pulses do occur, V_3 will not be damaged by runaway conduction.

The delay line must operate into a load impedance equal to or somewhat less than its characteristic impedance if a reasonably flat-topped current pulse is desired at discharge. This was accomplished by first determining that the transmitter presented a load of approximately 2400 ohms to the pulse transformer secondary. This then could be transformed to any desired primary impedance which, when totaled with the conducting impedance of the thyratron, should equal 150 ohms. Since thyratron impedance is a rather sensitive function of its conduction current, it was necessary to determine the transformer primary impedance by empirical methods. The optimum value proved to be 90 ohms with V_3 unavoidably contributing approximately 60 ohms. With this combination, the thyratron current is 840 milliamp during conduction.

2.5. TRANSMITTER

The transmitter shown in Figs. 5 and 6 is a two-tube master-oscillator power amplifier operating at 400 Mc with a peak power of approximately 32 watts when operating into a matched 50-ohm resistive load. The 400-Mc carrier frequency was chosen as a compromise between efficient operation of the transmitting tubes in conventional lumped-constant circuits and efficient radiation by the sphere antenna. In addition, the region around 400 Mc has been allocated by the Federal Communications Commission for radiosonde telemetry.

Each stage of the transmitter utilizes a Raytheon type CK 5703WA premium subminiature triode vacuum tube. The oscillator is a Colpitts type, in which the capacitors forming the feedback tap on the resonant tank circuit are the tube interelectrode capacitances. The plate is operated at rf ground potential to eliminate the plate to ground capacity as a portion of the tank circuit, thus enabling operation at higher frequencies. The output power amplifier is a grounded-grid stage with approximately one-third the total output power being supplied by the oscillator. The two-stage transmitter was developed with this circuit configuration to obtain adequate power output while maintaining satisfactory isolation of antenna load variations from the oscillator frequency determining tank circuit.

Tuning and loading of the transmitter is accomplished by using a 50-ohm terminating resistance as a transmitter load and a ground station receiver for frequency measurement. Approximate values for the interstage tap point and degree of coupling between the output tank and its output coupling loop are first selected. With the transmitter in operation, the oscillator capacitor C_2 is adjusted for the desired frequency of operation. Adequate stray field is present for receiver operation. The output tank capacitor C_3 is then adjusted for maximum power output. Some "pulling" of the oscillator frequency will be noted and oscillator retuning will be necessary, but convergence is readily obtained with only two or three adjustments necessary.

It is convenient at this point to have as a transmitter load a variable step-attenuator followed by a 50-ohm coaxial thermistor mount operating into a companion power meter. By triggering the modulator stage with a 200-cps square wave and using 20 db of attenuation, a 10-μsec 50-watt peak power pulse equals 1 milliwatt average power at the thermistor. For pulses not exactly 10 μsec, appropriate changes in repetition rate can be made to compensate for width variations. With the power meter now set up to measure peak power directly, the interstage tap point and output coupling loop position is adjusted. These adjustments are a compromise between power output and frequency stability with changes in antenna impedance. In practice, it has been found that with the tap point and coupling adjusted to produce a nominal 32-watt output, frequency stability is satisfactory. This is accomplished by transferring the transmitter output to the sphere antenna, which is deliberately slightly detuned. By methodically varying the tap point and coupling, a combination can be found which produces the 32-watt output into a resistive load, yet exhibits minimum frequency shift into the reactive load. It is, of course, necessary to readjust frequency during this procedure; but this is done only when working into the resistive load.

Operational experience with the transmitter as finally developed has been very satisfactory. No difficulty with vacuum-tube failure has been encountered, even though the pulsed plate potential of 500 volts is well over the normal maximum rating. This is probably because the average plate dissipation is well below the rated limit due to the very low transmitter duty cycle of 0.00002.

During actual firing of nine of these transmitters, no instability in frequency was noted. After sphere ejection from the rocket, the initial transmission came in within less than 1 Mc of its preflight setting. Thereafter, only small drift was noted, chiefly on the down-leg during re-entry. It was observed during re-entry and its equivalent altitude on the up-leg portion of all flights, however, that a significant reduction in received signal strength occurred, centered around an altitude of approximately 220,000 ft. Records of signal strength vs. altitude and a possible explanation of this phenomenon are included in a later section on flight results.

2.6. SPHERE ANTENNA

A boxed-in slot antenna extending over half the circumference of the sphere (shown in Fig. 7) was chosen as the sphere antenna. The design was arrived at after investigation showed that the radiation efficiency of the previous dipole-type antenna operating at 217 Mc was too low. Radio-frequency losses in components located within the sphere sections and a greatly foreshortened dipole length at 217 Mc appeared to be the major causes of the difficulty.

The slot antenna uses the surface of the sphere itself as the radiating element. Since the maximum dimension of the sphere (the circumference) is approximately 3/4 of a wavelength, this type of antenna yielded best radiation efficiency. It has the additional advantage of keeping the sphere interior free of rf fields, thus eliminating the need for shielding components placed therein. The depth of the antenna slot is as great as the dimensions of the sphere and accelerometer case permit, averaging approximately one-tenth wavelength. The slot is filled with polystyrene for structural reasons and covered with a Teflon fairing for heat resistance during the re-entry portion of the flight. The fairing is machined to match the spherical surface, and thus maintains aerodynamic continuity.

Because the length of the slot is less than 1/2 wavelength, the antenna appears inductive at its feed point. This inductance is resonated at 400 Mc with a capacitance placed 1/4 of the distance from the edge of the slot. The ideal place for the capacitor would be at the center of the slot where the rf currents are minimum, but bell-jar tests simulating atmospheric pressures during flight showed that at sufficiently high pulse repetition rates, a corona discharge occurred in the vicinity of the resonating capacitor. This tendency was reduced somewhat when the capacitor was displaced away from the antenna center. Under these circumstances no detectable corona breakdown occurred at any pressure when the pulse repetition rate was reduced to the normal 2 pulses per second.

The antenna feed point was determined by experiment to match 50-ohm coaxial cable when the antenna is tuned to resonance at 400 Mc. This can be accomplished by supporting the sphere on a 5-in. polystyrene cylinder to minimize proximity effects and feeding the antenna with a 50-ohm coaxial cable entering the sphere at right angles to the plane of the antenna. A dummy sphere hemisphere with an entrance hole for the cable is a useful adjunct here. The coax cable is cut so that it is an integral number of half wavelengths long at 400 Mc. A Hewlett-Packard type 803A VHF bridge and detector serve to measure and adjust the impedance and phase angle at the antenna feed point. Since the transmitter was previously aligned while working into a 50-ohm resistive load, this method provides an accurate and direct means to optimize the tuning of the complete system. An independent check of antenna tuning (which also serves as a rapid method for initial adjustments) can be accomplished by using an M. C. Jones "Micromatch" standing wave ratio indicator. With a CW source of 400-Mc power, the micromatch is inserted in the coax line, and the antenna tuning

capacitor is adjusted for zero back power. Compared to the bridge method, the SWR indicator is a more rapid but less sensitive indicator of proper antenna tuning.

Radiation patterns for the sphere are shown in Figs. 8 and 9. The patterns were obtained by using an antenna test range consisting of two towers 36 ft above ground and separated by 170 ft. One of the towers is shown in Fig. 10. Two mechanically ganged helical antennas feeding separate receivers constitute the detector system for the sphere signal. The antennas, described more fully in a later section, have their helices wound in opposite directions, thereby allowing optimum response to the sphere radiation which has a circularly polarized component. Since the receiver outputs are added, consideration of the patterns will show that the sphere appears as a reasonably good approximation of an isotropic radiator. Thus, since no sharp nulls are present, the received signal strength is essentially independent of sphere orientation during flight.

2.7 POWER SUPPLIES AND CONTROL CIRCUITS

Power for the sphere circuitry is furnished by 6 Yardney HR-1 Silvercels connected in series for filaments, intervalometer motor, and accelerometer coils; B+ voltage is supplied by 4 Burgess Y-10 and 4 Burgess Y-15 hearing-aid type batteries connected in series to provide 150 volts. Since the Silvercels must supply the high peak current required by the accelerometer coils during the bobbin pick-up interval of approximately 150 millisec as well as the filament and motor load, only fully charged cells should be used for flight operations. When fully charged and in good condition, these batteries are capable of dependable operation for at least 25 min provided that the cell internal temperature is 70°F. This is more than ample time for all necessary preflight checks and the firing count-down procedure. At lower temperatures, the cell internal resistance increases and reduces the period of satisfactory operation. It is standard practice to keep track of all preflight operating time on flight batteries after their final installation so that they will not be over-extended during flight.

In contrast to the Silvercels, the B+ batteries do not require special care because the load they supply is very modest. The low duty cycle of the transmitter makes possible many hours of operation from one set of B+ batteries.

Both A and B batteries can be checked externally by using monitor jack M4S (see Fig. 4). The procedure consists of unscrewing the pressurized cap covering the jack and inserting a mating plug connected to suitable monitoring meters. The function switch S, is turned to the "heaters only" position and the A voltage is noted. After a 30-sec interval for filament warm-up has elapsed the function switch is rotated to "test" position. This position energizes all portions of the sphere circuitry. Since the intervalometer motor and accelerometer coils are now operating, the A battery load is much greater. If the average A voltage does not fall below 8.4 volts, the batteries can be considered satisfactory for flight use.

When the function switch is placed in the "flight" position, the intervalometer and accelerometer coils are deenergized if the "start switch" S_2 is in the open position. S_2 is a pressurized spring-loaded plunger switch placed on the sphere periphery as shown in Fig. 2, section BB. When placed inside the nose cone for flight, the sphere is oriented so that a 1/4-in.-diameter steel ball depresses the plunger and opens the switch. The ball is held in place by the nose cone immediately adjacent to the sphere surface. Upon sphere ejection the steel ball is no longer constrained; this allows the plunger to close the switch and start the intervalometer and accelerometer.

Although not always necessary, a gravity sensitive switch can be incorporated in the control circuitry as shown in Fig. 3. This "G" switch is designed to latch in the closed position when subjected to an acceleration of from 4 to 6 g. When used, its purpose is to turn on all filaments at rocket takeoff. This conserves battery life when the sphere is flown in rockets requiring a long count-down time. The G-switch was used successfully aboard an Aerobee rocket (SM 2.10) in the Fort Churchill firing series.

3. NOSE CONE

The nose-cone and sphere ejection mechanism for the flights of this report was the same as that of DAN 2 of the previous report with a few minor exceptions:

(a) Radar beacon DPN-19 was included in AM 6.01 fired at Wallops but omitted from the Rushmore and Churchill flights.
(b) A switch with a bat handle operated by a wire loop was used for starting the timer at take-off on the Nike-Cajuns.
(c) Yardney Silvercels were substituted for Willard lead-acid cells in the sphere and nose cone on the Nike-Cajuns.
(d) The 4130 alloy steel "guns" in which the ejecting blasting caps were encased in DAN 2 were omitted in the Nike-Cajuns.

The nose-cone assembly used on the Nike-Cajuns is shown in Fig. 11. Figure 12 shows the sphere resting in the support structure and Fig. 13, the assembled nose cone. The circuit diagram for the ejection system is seen in Fig. 14 and the details, in Figs. 15 and 16.

TELEMETERING GROUND STATION

The sphere telemetering ground station shown in Figs. 3 and 17 consists of manually tracked, ganged helical antennas, rf pre-amplifiers and AM receivers for detection of the received pulse signals. The dual signal channels to this

point circumvent the sphere antenna nulls by utilizing the fact that the sphere antenna has a circularly polarized radiation component. With oppositely wound antenna helices, the separately detected signals when combined in an adder appear spatially as emission from an isotropic radiator. Since the circular polarization is not perfect, slight deviations in pattern uniformity are observed. Extensive pattern tests show only one sphere null as great as 6 db; all other nulls are 3 db or less.

The signal output from the pulse adder output which at this point is called "mixed raw data" is fed simultaneously to the tape recorder and to a pulse shaping and amplifying chain. The pulse shaper was devised in an effort to improve the signal-to-noise performance, especially in the presence of manmade interference. At the pulse amplifier output, the signal designated "clipped output" is fed to the tape recorder and in a somewhat modified form to the Brush ink-writing recorder.

A final item in the system is the precision frequency standard used as a time base for both the tape recorder and the ink writer. Although not shown in the block diagram, the time bases are keyed on at the moment of missile take-off by a tail fin lift-off switch on the launcher rail.

4.1. ANTENNAS

The antennas with 10-turn oppositely wound helices are shown mounted together in Fig. 18. A spacing of 2 wavelengths separates the helix axes and separate ground planes are provided for each antenna. Typical azimuth and elevation radiation patterns for these antennas when mounted together are shown in Figs. 19 and 20. Complete elevation patterns could not be obtained because of antenna test range limitations. The patterns agree closely with typical patterns in the literature, however, and in no case are the antennas normally used outside the regions defined by the figures. The antennas have a beam width of approximately 36° and a gain of about 15 db over a dipole when receiving a plane polarized signal. Tests were also made with only one antenna in place to investigate the mutual interaction and only slight effects were noted, primarily in the azimuth side lobes.

The antenna terminal impedance is approximately 140 ohms which must be transformed down to 50 ohms for the transmission line. This is accomplished with an adjustable length 84-ohm coaxial stub mounted at the antenna feed point. Proper matching is readily accomplished by feeding the antenna from a 400-Mc CW source and adjusting the stub length for zero back power as indicated on a Jones micromatch or similar standing-wave instrument.

Antenna tracking is accomplished by orienting the antennas for maximum signal with the aid of a meter at the antenna site which indicates the average received signal strength. The operator also takes advantage of the predicted sphere trajectory as calculated prior to flight.

Experience with 6-turn helix antennas having a beam width of approximately 45°, as well as the 10-turn antennas, indicates that, unless more complicated means are used for tracking, the latter type represents a practical minimum for antenna beam width provided that the pulse repetition rate remains approximately 2 per second.

4.2. RF PRE-AMPLIFIERS

Since the AN/FMQ-2 receivers exhibit relatively high equivalent input noise, an rf pre-amplifier shown in Fig. 21 is placed in each antenna line. The pre-amplifier uses the General Electric GL6299 low-noise co-planar triode in a co-axial line grounded grid amplifier circuit. The amplifier has a 10-Mc bandwidth centered at 400 Mc with a gain of approximately 12 db. This results in an improvement of about 8db in the receiver signal-to-noise ratio. With the receiver rf gain control setting at "8," an input signal of 2 microvolts at the pre-amp input produced a usable output signal.

4.3. RECEIVERS

The R 228-AN/FMQ-2 receiver used in the ground station was originally designed for reception of frequency modulated radiosonde signals between 390 and 420 Mc.[5] It was thus necessary to modify the IF amplifier and detector for AM operation. This was accomplished as shown in Fig. 22. The Foster-Seely FM discriminator stage was converted for AM demodulation by open-circuiting the discriminator transformer secondary L129B and using its primary as a single tuned parallel resonant circuit. An IN34A germanium diode is used as the detector, producing negative-going video pulses. The receiver IF bandwidth is adjusted by proper selection of resistor R137. A total bandwidth of 600 kc provides good pulse fidelity and ease of tuning of received signals.

In addition, cathode bias was added to the fifth IF stage to improve its large signal handling capacity and the FM limiter stage just preceding the detector was modified by introduction of cathode bias and increase of plate voltage to achieve normal IF amplifier performance. The modification was completed by installing a cathode follower stage after the crystal detector to eliminate pulse shape distortion by output cable shunt capacity.

4.4. PULSE CHASSIS

In addition to the functions indicated on Fig. 3, the "pulse chassis" shown in Fig. 22 includes circuits to: (a) key on the time signals from the frequency standard at missile take-off, (b) generate a signal whose average value is proportional to the peak amplitude of the received pulses for antenna tracking purposes, (c) modify the received pulse shape for Brush recorder use, and (d) provide for oscilloscope monitoring at key points in the various circuits.

The receiver cathode follower outputs are summed at the grid of V_{9A} through 100-K isolating resistors. V_{9A} acts as a direct coupled cathode follower for driving the crystal diode clipping and limiting network. The operation of this network is as follows: CR_1 attenuates all signal components which are more positive than the voltage set by R_1. Thus any signal having no components going further negative than the preset voltage is attenuated. By appropriate setting of the voltage, noise can be rejected. CR_2 is biased approximately 1 volt more negative than CR_1; this will attenuate all signals which exceed this level in the negative direction, thus providing a limiting action. The idealized output of this network consists of clean rectangular pulses. Three voltmeters on the pulse chassis front panel indicate the bias on each of the crystals and the difference in these biases, respectively.

The clipped and limited signal is coupled to cathode follower V_{9B} to prevent loading and provide a low output impedance level for driving V_3, a pentode amplifier with a gain of approximately 12. The amplified signal which is now a positive going pulse is fed next to cathode follower V_{4B} for signal isolation purposes. Similar functions are performed by cathode followers V_{4A} and V_{5A} for mixed raw data and 10-kc timing signals, respectively.

From V_{4B} the pulses are fed to V_{5B}, a driver amplifier for the Eccles-Jordan bi-stable flip-flop stage using the two triode sections of V_8. The action of this circuit is to flip from one stable state to the other each time a pulse is received. Its output, therefore, is a rectangular wave, changing from one level to the other at each start and stop pulse. This output is directly coupled to cathode follower V_6 which in turn drives the Brush pen motor directly. Triggering sensitivity of the flip-flop section is controlled by adjusting the "amplify level" control in the grid circuit of V_3. The other channel of the Brush recorder is driven by cathode follower V_7. This stage supplies the 10-cps time base for the Brush record.

Because of the short duration of the received pulses and the relatively long time interval between them, a peak-reading voltmeter is used for the signal strength meter. Negative-going mixed raw-data pulses are applied to isolating cathode follower V_{11}. The pulses charge the 1000-μμf coupling capacitor through one half of V_2 which is connected as a charging diode, with a charging time constant of approximately 1 μsec. The capacitor potential which closely approaches the peak value of a 10-μsec pulse is applied to the grid of the other half of V_2 which functions as a cathode follower meter driver. The 2500-megohm grid resistor and the slight cathode follower grid current caused by residual gas in the tube produces a discharge time constant of the order of 1 to 2 sec. Since approximately 2 pulses per second are normally received, the coupling capacitor is maintained at a charge determined by the average amplitude of the received signals.

The remaining tube on the pulse chassis is yet another cathode follower, V_{10}. It serves as a signal isolator for oscilloscope monitoring of all important pulse chassis waveforms.

Also included on the pulse chassis are 4 Sigma relays, all connected in series between the +220 B+ line, and a plug which is used to connect the relays back to chassis ground through the launcher take-off switch. The relay contacts are in series with the 100-kc, 10-kc, and 10-cps time signals supplied to the magnetic tape and Brush recorders. A manually operated "start-pulse signal-on reset switch" is also in series with these contacts so that, in case of switch malfunction at the launcher, the timing signals can be applied to the record at a known time after take-off. It will be noted that the relays deenergize at take-off, which provides some degree of fail-safe protection. The relay operating current is less than 7 milliamp which is below the level required for rocket igniter operation.

4.5. TIMING SIGNALS

A Hewlett-Packard type 100D secondary frequency standard accurate to 2 parts in one million, and calibrated against a WWV time signal, is used for timing purposes throughout the ground station. All timing signals are keyed on at take-off and thus provide a means to determine elapsed flight time to a high degree of precision. This method also eliminates timing errors caused by variations in tape drive speed, whether during recording or playback.

4.6. DATA RECORDERS

Pulse and timing signals are recorded simultaneously on a 7-channel Ampex magnetic tape recorder and on 2 dual-channel Brush pen recorders. Wherever possible, backup against circuit failure is insured by duplicate channel recording. The tape recorder input signals consist of 2 channels of mixed raw data and 1 each of clipped and limited pulses, 10-kc and 100-kc timing signals. The two Brush recorder units with pen motors in series record the flip-flop output and the 10-cps timing signal.

Primarily because of recording problems, only 5 of the 7 channels in the tape recorder are used. To record the 10-μsec pulses with reasonable fidelity, the tape speed is 60 in./sec. At this speed the channels nearest each edge of the 1-in. tape exhibit considerable variation in output level and thus are not normally used. The use of highest quality instrumentation tape alleviates the problem somewhat, but does not eliminate it. Since 5 channels are adequate, the additional safety factor of 2 more backup channels was not considered necessary.

One further problem associated with the tape recorder is worth mention. When operated at 60 in./sec, the sine wave response of the recorder is 3 db down at approximately 85 kc and is falling at the rate of 12 db per octave. This is less than 1/3 the bandwidth necessary for reasonable reproduction of a 10-μsec pulse and as a result the recorder output pulse does not even approximate the input pulse shape. This situation was recognized early in the design of the system and was accepted as tolerable because the pulse shape distortion

caused an error in pulse time interval measurement of less than 0.1%, which is negligible. Pulse shape distortion is of importance in data reduction, however, when considerable manmade noise is present on the record. Under these circumstances it is impossible to recognize a received pulse from a random noise pulse even though the noise pulse width might be as little as 5 or as large as 15 μsec. Thus, if pulse width discrimination is to be utilized for improving system performance in the presence of noise, it must occur prior to tape recording.

5. FLIGHT-DATA PLAYBACK SYSTEM

The flight data recorded on magnetic tape are played back with the aid of the system shown in Fig. 24. For normal flight records, the 100-kc precision frequency channel and the mixed raw-data channel are used at a playback speed of 3.75 in./sec. Compared to the recording speed, this is a reduction of 16 to 1, introduced to facilitate data handling. Since an accelerometer transit interval occurs at the rate of about 1 per second during flight, the slow playback lengthens this interval to 16 sec. This is slow enough for an operator to read the start-stop pulse intervals directly off the counter decades without stopping the tape playback provided that there are only a few spurious noise pulses on the tape.

The 100-kc signal is counted by both the time interval counter and the total cycle counter. The interval counter is gated on and off by the start and stop pulses while the cycle counter indicates the total accumulated count from rocket take-off. Thus by reading interval count and total cycle count at the moment of each stop pulse, accelerometer transit time intervals and times from take-off are obtained directly. By counting cycles of the 100-kc precision time base, cumulative timing errors cannot occur and system accuracy is independent of both tape recording and playback speeds.

When low signal strength and manmade impulse types of noise combine to produce a noisy tape recording, the 2-channel Brush recording is very helpful in identifying true transmitted pulses. Figure 25 is a section of a typical flight record. The timing signal is a 10-cps sine wave which is switched on at take-off and provides the total cycle count (i.e., time) from take-off. The data channel records the output of the bi-stable circuit described in an earlier section. Each received pulse above a preset minimum amplitude triggers the flip-flop and thus causes the recording pen to deflect to the opposite of its two possible positions. Advantage is taken of the repetitive nature of normally transmitted pulses to determine manually accelerometer start and stop pulses on the record. Time interval measurements can also be scaled off manually with reasonable accuracy. With this information as a guide, it is usually possible to desensitize manually the gating circuit on the standard HP 522B interval counter until just before the expected appearance of a transmitted pulse.

Sensitivity is then restored in time for the time start pulse to gate the interval counter "on." A similar procedure can be followed for gating the same counter off when the stop pulse is expected.

In the presence of considerable noise it is sometimes necessary to replay a difficult section of the tape several times before the true pulse interval can be determined. The only precaution which must be observed is that the total cycle counter must be temporarily disabled during the repetitive playback procedure. Experience with the four Churchill flight records indicates that experienced operators can achieve better than 98% data recovery, even in presence of moderate noise on the record when using the techniques described above.

The bandpass filter at the tape recorder output is used to improve the signal-to-noise ratio of the 100-kc signal. At the slow playback speed the 100-kc signal is shifted down to 6.25 kc at playback and thus the bandpass filter must be adjusted so the center of the pass band is at the frequency.

The filter output is fed to a second counter which completes the data playback system. This counter is set to count and indicate the total number of cycles generated by the 100-kc time standard starting from rocket take-off. Since this is a cumulative count, eight decades in cascade must be used to handle the total number of cycles counted during normal sphere flights. In the system diagrammed here, availability of two counters, each with less than eight decades required the use of a phase inverting amplifier for proper cascading of the two units.

6. FLIGHT-SIGNAL-STRENGTH DATA

Reference was made in the section on the sphere antenna to the problem of ionization of the air near the antenna during bell-jar tests to simulate high-altitude conditions. Several tests showed that when transmitting at the normal rate of two pulses per second, rf breakdown does not occur at any pressure in a bell jar. If the repetition rate is raised to 50 pulses per second, however, air breakdown is observed at a simulated altitude of about 200,000 ft. This is also the altitude at which breakdown is predicted from theoretical considerations.[6] Neither the bell-jar tests nor the predicted results consider other effects known to be present during actual flight. These include the supersonic velocity of the sphere and other sources of energy including ultraviolet radiation, cosmic rays, soft X-rays, etc., none of which can readily be simulated in the laboratory.

Both theory and experiment indicate that, when breakdown occurs, only part of the radiated signal is consumed in the ionization process. Thus if the ground station receiver signal-to-noise ratio is adequate, reception should be possible at least to some extent even in the presence of breakdown. This has been borne out during actual firings. Figures 26, 28, 30, and 32 are signal-

strength records of the Churchill firing series as derived from the mixed raw-data channel of the tape recorder. When antenna breakdown is not present, the received signals are so large that the inverse square law effect is not observed even at maximum range because of pulse amplitude saturation in the tape recorder. Measurements of the complete ground station input-output characteristics indicate that a decrease of 17 db in rf signal strength at the receiver pre-amplifier input is necessary for a decrease of approximately 15 volts in mixed raw-data output during tape playback.

The curves of signal strength are plots of peak pulse amplitudes for both start and stop pulses as measured on an oscilloscope with no corrections for antenna nulls or inverse square distance effects. All records show breakdown effect both on the up- and down-legs except for the up-leg SM 2.10 trajectory. In this case, the sphere was deliberately ejected late and thus did not start transmitting until after the breakdown altitudes had been exceeded.

Figures 27, 29, 31, and 33 are companion curves of velocity, Mach number, density, and drag acceleration for comparison with the observed breakdown effects.

Since a review of the literature on antenna breakdown at high altitudes indicated that free electrons are involved in the process, an attempt was made to simulate the effect in the laboratory. As reported above, breakdown is not observed at the normal transmission rate of 2 pulses per second. If a small radioactive alpha source is placed adjacent to the antenna, however, breakdown is observed at 2 pps. A number of experiments were performed with and without the alpha source to investigate the effects of repetition rate, source proximity, transmitted power level, and density on observed breakdown. A reasonable degree of correlation between these tests and flight data was obtained. This work was carried out by the Gas Dynamics Laboratory of the Boeing Aircraft Company with a sphere loaned to them by the Michigan project. Major details of the work are reported in a paper scheduled for presentation at the June, 1959, RAND Symposium[7] on Aerodynamics of the Upper Atmosphere, Santa Monica, California.

7. DATA REDUCTION AND RESULTS

Considerable effort was expended in developing the methods of reducing data. In the flights with which this report is concerned, preliminary results were obtained by hand calculation. Refinements in the method for peak time and the necessity for using radiosonde data to establish altitude in the absence of rocket tracking were major changes of the method described in Ref. 1. For a synoptic method to be of maximum use operationally, the results must become available in days or even hours. To this end, the data-reduction method was almost completely programmed for the LGP-30 digital computer and all the final results of this report were calculated on the computer. The new speed of data

reduction has proved to be of great research value in understanding the data-reduction process by permitting analysis of variations and perturbations which would otherwise have been avoided because of tedious calculations.

7.1. DATA ANALYSIS PROCEDURES

The basic data consist of bobbin release times, when the bobbin is at the center of the accelerometer cavity, and bobbin contact times, when the bobbin touches the cavity walls. The difference between release time and contact time is the transit time which is in the range $.01 < \tau < 1$ sec approximately. The maximum accelerations experienced by the sphere are about 10 times gravity corresponding to a minimum transit time of about 10 millisec since the accelerometer gap is .188 in. The maximum transit time of nearly 1 sec is determined by the recycling period of the accelerometer caging mechanism. The minimum acceleration measured by the accelerometer is therefore a little greater than .001 times gravity.

The drag acceleration is computed from the formula

$$a_D = 2s/\tau^2 \quad , \tag{2}$$

where s is the accelerometer gap. This acceleration is an average value over the whole time the bobbin is in transit and is assumed to be applicable at the midpoint of the transit time interval.

The first step of the trajectory analysis is to find the time at which the sphere was at the peak of its trajectory. This peak time is found by comparing the drag accelerations on the up-leg and down-leg portions of the trajectory. The drag function is assumed to be symmetrical with respect to the peak time. Figures 34 to 41 show the values of the acceleration used to calculate peak time for each of the spheres. The numbered points were used to fit the straight lines by a least-squares analysis.

Initial values of peak altitude and horizontal velocity are assumed in order to compute a trial trajectory (see Appendix I). An inverse square law central gravitational force is used in these calculations. The effect of drag acceleration is included by making use of the accelerometer data. At low altitudes the density derived from sphere accelerations is compared with the density derived from radiosonde measurements of pressure and temperature. The difference in altitude between the two density functions is used to correct the initial value assumed for the peak altitude. The corrections are repeated until good agreement with the radiosonde data is achieved. A single adjustment is usually sufficient. Figures 42 to 49 show how the two density functions agree for each of the spheres after all corrections to the trajectory have been made. There are two exceptional cases. Radar tracking data were taken in the case of AM 6.01 from which one can derive initial values for the trajectory analysis. In the case of SM 2.10, DOVAP tracking data are the source of the initial values.

The air density is related to the drag acceleration by the equations

$$D = C_D A \, 1/2 \, \rho V^2 \tag{3}$$

and

$$D = ma_D \quad . \tag{4}$$

These equations can be solved for air density with the result

$$\rho = \frac{2m}{C_D A} \frac{a_D}{V^2} \quad . \tag{5}$$

The sphere cross-section area A, and the mass of the sphere not including bobbin m, are constants. The drag acceleration a_D was discussed above. The velocity of the sphere relative to the atmosphere V is known from the trajectory analysis. The drag coefficient C_D is a function of Mach number M and Reynolds number Re; it is plotted in Fig. 50. One finds that the paths of all the spheres in the C_D plane (Fig. 50) are approximately the same because of the similarity of the trajectories. The paths are such that the two-parameter function for C_D can be replaced by the two single-parameter functions, plotted in Fig. 51. These functions are particularly useful for the automatic processing of the sphere data since it is much simpler to store a single-parameter function than a two-parameter function.

It is necessary to determine the Mach number and Reynolds number in order to find the drag coefficient. The Mach number is defined by

$$M = V/a \quad . \tag{6}$$

The velocity V is known from the trajectory analysis. The speed of sound a is a rather slowly varying function of the altitude which can be found with reasonable accuracy by consulting The ARDC Model Atmosphere, 1956.[8] The Reynolds number is defined by

$$Re = \rho V d/\mu \tag{7}$$

where d is the sphere diameter. The viscosity μ, like a, is a slowly varying function of the altitude and is taken from the model atmosphere. It is believed that the difference between the model atmosphere density and the actual density is greater than in the case of μ and a. It is not necessary to rely upon the model in this case because the density can be replaced by accelerometer data according to Eq. (5). The result is

$$Re = \frac{2md}{A} \frac{a_D}{C_D \mu V} \quad . \tag{8}$$

The initial approximation to the Reynolds number can now be found by assuming $C_D = 1$ in Eq. (8). The second approximation to C_D is found by entering Fig. 51 with this Reynolds number and Mach number. The drag coefficient substituted in Eq. (8) results in a second approximation to the Reynolds number. These iterations converge very rapidly. Three iterations are used in the sphere data analysis.

The atmospheric pressure is related to the density by the formula

$$\Delta P = - \bar{\rho}\, \bar{g}\, \Delta y \quad . \tag{9}$$

The mean density is calculated from the density at the upper and lower ends by the formula

$$\bar{\rho} = \frac{\rho_1 - \rho_2}{\ell n(\rho_1/\rho_2)} \quad . \tag{10}$$

Formula (10) is preferable to the arithmetic mean because it is exact in the case of an exponential density distribution. When integrated, Eq. (9) relates the pressure at an arbitrary level to the pressure at an initial level.

$$P = P_i - \Sigma\, \bar{\rho}\, \bar{g}\, \Delta y \tag{11}$$

If the initial level is taken at the highest altitude, the first term of Eq. (11) becomes small compared with the summed terms as the sphere falls to lower altitudes. Therefore it is not essential that the initial estimate of the pressure is exactly correct. The initial pressure P_i is estimated by assuming an initial temperature of -105.34°F (model atmosphere), deriving the density from Eq. (5), and then substituting in the equation of state

$$P = 1716.25\, \rho T \quad . \tag{12}$$

At lower levels the temperature is found by deriving pressure and density from Eqs. (11) and (5), and then substituting in Eq. (12).

The calculated temperatures at the highest altitudes cannot be relied upon because of the influence of the arbitrary choice of temperature at the initial point of the calculations, and also because of the relatively severe scatter in the accelerometer data at the highest altitudes. If a different choice of the initial point for the temperature calculations were made, it would have a rather strong effect on the calculated temperatures immediately below. For these reasons the calculated temperatures in the highest 15-km level, having doubtful geophysical significance, were not exhibited in the temperature plots.

The trajectory calculations and density derivations were computed with an LGP 30 digital computer. The data processing is not completely automatic at this time. The accelerometer data are manually read from the magnetic tape recordings and reduced to accelerations as a function of time and then punched onto the paper tape required by the computer. The peak time derivation is also

a manual operation, as is the comparison with radiosonde data after the first trial trajectory is computed.

7.2. RESULTS

Table II summarizes all the small-sphere firings carried out by The University of Michigan to date. Figures 52 to 59 are the calculated densities plotted as a function of altitude for the 8 successful pre-IGY and IGY flights. Figures 60 to 67 are the corresponding temperatures vs. altitude. Also, tabulated results in both English and metric units are reproduced. Results from DAN 2 may be found in Ref. 1.

7.3. SOURCES OF ERROR

According to Eq. (5) the fundamental quantity measured is the product of air density and the drag coefficient.

$$C_D\rho = \frac{2m}{A}\frac{a_D}{V^2} \tag{13}$$

An error in the drag-coefficient data will therefore cause an error in the derived atmospheric density. If new drag-coefficient data should become available, Eq. (13) can be used to make the appropriate changes in the derived atmospheric density. If the drag coefficients applicable at the radiosonde altitudes are changed, it will also be necessary to change the derived altitudes. It is believed that the drag-coefficient data are most reliable in this range, however, since much experimental work has been done here. The uncertainty in the drag coefficient is estimated to be 2% if the drag coefficient is near unity. At very low Reynolds numbers, the drag coefficient approaches two where the error may be 5 or 10%.

It is believed that the overall accelerometer errors are of the order of magnitude of 1% of the acceleration actually being measured. The effect of accelerometer errors on the air density calculation is therefore not very serious. Of more concern are the errors introduced into the determination of the altitude. These errors depend very strongly on the maximum altitude of the radiosonde data. If the comparison with radiosonde data can be made at an altitude of 100,000 ft the effect of air drag on the trajectory is very small. The maximum drag accelerations occur at about 80,000 ft. If the comparison with radiosonde data is made at 50,000 ft the accelerometer data must be relied upon to extend the trajectory calculations down to this altitude. The errors are greater in this case because the accelerations to be measured are greater and also because the time over which the velocity errors integrate is greater. Figures 42 to 49 show the comparison with radiosonde data. The analysis of this error is discussed further in Appendix II. It is estimated

that the error in altitude may be approximately 1500 ft in the case of AM 6.09, 6.10, and 6.12. The radiosonde data extended to the relatively low altitude of 50,000 ft in these cases. The radiosonde data went higher than 100,000 ft for AM 6.02, 6.03, and 6.05 and the error is estimated to be about 60 ft. These errors always appear at the higher altitudes because the data analysis procedures require agreement at the radiosonde altitude.

Trajectory errors can also result from an error in the derivation of the densities which are compared with radiosonde densities. According to the drag equation (5), the error in density is related to errors in acceleration, drag coefficient, and velocity by the formula

$$\frac{\Delta\rho}{\rho} = \frac{\Delta a_D}{a_D} - \frac{\Delta C_D}{C_D} - 2\frac{\Delta V}{V} \quad . \tag{14}$$

On the other hand, it can be shown that an error in altitude is related to an error in density by the formula

$$\Delta y = - H \frac{\Delta\rho}{\rho} \quad , \tag{15}$$

where H is the scale height, about 20,000 ft. Therefore

$$\frac{\Delta y}{H} = - \frac{\Delta a_D}{a_D} + \frac{\Delta C_D}{C_D} + 2\frac{\Delta V}{V} \quad . \tag{16}$$

A 1% error in acceleration causes a 200-ft error in altitude. A 2% error in drag coefficient causes a 400-ft error in altitude.

According to Appendix II, the velocity error becomes insignificant if the radiosonde data extend up to 100,000 ft. An error of 1/4% causes an error of 100 ft in altitude. In the case of AM 6.09, 6.10, and 6.12, however, a velocity error of 10-15% is possible or 5000 ft in altitude. This is the most serious of all the trajectory errors.

An error in estimating the time when the sphere is at the peak of its trajectory can also result in trajectory errors. The following formulas are applicable:

$$\Delta V = \bar{g}\, \Delta t_P \tag{17}$$

$$\Delta y = \bar{g}\, \Delta t_P (t_L - t) \tag{18}$$

where $\bar{g}$ is an average value of the acceleration of gravity, Δt_P is the error in peak time and t_L is the time at which the sphere densities are compared with radiosonde densities. In a typical case $\bar{g}$ = 31, Δt_P = .1, and $t_L - t$ = 50. According to Eqs. (17) and (18), ΔV = 3.1, and Δy = 155. This is a relatively

minor source of error except in the case of AM 6.09 where the up-leg accelerometer data are more scattered. The error in peak time is estimated to be about 1/2 sec for 6.09.

A possible source of error is the initial horizontal component of velocity assumed in the trajectory calculations. If the launching angle is 85°, the horizontal velocity should be about 500 ft/sec. This value is used in all trajectory calculations which lack tracking data. A trajectory computed with zero initial horizontal velocity shows only a slight departure from the standard trajectory.

AM 6.01 and SM 2.10 are exceptional cases. Due to lack of accelerometer data at radiosonde altitudes (AM 6.01), it is necessary to rely on the up-leg radar data for initial values of altitude and velocity for trajectory analysis. The quality of the radar data indicates that an error of 1000 ft might be expected on the down-leg part of the trajectory and negligible error on the up-leg trajectory. Since both radar tracking data and up-leg drag data are available for AM 6.01, the peak time can be calculated in two ways and the results compared. According to Fig. 34, it is 171.70. According to Table III, it is 171.83. Although the agreement is good, it may be fortuitous since the accelerometer data are quite scattered.

DOVAP tracking data are available in the case of SM 2.10 but there are no up-leg accelerometer data. Initial velocity and altitude at the time of sphere ejection can be found from the DOVAP records. A possible source of trajectory error is the initial velocity of the sphere relative to the rocket. The sphere ejection was normal to the rocket axis at a velocity of about 30 fps. The greatest error results if one assumes the rocket is oriented so that the initial velocity is in a vertical direction. The down-leg accelerometer data appear about 250 sec after ejection. Hence the maximum error in altitude is estimated to be 30 x 250 = 7500 ft.

7.4. DATA QUALITY

The falling-sphere system for air-density measurement at its present state of development performs best in a middle range of altitudes, from 100,000 ft (30 km) to about 250,000 ft (80 km). In this range the raw accelerometer data plots smoothly with very few missing points. The drag coefficients assumed vary between .9 and 1.1. It is believed that the data can be relied upon to calculate atmospheric density and temperature functions which have geophysical significance. Certain difficulties are encountered at each end of the range of altitudes which in some cases affect the altitude calculations throughout. The more recent work, AM 6.02, 6.03, and 6.05 has demonstrated that these difficulties have been largely overcome.

At the high altitudes the drag acceleration becomes very small and ultimately the threshold of accelerometer sensitivity is passed. This effect can

be seen in Figs. 34 to 41 where accelerometer output is plotted as a function of time. The scatter in the acceleration data also causes scatter in the density vs. altitude plots in Figs. 52 to 59 and the temperature vs. altitude plots, Figs. 60 to 67.

The most important factor causing the low drag scatter is believed to be the spinning motion of the sphere. The effect can be reduced if the center of gravity of the sphere is placed at the geometrical center of the sphere. In the case of the most recent spheres fired, AM 6.02, AM 6.03, AM 6.04, and SM 2.10, the center of gravity was more carefully controlled and the data apparently improved as a result. The recycle time of approximately 1 sec imposes a low acceleration cutoff on the accelerometer. The effect is masked by the scatter found at low accelerations except in those cases of relatively low scatter. The cutoff occurs at approximately 300,000 ft (90 km).

It is not possible to make an accurate determination of peak time if there are only a few scattered acceleration data points to analyze as in the case of AM 6.09.

Two difficulties are present at low altitudes. The maximum accelerations occur at approximately 80,000 ft (25 km) and approach 10 g's in magnitude (Tables IV to X). The operation of the accelerometer under these conditions is marginal due to lack of power for centering the bobbin. An improved version of the accelerometer with a lighter bobbin, used in AM 6.02, AM 6.03, AM 6.05, and SM 2.10, shows some improvement. When several acceleration data points are missing, smoothed values are estimated in order to improve the trajectory calculations.

If the accelerometer bobbin is not driven all the way to the center, the output will indicate accelerations which are too high. In most cases one finds a few indicated accelerations which are much too high. These are suppressed in the data analysis. In the case of SM 2.10 the peak accelerations are not obviously wrong. However, closer inspection reveals that they are a bit high when one considers that the peak altitude of the sphere trajectory is relatively low. The density and temperature plots, Figs. 57 and 65, also seem to be abnormal in this area.

It is believed that the drag-coefficient data may be in error at a Mach number of 1.3 or less. In this range the drag-coefficient curve falls away rather sharply from a value of one, which suggests that the character of the flow about the sphere may be changing. The Reynolds number is about a half million which is in the right range for boundary-layer transition phenomena.[9] In this case the drag is very sensitive to minor changes in surface finish on the sphere and turbulence in the air. Consequently one cannot expect good agreement with drag-coefficient charts derived from wind tunnel or other tests. When the drag coefficient becomes less than one at low Mach numbers, it is not considered to be reliable for the analysis of falling-sphere data. This sets a lower limit of about 60,000 ft (18 km) to the densities derived by the falling-sphere method.

Another phenomenon of interest is the tendency for the acceleration data to become more scattered below approximately 60,000 ft. It is believed that an unsteady condition of flow exists accompanied by lateral accelerations. Other aerodynamic experiments with spheres have revealed such a phenomenon.[10,11] Since the accelerometer is an omni-directional device which cannot distinguish lateral from vertical accelerations, it is not possible to extend the trajectory analysis to the time of impact with the ground.

8. RECOMMENDATIONS

The sphere experiment has produced significant geophysical results. Its potential contribution to research and operations may be fully realized by further automation. It is recommended that those parts of the data-reduction process which are still performed manually be programmed for computer. Automatic transcription of the telemeter magnetic tapes to computer tapes is feasible and the process should be developed. Many improvements in the flight and ground instrumentation are possible to increase signal-to-noise ratio and the altitude at which useful data can be obtained. It is recommended that all the above developments be carried out and tested in actual flight and data-reduction operations.

9. ACKNOWLEDGMENTS

Development and use of the sphere experiment has continued since 1954 under the sponsorship of the Air Force Cambridge Research Center. We wish to acknowledge the financial support and splendid cooperation of AFCRC. During the IGY additional support was made from IGY funds for which we wish to thank the Technical Panel for Rocketry of the U. S. National Committee for the IGY and also the National Science Foundation. The first small-sphere firings were carried out at Wallops Island, Va., with the generous assistance of the NACA Pilotless Aircraft Research Division people at Wallops and at Langley Field. The shipboard operations took place on the USS Rushmore (LSD-14). The willing cooperation of Cdr B. J. Gemershansen and his crew were essential to the success of the ship firings. During the IGY, the firings were conducted at Ft. Churchill, and we wish to express our appreciation to all at Churchill who contributed to our program.

One sphere was carried on Aerobee SM 2.10, a grenade rocket prepared and fired at Churchill jointly by The University of Michigan and the U. S. Army Signal Research and Development Laboratories. We wish to thank the grenade group for the ride.

APPENDIX I

TRAJECTORY ANALYSIS EQUATIONS

The inverse square law of gravitation is assumed. In this case it is convenient to use the parameters r and ϕ where r is the radius to the earth's center and ϕ is the polar coordinate angle. The polar coordinate velocities are defined by

$$u_r = \dot{r}$$
$$u_\phi = r\dot{\phi} \quad . \tag{19}$$

The equations of motion for the vacuum portion of the trajectory are

$$\dot{u}_r = -g_o \frac{r_o^2}{r^2} + \frac{u_\phi^2}{r}$$
$$\dot{u}_\phi = -\frac{u_r u_\phi}{r} \quad . \tag{20}$$

The sea level value of gravity, g_o, can be found from Helmert's equation[12] provided a term is added to take into account the acceleration due to the earth's rotation. Helmert's equation gives the sea level gravity as measured by a gravimeter fixed on the earth's surface. In the present analysis the applicable quantity is the gravity that would be measured on the surface of a non-rotating earth. The equation used is

$$g_o = 32.172 - .0851 \cos 2\phi_L + .00023 \cos^2 2\phi_L + .11115 \cos^3 \phi_L \quad . \tag{21}$$

In this equation ϕ_L is the latitude angle. At lower altitudes a drag term must be added to Eqs. (20). The horizontal component of the sphere relative to the atmosphere is u_{ϕ_D}. The eastward component of velocity due to the earth's rotation is u_{ϕ_E}. Reference is made to the sketch below which shows how the velocity components are related in the horizontal plane. It is assumed in these

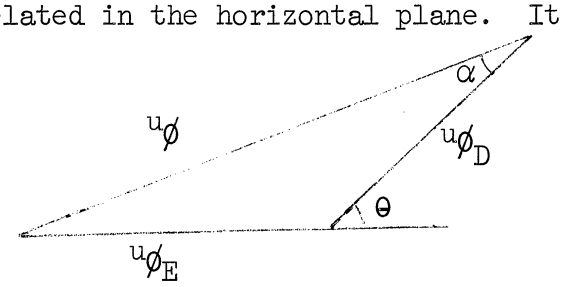

calculations that the drag reduces the velocity $u\phi_D$ while θ remains constant. The equations of motion then become

$$\left.\begin{aligned} \dot{u}_r &= -g_o \frac{r_o^2}{r^2} + \frac{u\phi^2}{r} - a_D \frac{u_r}{V} \\ \dot{u}_\phi &= -\frac{u_r\, u\phi}{r} - a_D \frac{u\phi_D}{V} \cos\alpha \end{aligned}\right\} \tag{22}$$

where

$$u\phi_D = \pm\sqrt{u\phi^2 - u\phi_E^2 \sin^2\theta} - u\phi_E \cos\theta$$

$$u\phi_E = r\,\Omega \cos\phi_L$$

$$V^2 = u_r^2 + u\phi_D^2$$

$$\cos\alpha = \frac{1}{u\phi}\left(u\phi_D + u\phi_E \cos\theta\right) .$$

Equations (22) must be integrated numerically since the drag-acceleration data points are approximately 1 sec apart. The numerical integration can be improved if mean values of certain variables are used, applicable to the middle of the interval. The difference equations numerically integrated to derive sphere trajectories are

$$\left.\begin{aligned} \frac{\Delta u_r}{\Delta t} &= -g_o \frac{r_o^2}{\bar{r}^2} + \frac{u\phi^2}{\bar{r}} - \bar{a}_D \overline{\left(\frac{u_r}{V}\right)} \\ \frac{\Delta u_\phi}{\Delta t} &= -\frac{u_r\, u\phi}{\bar{r}} - \bar{a}_D \overline{\left(\frac{u\phi_D}{V}\right)} \cos\alpha \\ \frac{\Delta r}{\Delta t} &= \bar{u}_r \end{aligned}\right\} \tag{23}$$

where

$$\bar{a}_D = a_D + \frac{1}{2}\Delta a_D$$

$$\overline{\left(\frac{u_r}{V}\right)} = \frac{u_r}{V} - \frac{\bar{g}\,\Delta t}{2V}\left(\frac{u\phi_D}{V}\right)^2$$

$$\overline{\left(\frac{u\phi_D}{V}\right)} = \frac{u\phi_D}{V} + \frac{\bar{g}\,\Delta t}{2V}\left(\frac{u_r}{V}\right)\left(\frac{u\phi_D}{V}\right)$$

In all cases the earth's radius, r_o, is assumed to be 20,903,520 ft (3959 miles). The following constants were used in the trajectory analyses of the different spheres.

	$\cos \phi_{LAT}$	g_o	$\cos \theta$
AM 6.01	.79016	32.206	.91355
AM 6.02	.51877	32.227	.79864
AM 6.03	.51877	32.227	.79864
AM 6.05	.51877	32.227	.89337
AM 6.09	.65672	32.215	.96593
AM 6.10	.53337	32.226	-.70711
AM 6.12	.41337	32.236	.34202
SM 2.10	.51877	32.227	-.15518

APPENDIX II

EFFECT OF ACCELEROMETER ERROR ON THE TRAJECTORY ANALYSIS

Errors due to the accelerometer can be estimated by comparing the velocity and altitude according to Appendix I with vacuum trajectory calculations of velocity and altitude computed from the same equations except that the a_D term is set equal to zero. The accelerometer error is assumed to be 1% of the acceleration being measured. The velocity error is therefore 1% of the difference between the actual velocity and the vacuum trajectory velocity and the altitude error is 1% of the difference between the actual altitude and the vacuum trajectory altitude. There is a very slight difference in the acceleration of gravity between the actual trajectory and the vacuum trajectory at the same time (due to the difference in altitude) but this is not an important consideration in an error analysis which is necessarily quite crude. Figure 68 shows qualitatively how the actual velocity and altitude compare with the vacuum velocity and altitude in a typical case. These plots show the desirability of comparing with radiosonde data at a high altitude at time t_H rather than at a low altitude at time t_L. If trajectory calculations are extended to sea level in order to verify the assumed peak altitude, the difference between the two trajectories becomes about 900,000 ft. Hence a 1% accelerometer error results in a 9000-ft altitude error.

Table XI summarizes the results of this error study. An accelerometer error of 1% is assumed except for AM 6.10 and AM 6.12 where it is 2% to account for the relatively large number of missing data points at the high accelerations.

REFERENCES

1. Jones, L. M., and Bartman, F. L., A Simplified Falling Sphere Method for Upper-Air Density, Univ. of Mich. Eng. Res. Inst. Report No. 2215-10-T, Ann Arbor, June, 1956.

2. Hansen, W. H., and Fischbach, F. F., The Nike-Cajun Sounding Rocket, Univ. of Mich. Eng. Res. Inst. Report No. 2453-1-F, Ann Arbor, March, 1957.

3. Jones, L. M., Fischbach, F. F., and Peterson, J. W., Seasonal and Latitude Variations in Upper-Air Density, IGY Rocket Report Series No. 1, National Academy of Sciences, July, 1958 (47-57).

4. Jones, L. M., "Transit Time Accelerometer," Rev. Scien. Instr., 27, 374-377 (June, 1956).

5. Radiosonde Receptor AN/FMQ-2, Department of the Army Technical Manual TM11-2434, Department of the Air Force Technical Order T016-30FMQ2-6, July, 1951.

6. MacDonald, A. D., "High Frequency Breakdown in Air at High Altitudes," Proc. I.R.E., 47, No. 3 (March, 1959).

7. Burns, G. A., Linder, W. J., Schorsch, J. F., Steele, H. L., and Schulte, H. F., "Formation of a Radiofrequency Plasma at an Antenna During Falling-Sphere Measurements," RAND Corporation Symposium on Aerodynamics of the Upper Atmosphere, June, 1959.

8. Minzner, R. A., and Ripley, W. S., The ARDC Model Atmosphere, 1956. Geophysics Research Directorate, Air Force Cambridge Research Center. ASTIA Document 110233.

9. Goldstein, S., Modern Developments in Fluid Dynamics (Oxford University Press, 1938), p. 495.

10. Lunnon, R. G., "Fluid Resistance to Moving Spheres," Proc. Roy. Soc., Series A, 118, 680-690 (1928).

11. Liebster, H., "Über den Widerstand von Kugeln," Annalen der Physik, 82, 541-562 (1927).

12. Handbook of Chemistry and Physics, 31st Edition, Chemical Rubber Publishing Company, p. 2358.

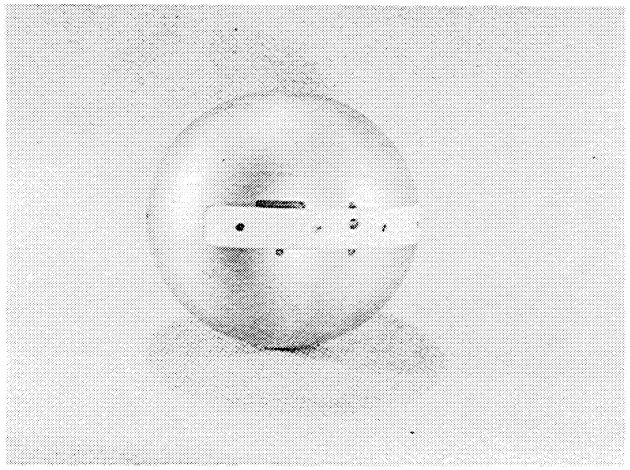

a

b

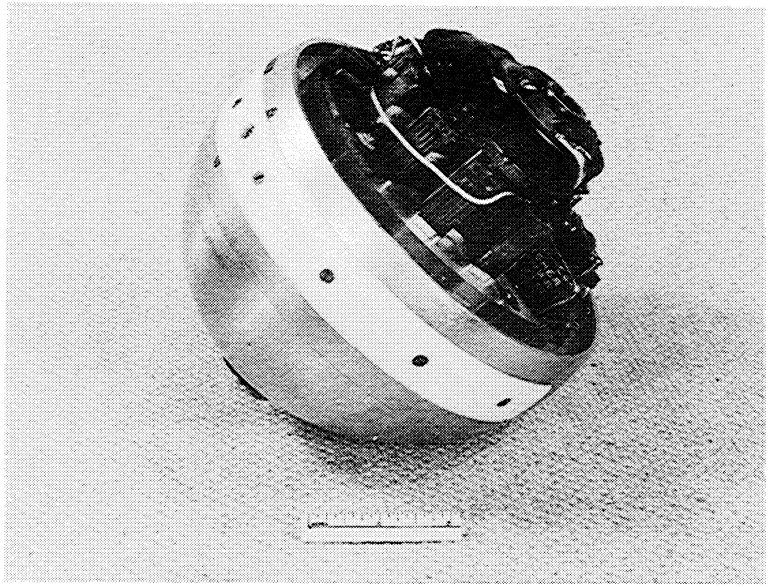

c

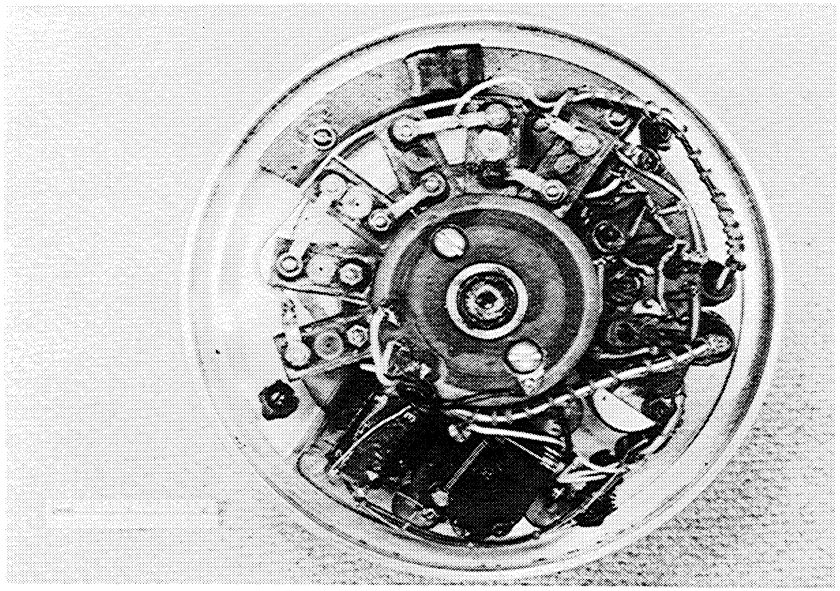

d

Fig. 1. Photographs of sphere with slot antenna.

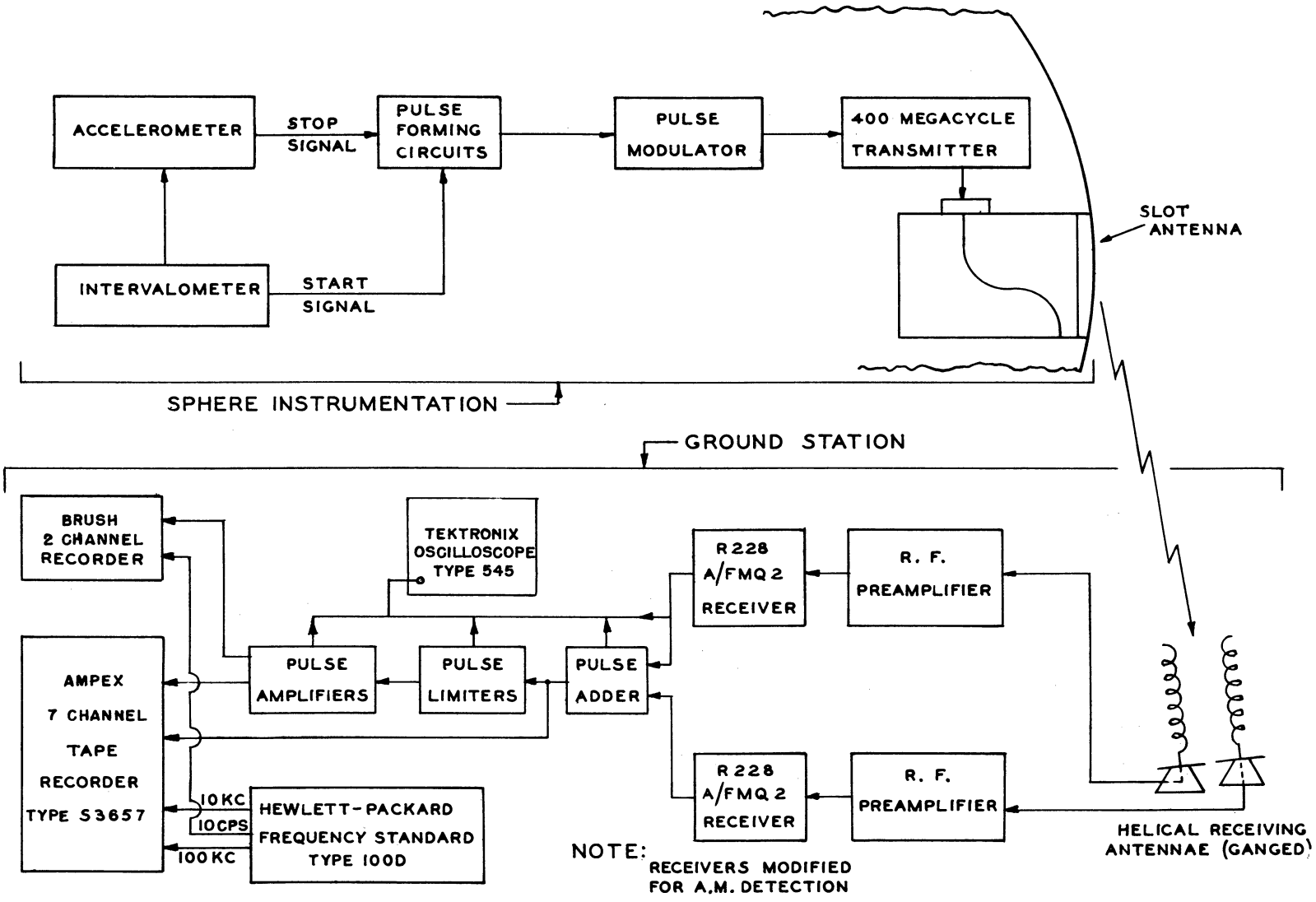

Fig. 3. Block diagram of sphere experiment.

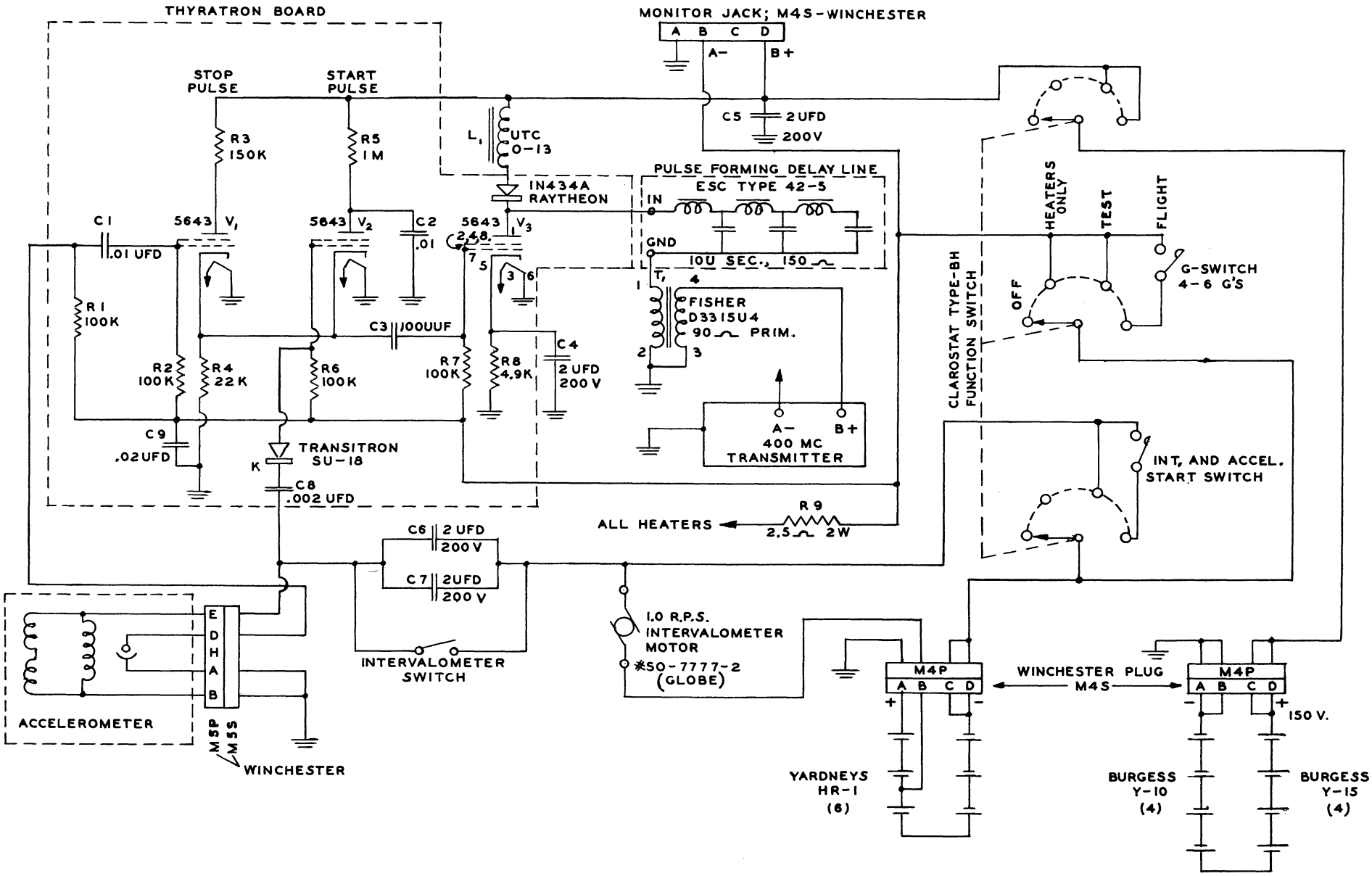

Fig. 4. Schematic of sphere circuitry.

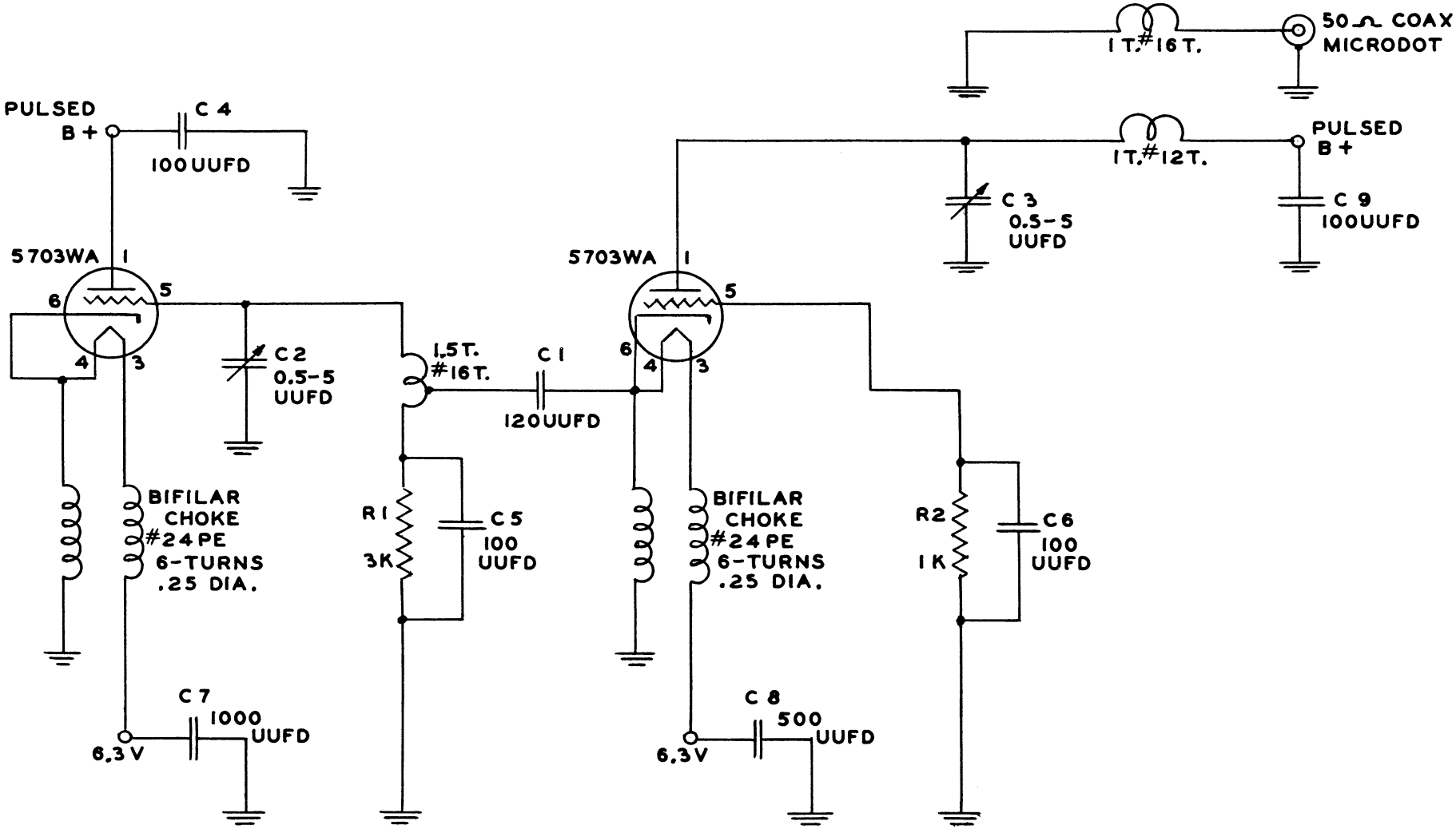

NOTE:

C4 THROUGH C9 ARE BUTTON FEED-THRU SILVER MICA CAPACITORS

Fig. 5. Transmitter schematic.

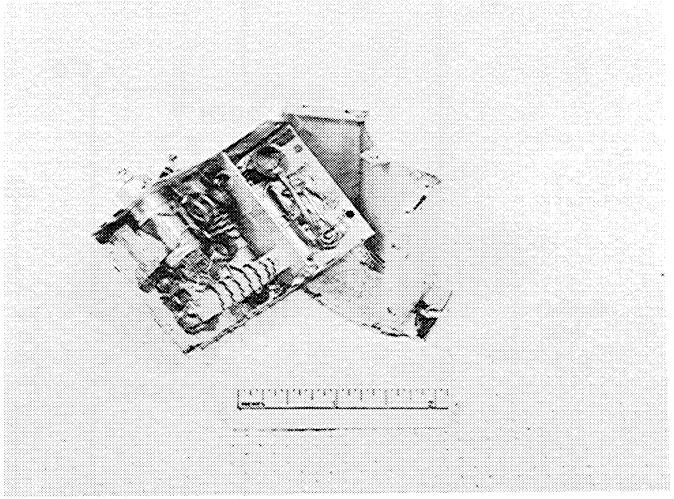

Fig. 6. Transmitter.

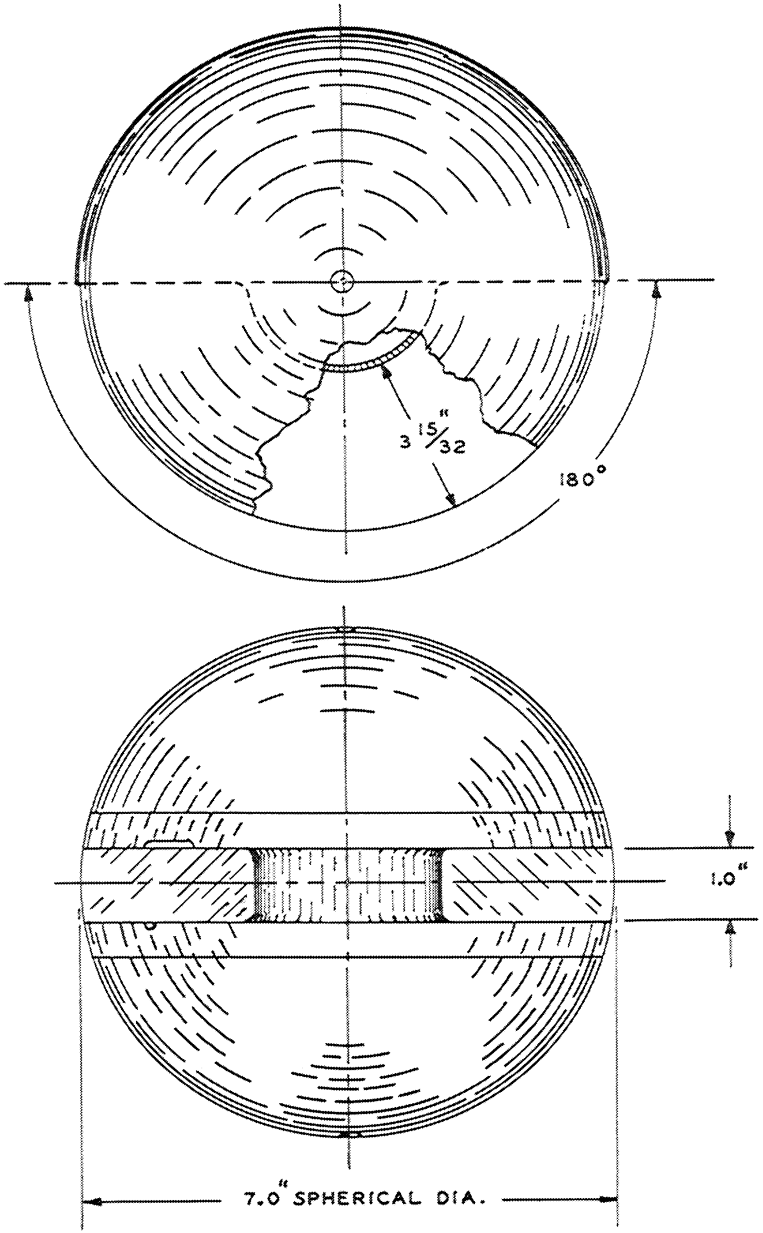

Fig. 7. Sphere antenna.

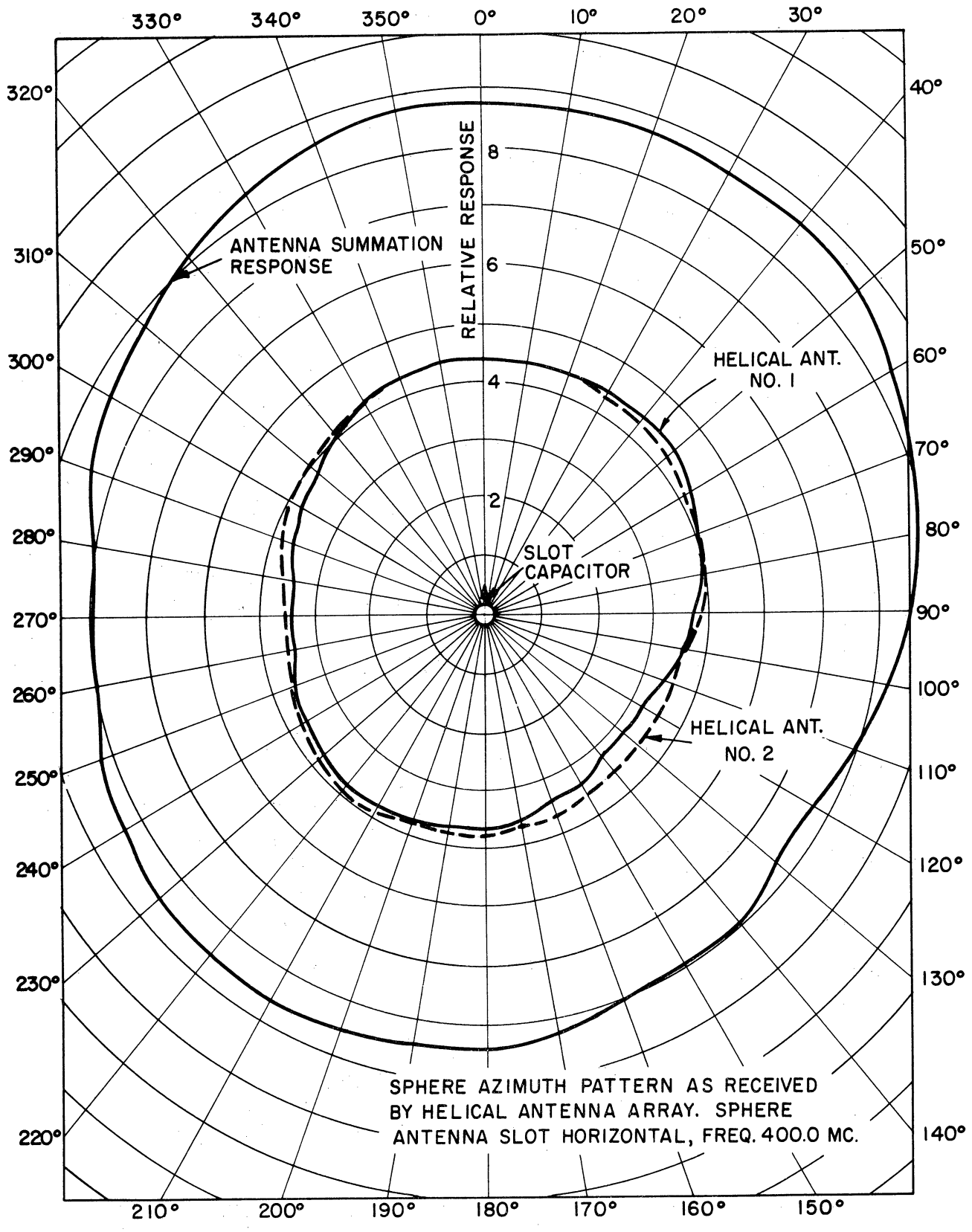

Fig. 8. Sphere-antenna radiation pattern.

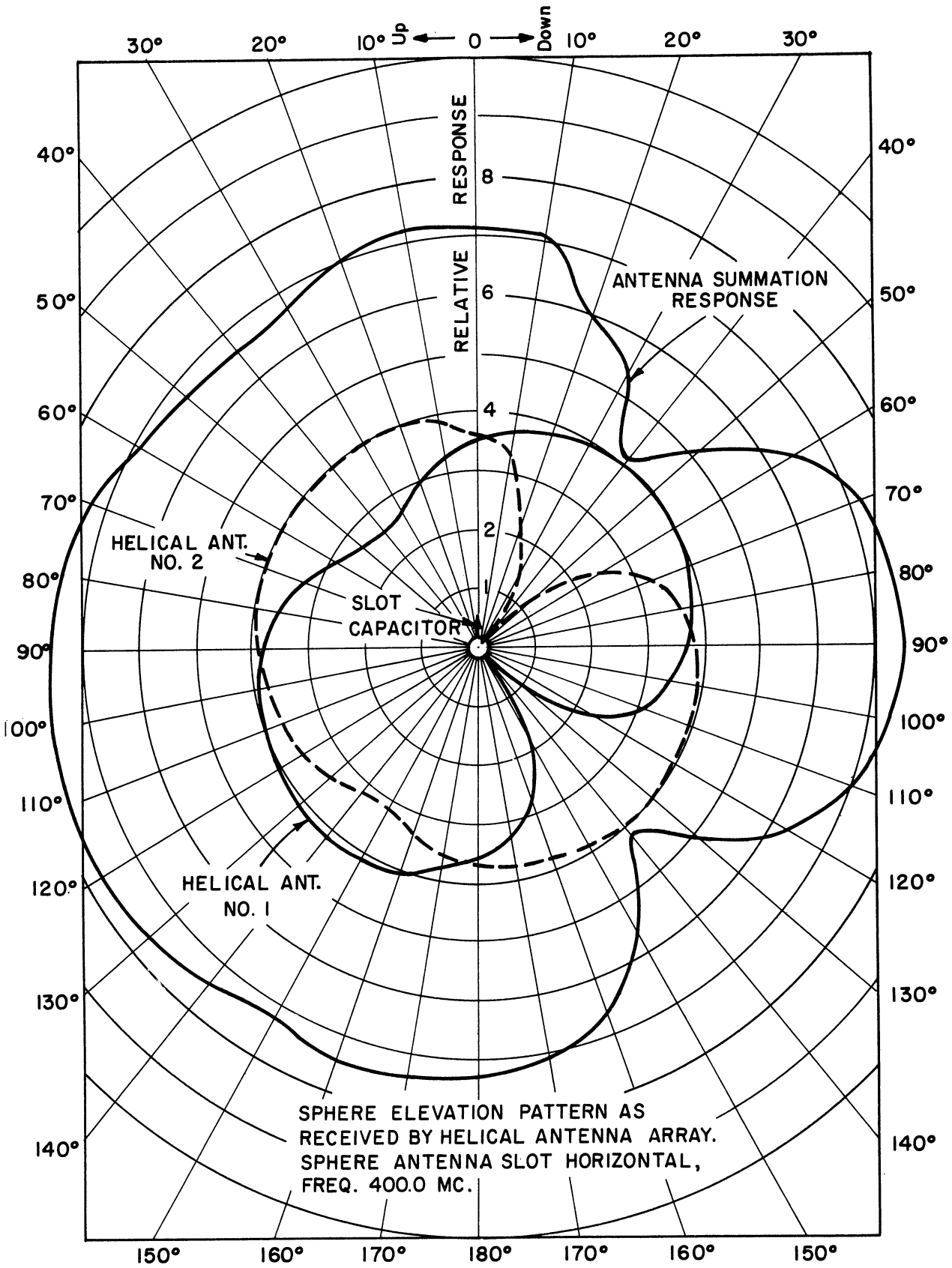

Fig. 9. Sphere-antenna radiation pattern.

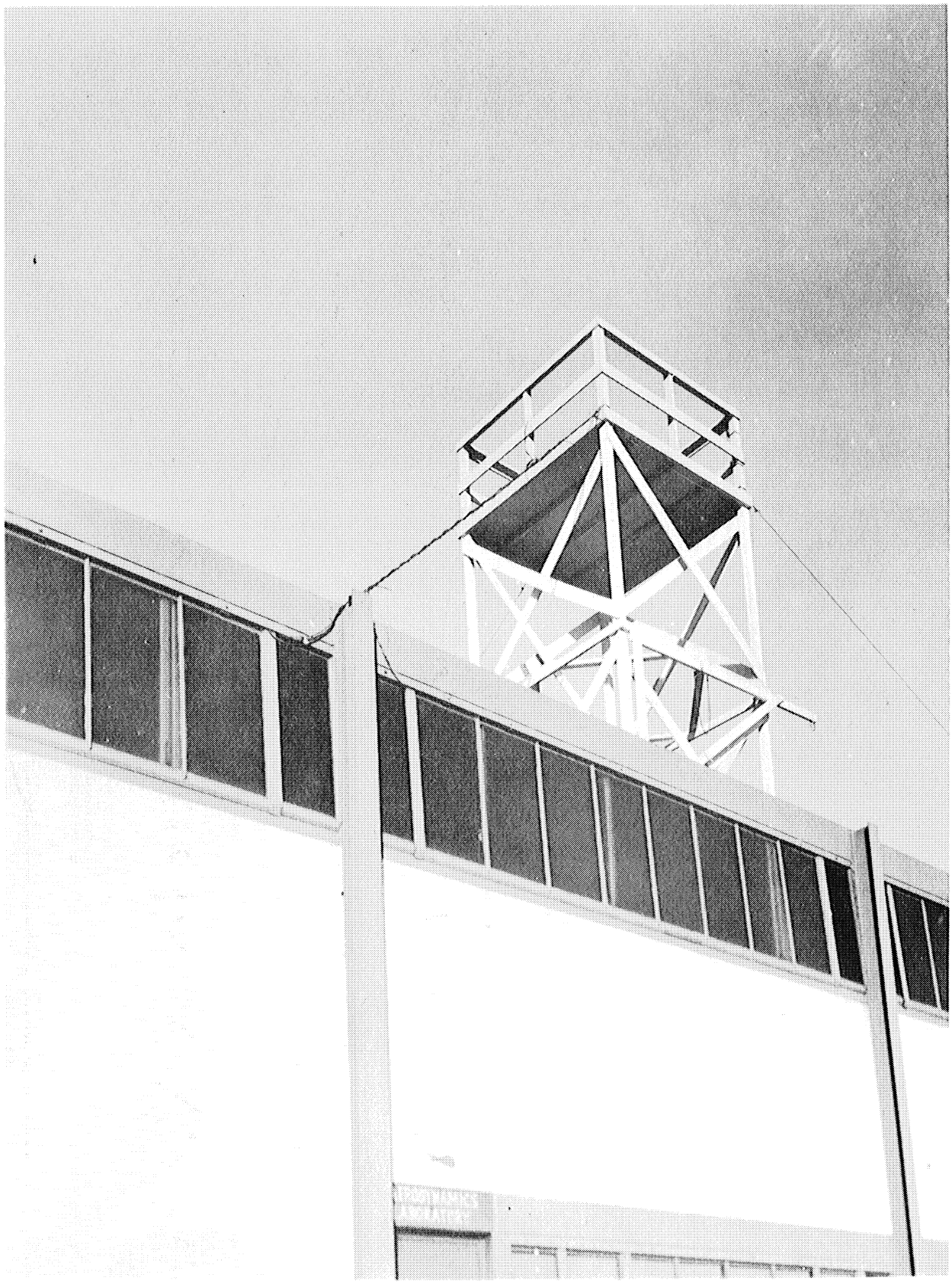

Fig. 10. Antenna test tower.

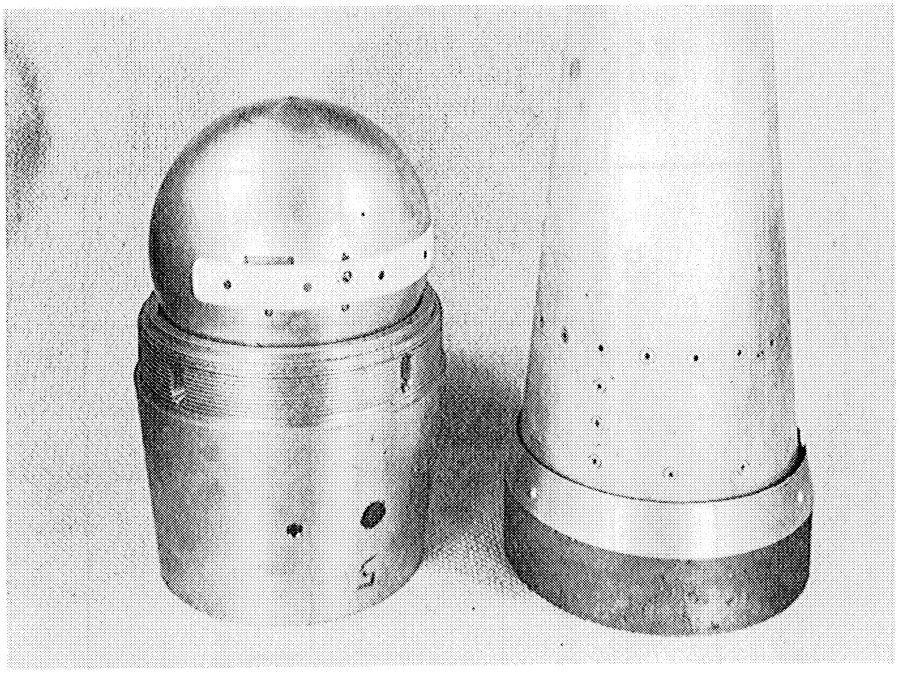

Fig. 12. Sphere in support structure.

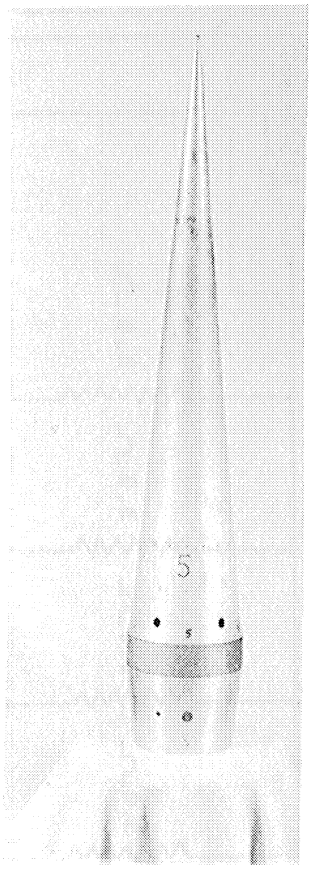

Fig. 13. Assembled nose cone.

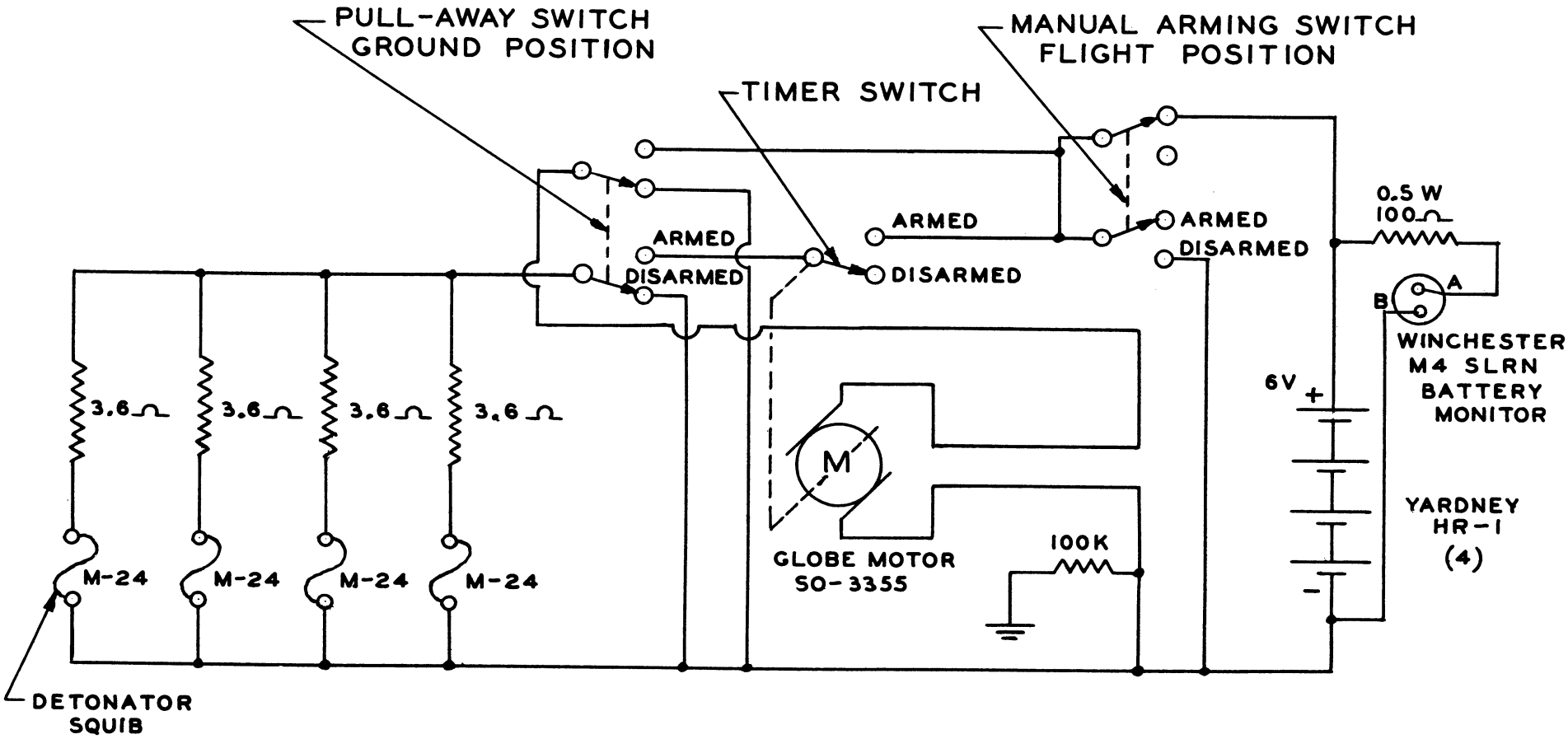

Fig. 14. Schematic of sphere-ejection system in nose cone.

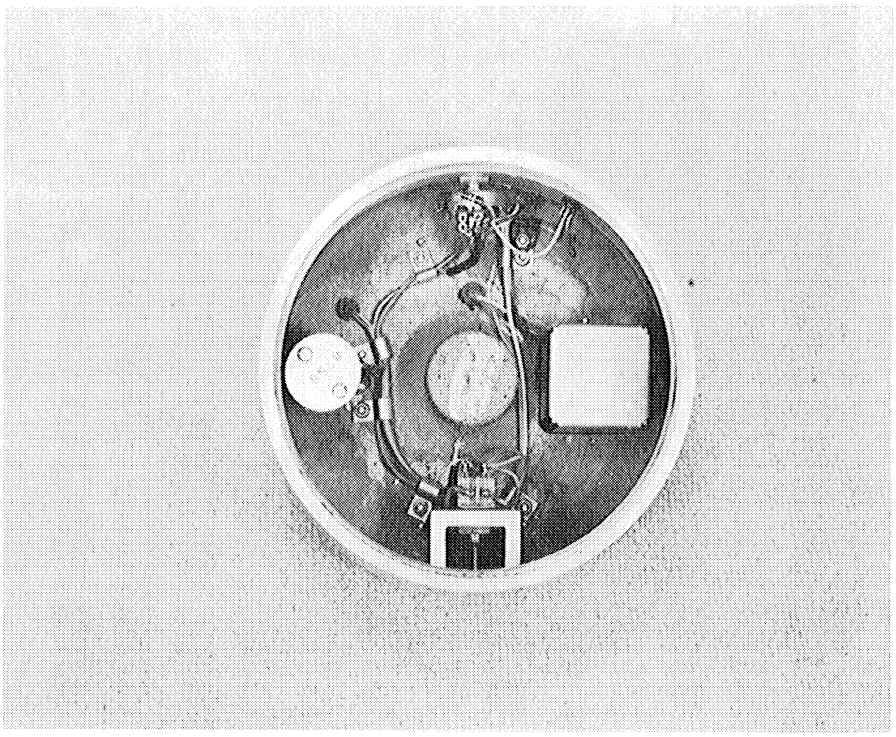

Fig. 15. Ejection timer and circuit (bottom side).

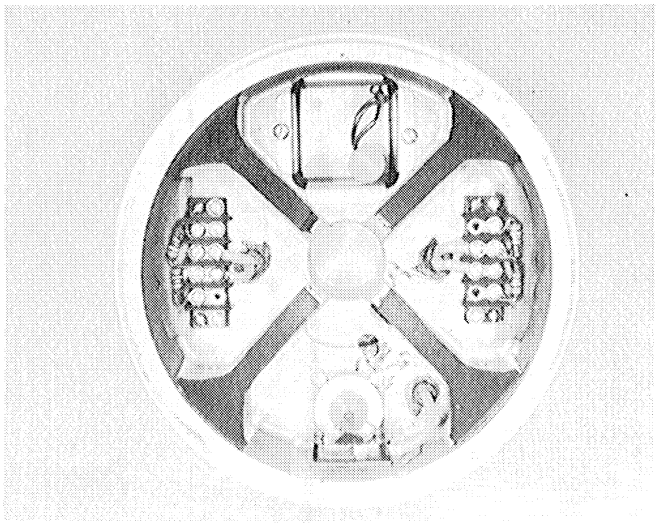

Fig. 16. Ejection timer and circuit (top side).

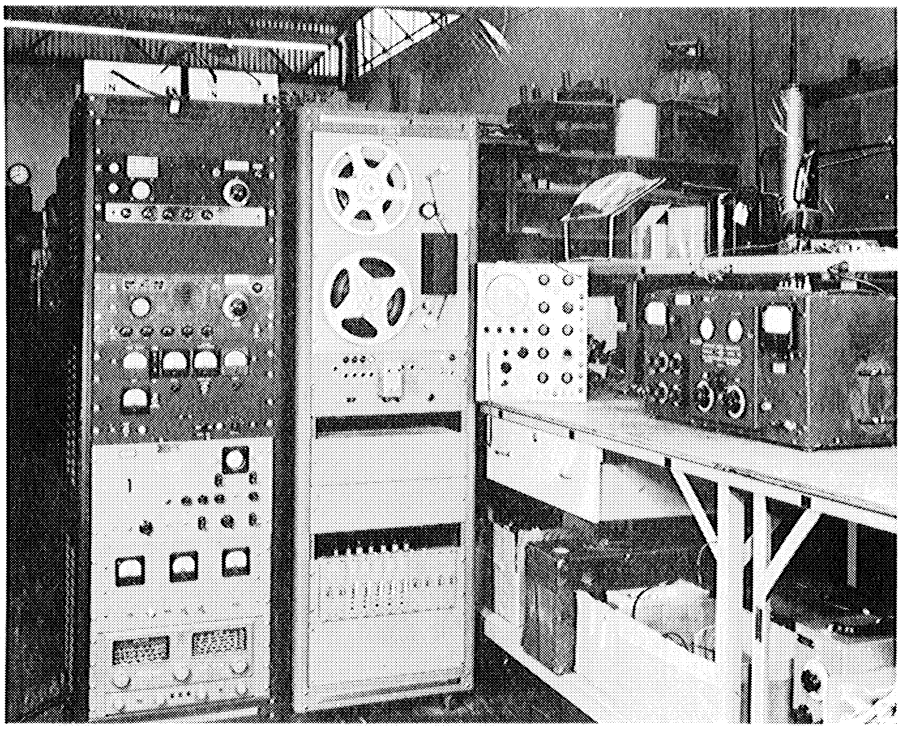

Fig. 17. Ground station.

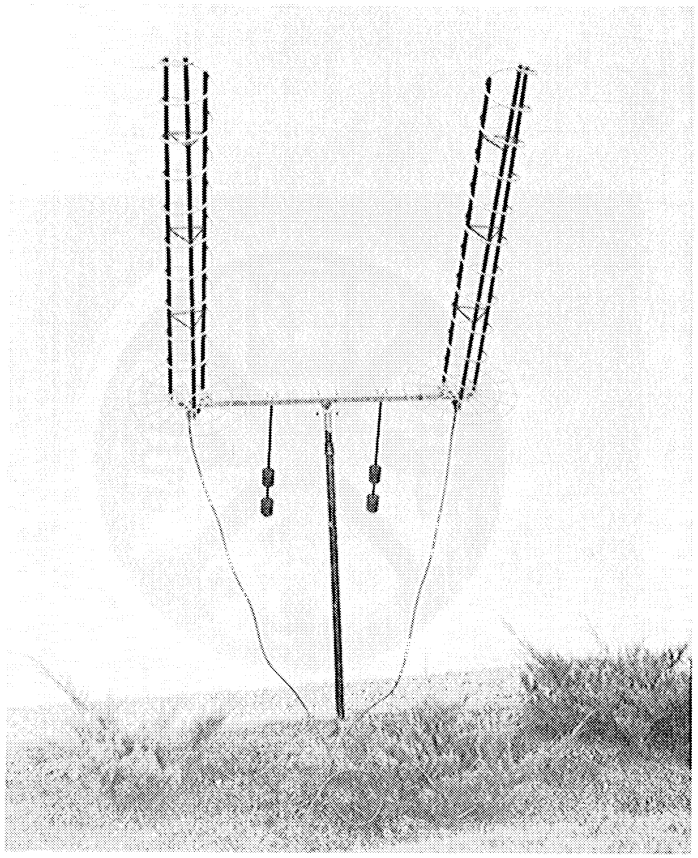

Fig. 18. Ground antenna.

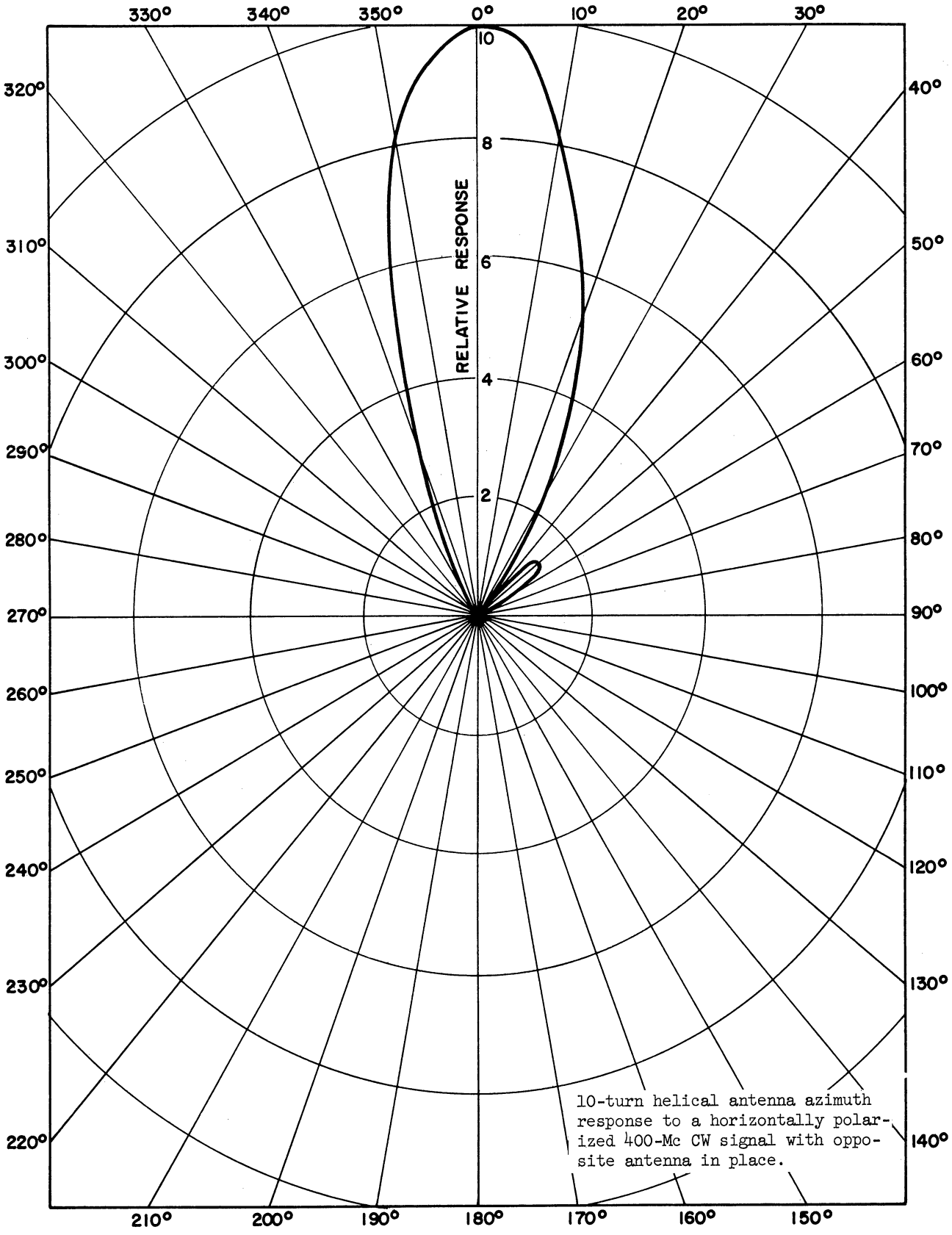

Fig. 19. Ground-antenna radiation pattern.

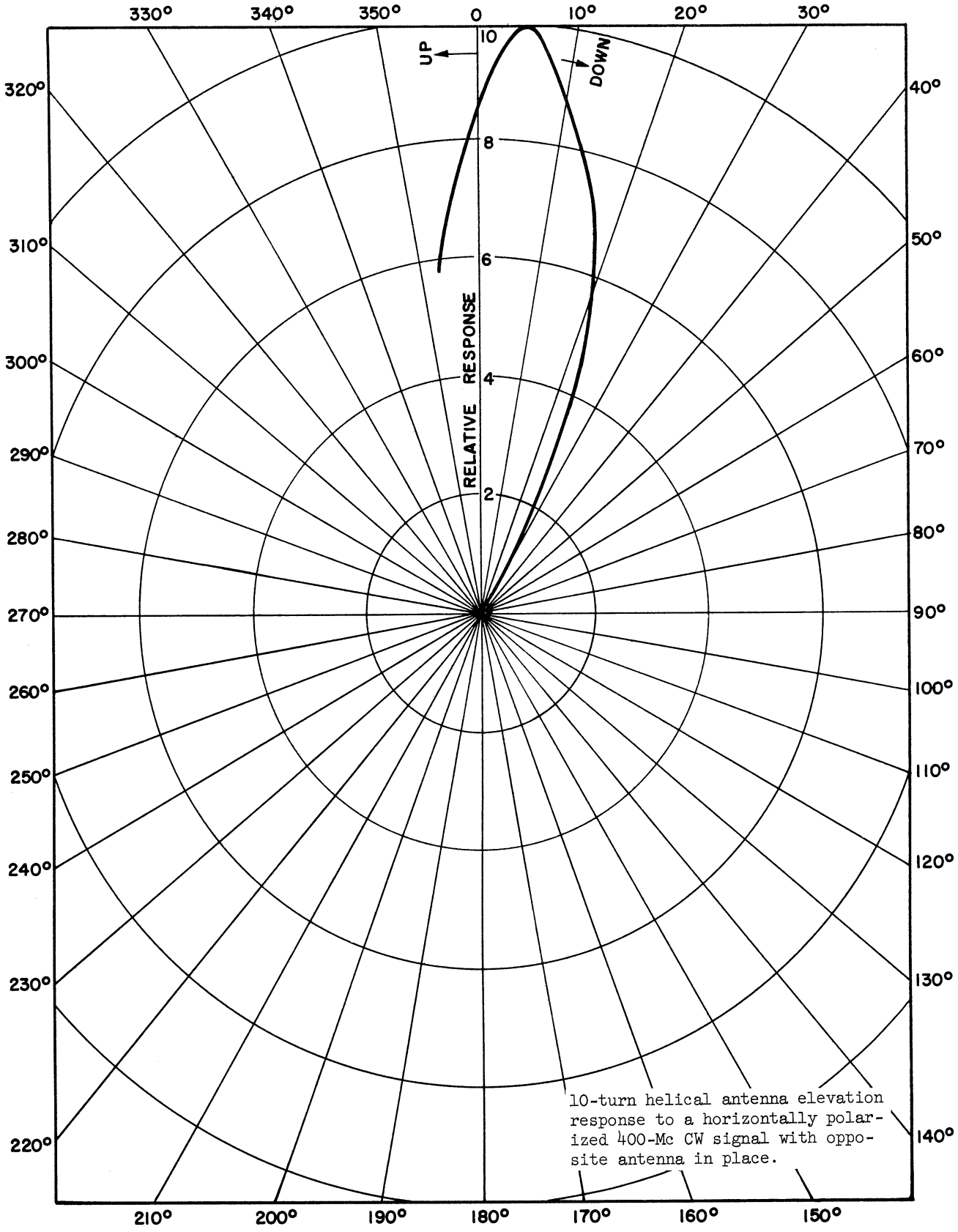

Fig. 20. Ground-antenna radiation pattern.

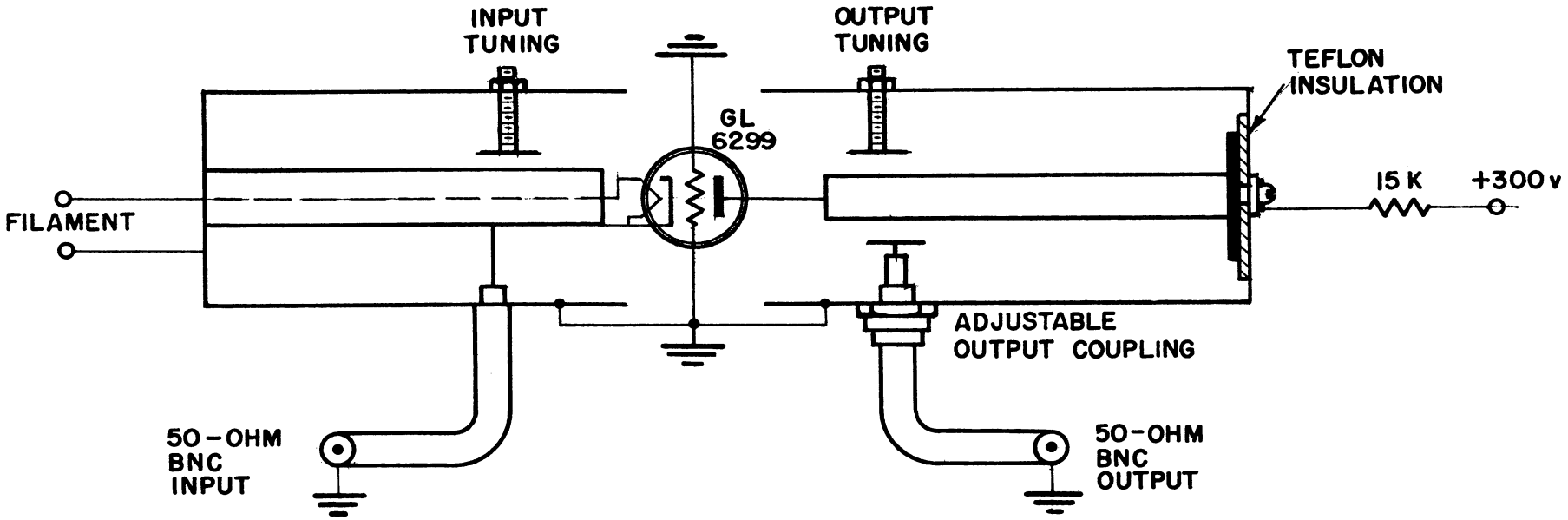

Fig. 21. Pre-amplifier.

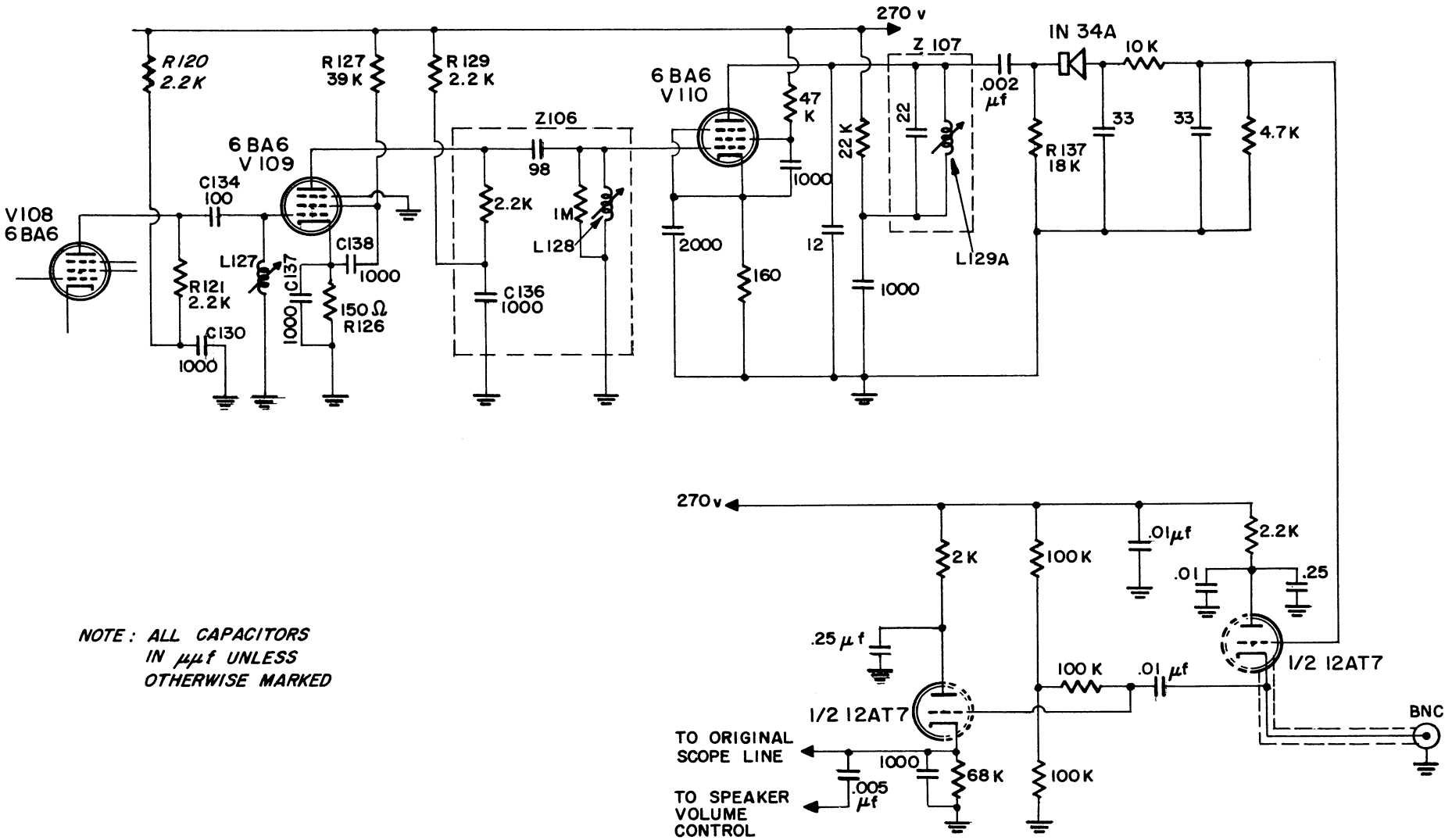

Fig. 22. Modification of receiver circuit.

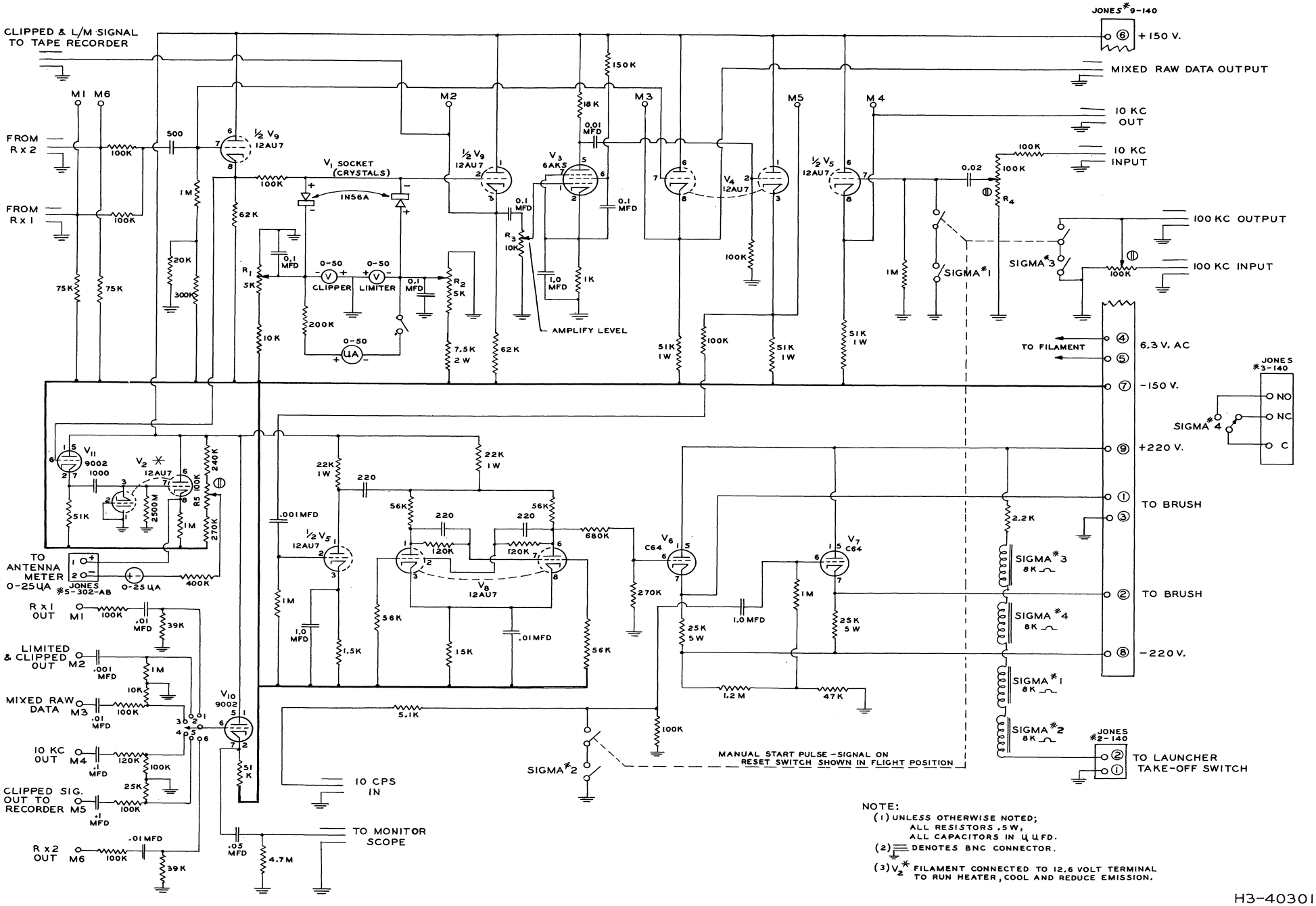

Fig. 23. Pulse-chassis schematic.

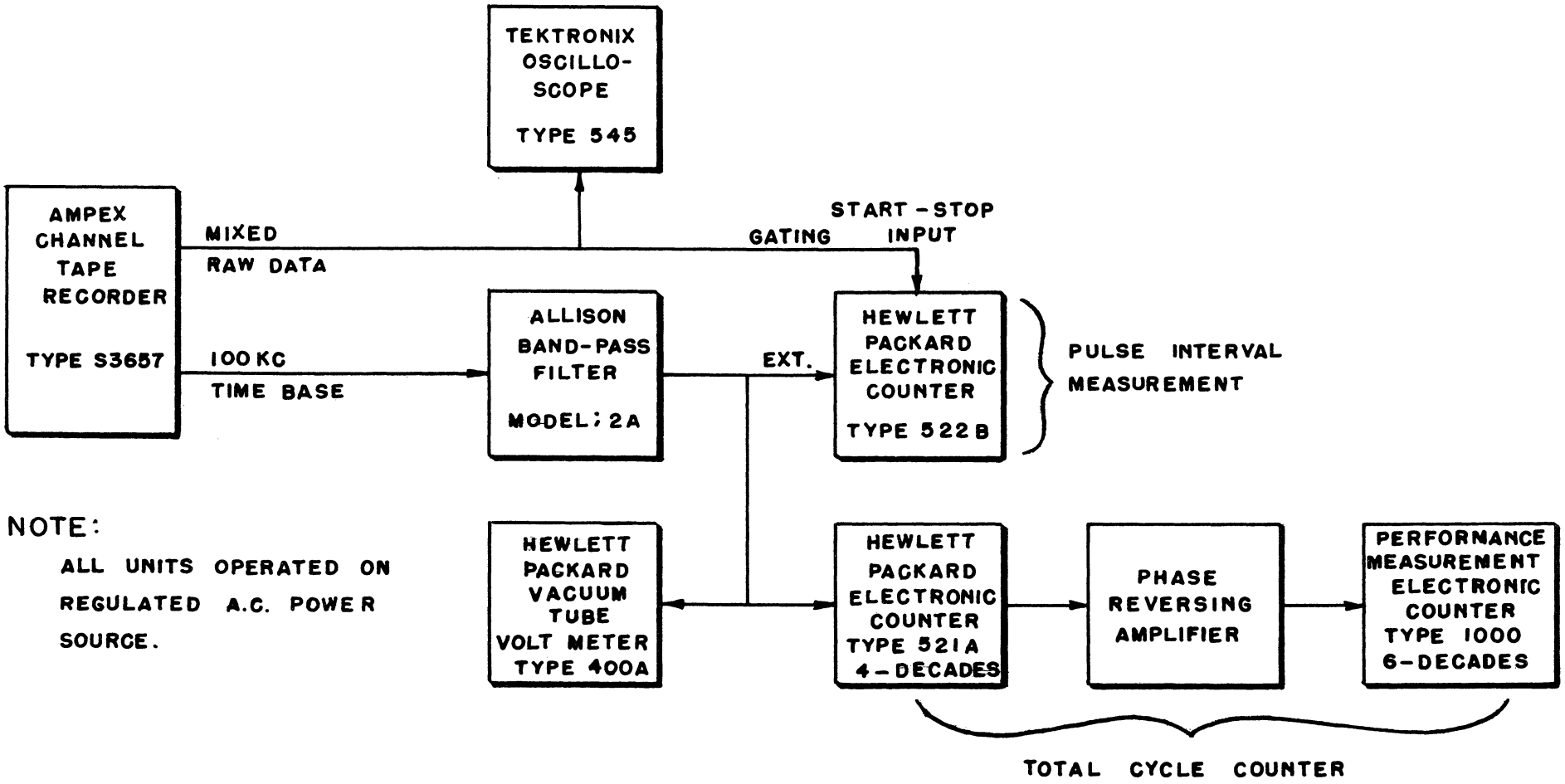

Fig. 24. Block diagram of flight-data playback system.

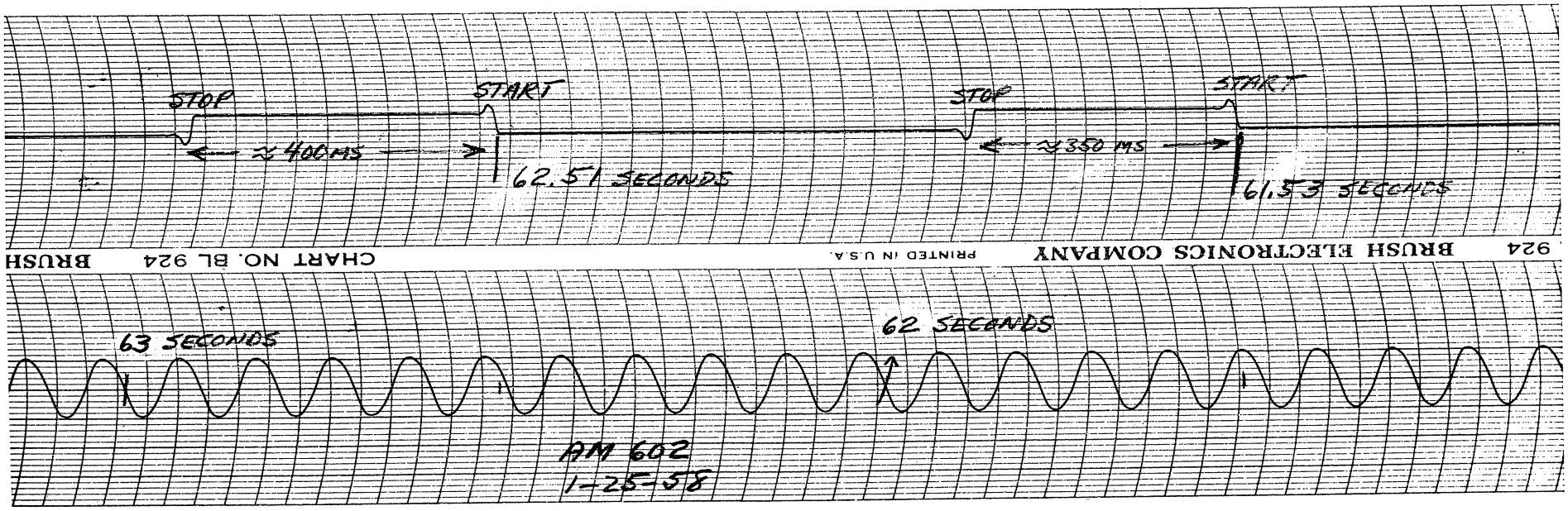

Fig. 25. Section of typical Brush record.

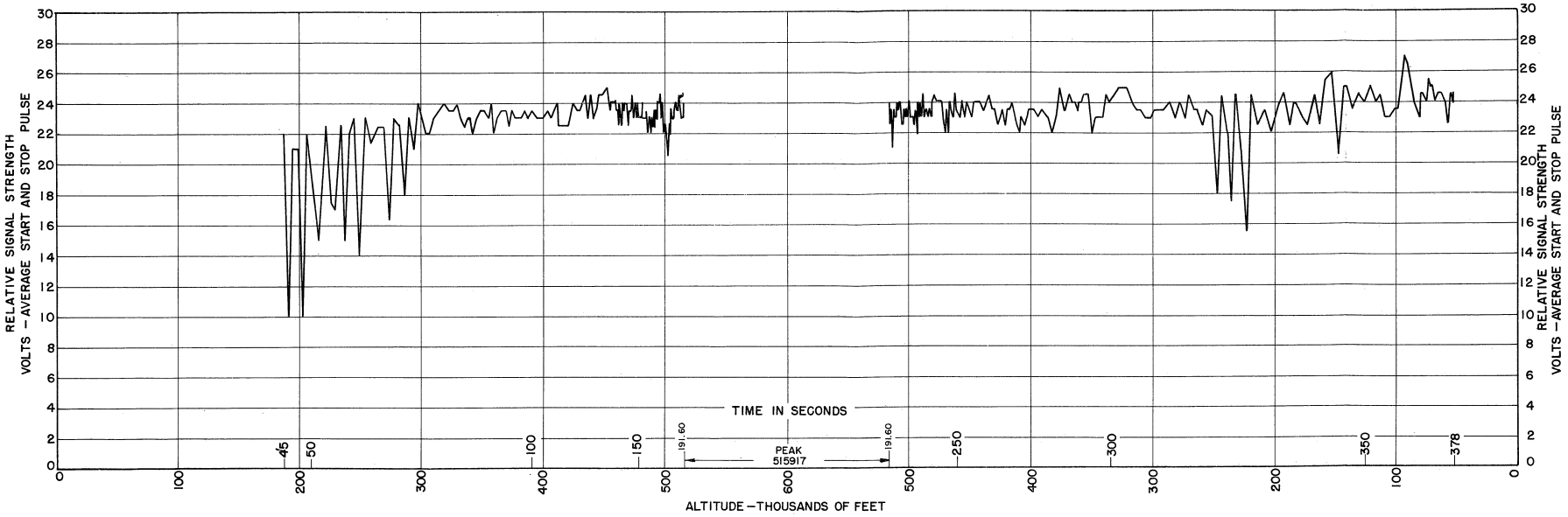

Fig. 26. Signal strength vs. time and altitude (AM 6.02).

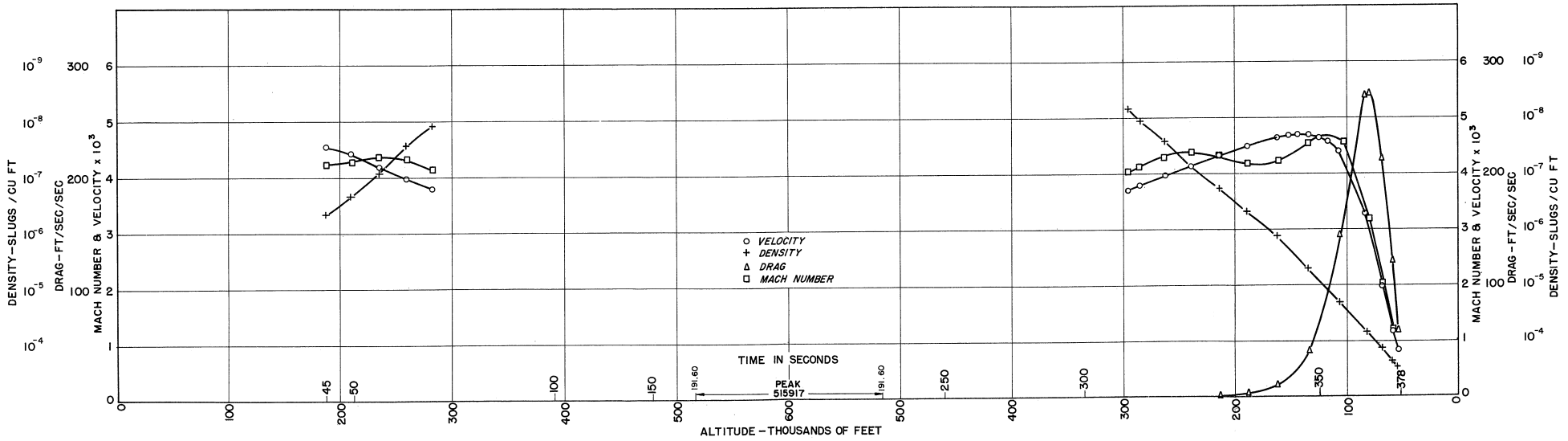

Fig. 27. Velocity, Mach number, drag acceleration, and density vs. time and altitude (AM 6.02).

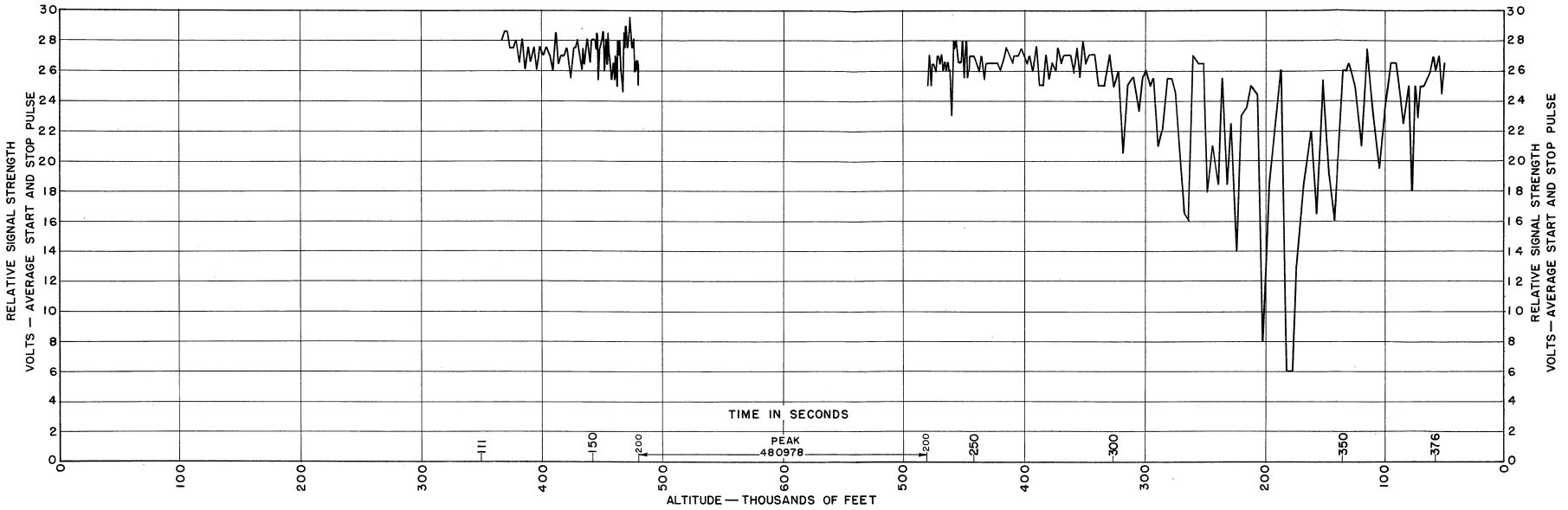

Fig. 28. Signal strength vs. time and altitude (SM 2.10).

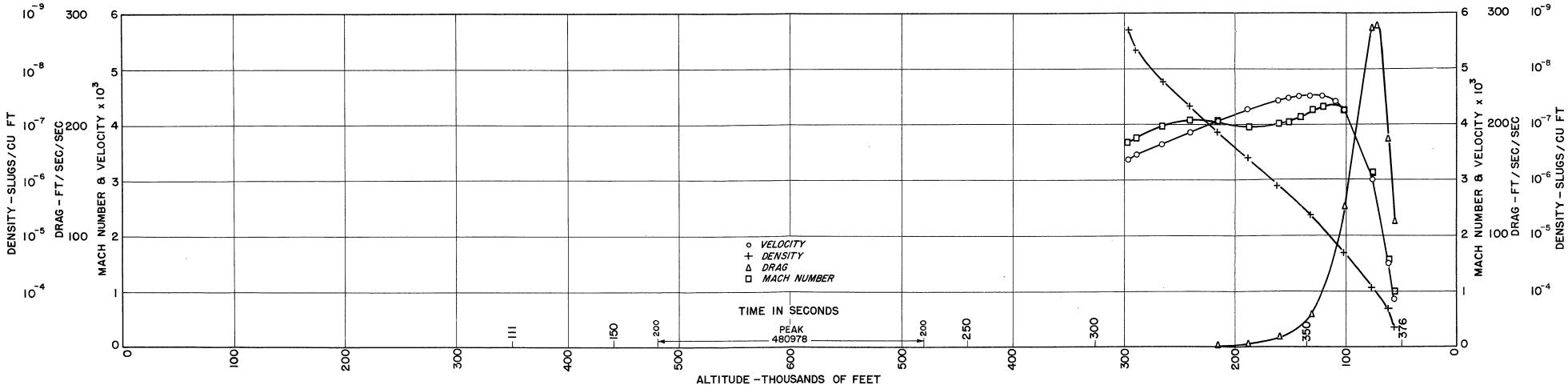

Fig. 29. Velocity, Mach number, drag acceleration, and density vs. time and altitude (SM 2.10).

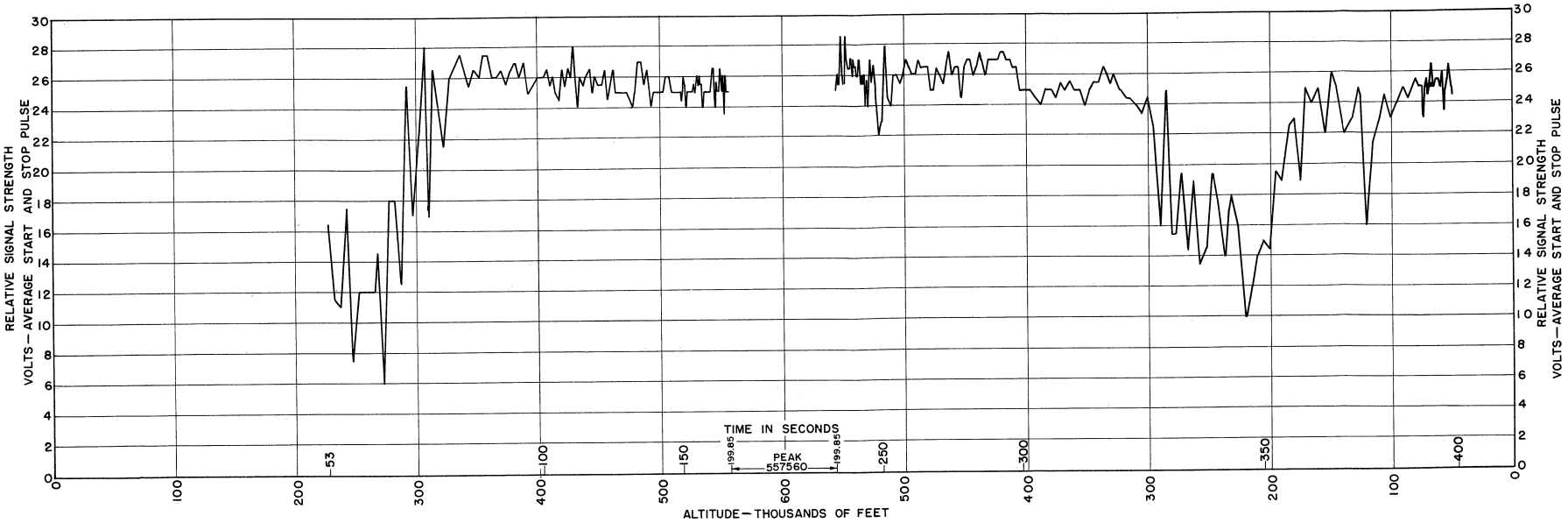

Fig. 30. Signal strength vs. time and altitude (AM 6.03).

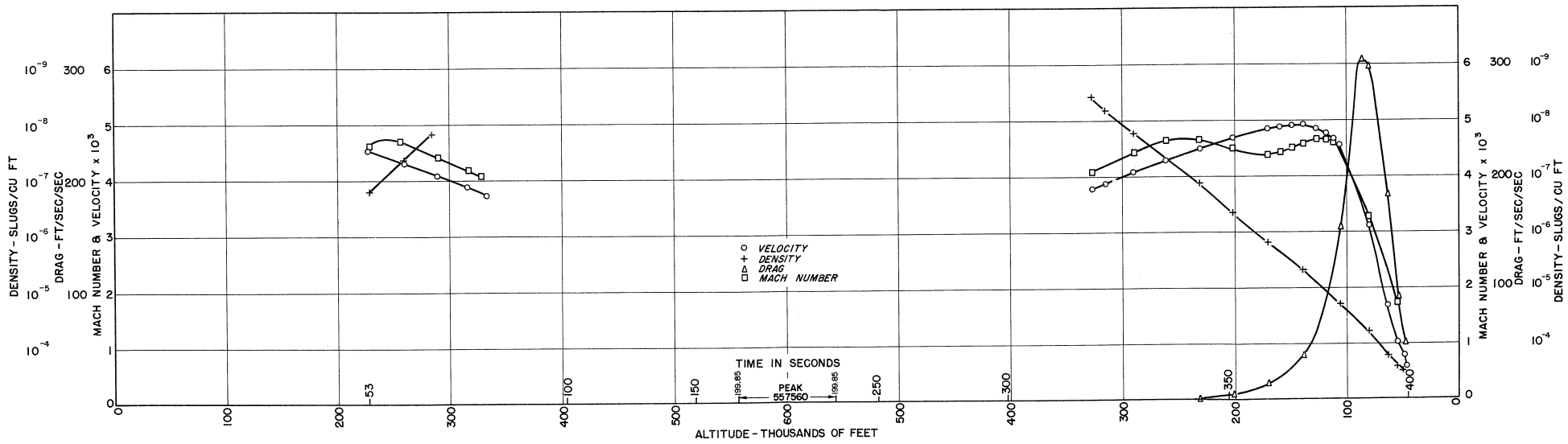

Fig. 31. Velocity, Mach number, drag acceleration, and density vs. time and altitude (AM 6.03).

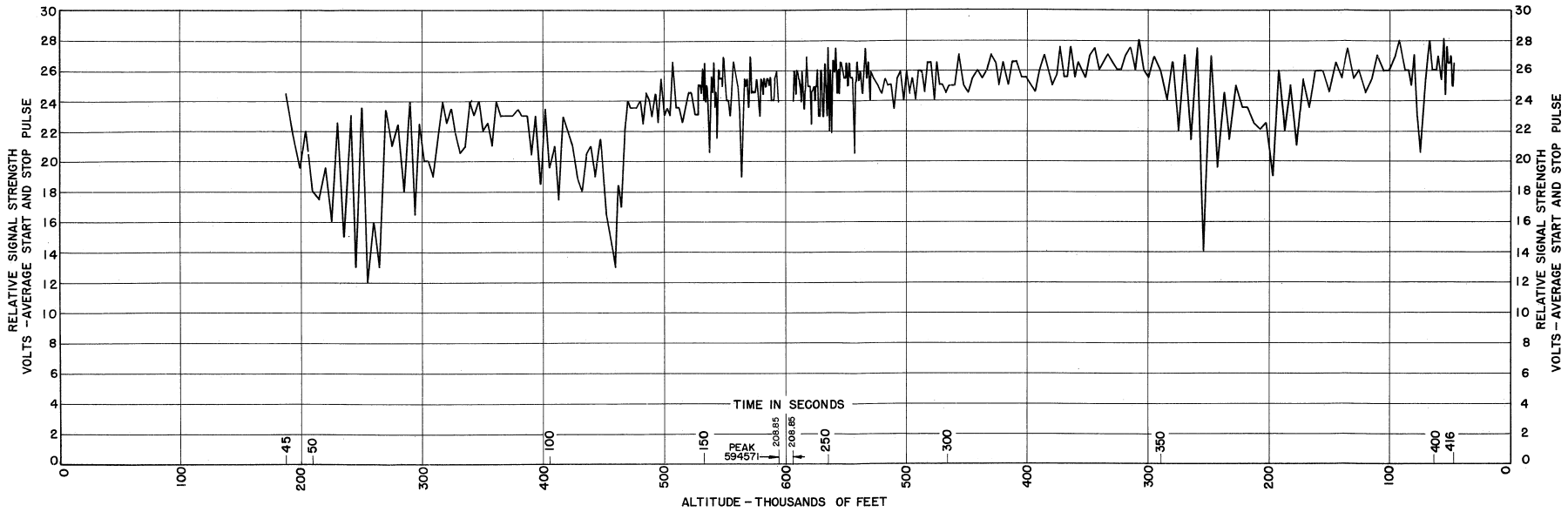

Fig. 32. Signal strength vs. time and altitude (AM 6.05).

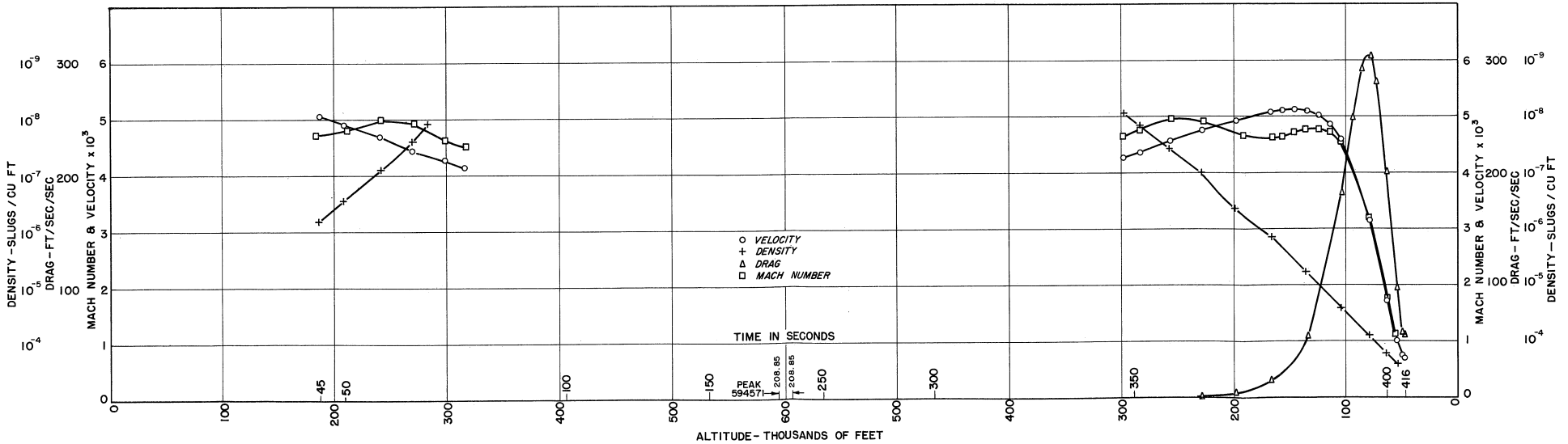

Fig. 33. Velocity, Mach number, drag acceleration, and density vs. time and altitude (AM 6.05).

TABLE II

FLIGHTS OF SMALL-SPHERE EXPERIMENT

Rocket	Date	Local Time	Location	Firing Angle, deg	Peak Altitude, ft	Instrumentation	Remarks
Nike-Deacon (DAN) 1	4/8/55	1019 EST	37.8°N Wallops Island, Va.	75	356,000	Test sphere,* 1/2 w CW at 217 Mc, radar tracking	Rocket test only, successful
Nike-Deacon (DAN) 2	6/24/55	1304 EST	37.8°N Wallops Island, Va.	75	347,339	Sphere,* freq. shift mod. 1/2 w at 217 Mc, radar tracking	Successful
Nike-Cajun AM 6.01	7/6/56	Approx. 1300 EST	37.8°N Wallops Island, Va.	75	426,479	Sphere, keyed 35 w pulses at 400 Mc, radar tracking	Successful
Nike-Cajun AM 6.08	10/27/56	1624 EST (Zone 5 time)	39°58'N, 70°50'W USS Rushmore	85	(tentative) 541,000	Sphere, keyed 35 w pulses at 400 Mc, no radar	Signals only for last minute, no results
Nike-Cajun AM 6.09	11/2/56	1540, Zone 3	48°57'N, 48°22'W USS Rushmore	85	430,600	Sphere, keyed 35 w pulses at 400 Mc, no radar	Successful
Nike-Cajun AM 6.10	11/4/56	1554, Zone 3	57°46'N, 46°41'W USS Rushmore	85	531,200	Sphere, keyed 35 w pulses at 400 Mc, no radar	Successful
Nike-Cajun AM 6.11	11/7/56	1102, Zone 4	64°10'N, 58°05'W USS Rushmore	85	(tentative) 555,000	Sphere, keyed 35 w pulses at 400 Mc, no radar	Partially successful
Nike-Cajun AM 6.12	11/10/56	1117, Zone 4	65°36'N, 58°03'W USS Rushmore	85	529,300	Sphere, keyed 35 w pulses at 400 Mc, no radar	Successful
Nike-Cajun AM 6.02	1/25/58	1312 CST	58°45'N, 94°00'W Ft. Churchill	85	515,100	Sphere, keyed 35 w pulses at 400 Mc, no radar	Successful
Aerobee SM 2.10	1/27/58	1248 CST	58°45'N, 94°00'W Ft. Churchill		481,410	Sphere, keyed 35 w pulses at 400 Mc, with radar and DOVAP	Successful
Nike-Cajun AM 6.03	1/29/58	1306 CST	58°45'N, 94°00'W Ft. Churchill	85	556,800	Sphere, keyed 35 w pulses at 400 Mc, no radar	Successful
Nike-Cajun AM 6.04	3/4/58	0002 CST	58°45'N, 94°00'W Ft. Churchill	85	Unknown, appeared OK	Sphere, keyed 35 w pulses at 400 Mc, no radar	No signals from sphere, no results
Nike-Cajun AM 6.05	3/4/58	1330 CST	58°45'N, 94°00'W Ft. Churchill	85	593,600	Sphere, keyed 35 w pulses at 400 Mc, no radar	Successful

*These spheres had equatorial insulating rings in a dipole arrangement, but were otherwise similar to the later ones.

TABLE VI

RESULTS OF AM 6.12

AM 6.12 DATA ANALYSIS (DOWN LEG DATA)

TIME SECONDS	DRAG ACCELERATION FT/SEC/SEC	VELOCITY VERTICAL FT/SEC	VELOCITY HORIZONTAL FT/SEC	ALTITUDE FEET	ALTITUDE METERS	DRAG COEFFICIENT	DENSITY SL/CU FT X1000	DENSITY KG/CU METER	PRESSURE LB/SQ FT	PRESSURE DYNES/SQ CM	TEMPERATURE FAHRENHEIT	TEMPERATURE CENTIGRADE
195.79	.000	.	500.	529300.	161331.							
319.74	.118	-3824.	521.	293212.	89371.	1.234	.00001661	.00000856				
322.38	.133	-3906.	522.	283009.	86261.	1.220	.00001816	.00000936				
323.26	.140	-3934.	523.	279560.	85210.	1.214	.00001896	.00000977				
324.18	.106	-3962.	523.	275928.	84103.	1.239	.00001386	.00000714				
324.96	.262	-3987.	523.	272829.	83158.	1.153	.00003639	.00001875				
326.72	.324	-4041.	524.	265765.	81005.	1.131	.00004466	.00002302				
327.62	.342	-4069.	524.	262116.	79893.	1.125	.00004676	.00002410				
328.52	.335	-4097.	524.	258441.	78773.	1.125	.00004515	.00002327				
330.33	.311	-4154.	525.	250975.	76497.	1.131	.00004062	.00002094				
331.21	.460	-4181.	525.	247309.	75380.	1.095	.00006124	.00003156	.03048	14.594	-170.	-113.
332.13	.402	-4209.	525.	243449.	74203.	1.111	.00005204	.00002682	.03735	17.882	-42.	-41.
333.07	.467	-4239.	526.	239479.	72993.	1.100	.00006024	.00003105	.04436	21.237	-31.	-35.
333.91	.617	-4265.	526.	235908.	71905.	1.076	.00008036	.00004142	.05222	24.999	-82.	-63.
334.81	.648	-4292.	526.	232058.	70731.	1.075	.00008346	.00004302	.06216	29.759	-26.	-33.
338.37	1.288	-4401.	527.	216586.	66015.	1.021	.00016619	.00008565	.12076	57.818	-37.	-38.
339.26	1.515	-4428.	527.	212657.	64818.	1.008	.00019555	.00010079	.14315	68.538	-34.	-37.
340.17	1.732	-4455.	528.	208616.	63586.	.999	.00022305	.00011496	.16983	81.314	-17.	-27.
341.06	1.912	-4482.	528.	204640.	62374.	.992	.00024498	.00012626	.19922	95.384	14.	-10.
343.73	3.344	-4559.	528.	192572.	58696.	.962	.00042736	.00022026	.32426	155.254	-18.	-28.
344.63	3.868	-4584.	528.	188458.	57442.	.959	.00049017	.00025263	.38390	183.812	-4.	-20.
346.42	4.920	-4633.	528.	180210.	54928.	.956	.00061297	.00031593	.52736	252.500	42.	5.
347.32	6.216	-4656.	528.	176030.	53654.	.951	.00077012	.00039692	.61855	296.161	8.	-14.
348.21	7.064	-4679.	528.	171877.	52388.	.949	.00086946	.00044812	.72636	347.782	27.	-3.
349.11	8.504	-4700.	527.	167656.	51102.	.945	.00104162	.00053685	.85390	408.848	18.	-8.
350.01	10.250	-4720.	527.	163418.	49810.	.941	.00125024	.00064437	1.00758	482.430	10.	-13.
350.91	11.950	-4739.	526.	159161.	48512.	.938	.00145142	.00074806	1.18973	569.642	18.	-8.
351.82	15.000	-4756.	525.	154842.	47196.	.933	.00181872	.00093737	1.41302	676.552	-7.	-22.
352.74	19.100	-4769.	524.	150461.	45860.	.927	.00231712	.00119424	1.69940	813.672	-33.	-36.
353.64	21.930	-4779.	522.	146164.	44551.	.923	.00265959	.00137075	2.03861	976.085	-14.	-26.
354.56	27.110	-4786.	520.	141764.	43210.	.918	.00329701	.00169928	2.45361	1174.788	-27.	-33.
355.47	33.250	-4788.	517.	137409.	41882.	.913	.00406310	.00209412	2.96151	1417.970	-35.	-38.
356.37	39.680	-4784.	514.	133102.	40570.	.909	.00488045	.00251538	3.57258	1710.551	-34.	-37.
357.28	48.190	-4773.	510.	128754.	39244.	.906	.00597552	.00307978	4.32125	2069.013	-39.	-40.
358.18	57.220	-4754.	506.	124467.	37938.	.906	.00715154	.00368590	5.21485	2496.867	-35.	-38.
359.09	69.720	-4726.	500.	120154.	36623.	.906	.00882023	.00454595	6.30799	3020.265	-43.	-42.
359.99	85.000	-4685.	493.	115920.	35332.	.906	.01094175	.00563938	7.63637	3656.294	-54.	-48.
360.87	97.790	-4633.	485.	111820.	34083.	.906	.01287364	.00663507	9.18942	4399.891	-44.	-43.
361.76	119.390	-4566.	475.	107727.	32835.	.906	.01618923	.00834393	11.07824	5304.260	-61.	-52.
362.66	143.050	-4477.	463.	103658.	31595.	.906	.02017708	.01039927	13.42931	6429.952	-72.	-58.
363.58	166.940	-4364.	449.	99592.	30356.	.906	.02477962	.01277141	16.33650	7821.917	-76.	-60.
364.50	194.270	-4228.	432.	95639.	29151.	.908	.03064955	.01579678	19.82113	9490.356	-83.	-64.
365.41	217.590	-4071.	413.	91863.	28000.	.913	.03685650	.01899584	23.88079	11434.122	-83.	-64.
366.30	* 242.700	-3896.	393.	88319.	26920.	.918	.04464270	.02300885	28.48253	13637.437	-88.	-67.
367.17	258.950	-3706.	371.	85012.	25912.	.924	.05229357	.02695211	33.59453	16085.059	-86.	-66.
368.08	* 275.500	-3493.	347.	81737.	24913.	.931	.06217131	.03204309	39.57324	18947.665	-89.	-68.
369.00	* 281.900	-3268.	322.	78627.	23966.	.939	.07209140	.03715591	46.23850	22138.991	-86.	-66.
369.89	* 285.300	-3045.	297.	75819.	23110.	.947	.08332828	.04294740	53.20969	25476.800	-88.	-67.
370.79	278.900	-2821.	272.	73180.	22305.	.955	.09412063	.04850977	60.69466	29060.301	-84.	-65.
371.64	* 273.300	-2615.	250.	70870.	21601.	.969	.10588358	.05457240	68.07981	32596.613	-86.	-66.
372.62	* 257.900	-2387.	225.	68420.	20854.	.992	.11707017	.06033796	76.81787	36780.396	-78.	-61.
373.50	* 243.600	-2195.	204.	66404.	20240.	1.010	.12847408	.06621554	84.73772	40572.421	-76.	-60.
374.38	232.900	-2015.	184.	64552.	19675.	1.010	.14588100	.07518707	92.86459	44463.563	-89.	-68.
375.27	217.600	-1844.	166.	62836.	19152.	1.010	.16282982	.08392249	101.34458	48523.783	-98.	-72.
376.18	197.400	-1685.	149.	61231.	18663.	1.010	.17696036	.09120537	110.07665	52704.700	-98.	-72.
377.10	177.100	-1542.	134.	59747.	18211.	1.010	.18943434	.09763446	118.78533	56874.416	-95.	-71.
378.01	162.200	-1418.	120.	58400.	17800.	1.010	.20542202	.10587451	127.3017	60952.039	-99.	-73.
378.88	145.000	-1313.	109.	57213.	17439.	1.010	.21435699	.11047959	135.2888	64776.251	-92.	-69.
379.75	135.600	-1219.	99.	56112.	17103.	.986	.23817867	.12275729	143.2660	68595.767	-110.	-79.
380.61	120.900	-1136.	90.	55100.	16795.	.951	.25353565	.13067227	151.2434	72415.316	-113.	-81.
381.50	109.700	-1063.	82.	54122.	16496.	.919	.27237279	.14038094	159.4875	76362.608	-119.	-84.
382.39	101.200	-998.	75.	53206.	16217.	.890	.29425489	.15165897	167.8091	80346.994	-128.	-89.
383.28	94.590	-939.	68.	52344.	15954.	.857	.32240925	.16616973	176.3220	84422.947	-142.	-97.
384.18	88.650	-886.	63.	51523.	15704.	.782	.37268056	.19207956	185.4564	88796.524	-170.	-113.
385.07	81.560	-839.	57.	50756.	15470.	.715	.41814519	.21551203	195.1731	93448.870	-188.	-123.

AM 6.12 DATA ANALYSIS (UP LEG DATA)

TIME SECONDS	DRAG ACCELERATION FT/SEC/SEC	VELOCITY VERTICAL FT/SEC	VELOCITY HORIZONTAL FT/SEC	ALTITUDE FEET	ALTITUDE METERS	DRAG COEFFICIENT	DENSITY SL/CU FT X1000	DENSITY KG/CU METER	PRESSURE LB/SQ FT	PRESSURE DYNES/SQ CM	TEMPERATURE FAHRENHEIT	TEMPERATURE CENTIGRADE
195.79	.000	.	500.	529300.	161331.							
62.86	.240	4105.	525.	257618.	78522.	1.157	.00003135	.00001616				
61.90	.299	4135.	525.	253662.	77316.	1.135	.00003923	.00002022	.02342	11.214	-112.	-80.
60.93	.261	4166.	525.	249636.	76089.	1.147	.00003340	.00001721	.02801	13.411	29.	-2.
59.96	.386	4197.	526.	245580.	74853.	1.113	.00005016	.00002585	.03327	15.931	-74.	-59.
58.98	.507	4228.	526.	241451.	73594.	1.090	.00006628	.00003416	.04079	19.531	-102.	-74.
57.05	.693	4290.	527.	233232.	71089.	1.067	.00008995	.00004636	.06087	29.143	-66.	-55.
55.09	.863	4353.	528.	224761.	68507.	1.053	.00011031	.00005686	.08752	41.904	3.	-17.
54.09	1.023	4386.	529.	220391.	67175.	1.040	.00013047	.00006724	.10408	49.833	5.	-15.
53.10	1.263	4418.	529.	216033.	65847.	1.023	.00016139	.00008318	.12408	59.409	-12.	-25.
52.08	1.871	4452.	530.	211510.	64468.	.989	.00024368	.00012559	.15261	73.069	-95.	-71.

AM 6.12 DOWN LEG

ALTITUDE METERS	DENSITY KG/CU METER	PRESSURE DYNES/SQ CM	TEMPERATURE CENTIGRADE
16000.	.17043029	84015.124	-101.5
20000.	*.07110827	42286.146	-66.0
24000.	*.03697585	22010.564	-65.8
28000.	*.01911642	11438.746	-64.7
32000.	.00965334	6041.731	-55.2
36000.	.00499913	3315.760	-42.1
40000.	.00274962	1856.433	-38.0
44000.	.00151128	1053.082	-30.5
48000.	.00082508	609.339	-15.9
52000.	.00047816	365.065	-7.2
56000.	.00028719	220.519	-5.7
58696.	.00022026	155.254	-27.6
64000.	.00010933	76.661	-28.9
66015.	.00008565	57.818	-38.0
72000.	.00003743	24.632	-43.9

*Smoothed accelerometer data

AM 6.12 UP LEG

ALTITUDE METERS	DENSITY KG/CU METER	PRESSURE DYNES/SQ CM	TEMPERATURE CENTIGRADE
64000.	.00014445	78.387	-84.1
68000.	.00006060	44.759	-15.9
72000.	.00004149	25.194	-61.6
76000.	.00002098	13.544	-48/3

Note: This is an unedited tabulation of computer calculations. Some points at the highest and lowest altitudes lie outside the valid range of measurement of the sphere instrumentation. See page 24 for a discussion. See the plotted curves for the final edited data of density and temperature vs. altitude.

TABLE VIII

RESULTS OF SM 2.10

SM 2.10 DATA ANALYSIS

TIME SECONDS	DRAG ACCELERATION FT/SEC/SEC	VELOCITY VERTICAL FT/SEC	VELOCITY HORIZONTAL FT/SEC	ALTITUDE FEET	ALTITUDE METERS	DRAG COEFFICIENT	DENSITY SL/CU FT X1000	DENSITY KG/CU METER	PRESSURE LB/SQ FT	PRESSURE DYNES/SQ CM	TEMPERATURE FAHRENHEIT	TEMPERATURE CENTIGRADE
97.50	.000	3180.	462.	318263.	97007.							
200.36	.000	-1.	430.	481410.	146734.							
309.90	.026	-3389.	466.	296363.	90332.	1.752	.00000340	.00000175				
310.99	.032	-3423.	466.	292651.	89200.	1.692	.00000426	.00000219	.00251	1.202	-116.	-83.
312.07	.046	-3457.	467.	288937.	88068.	1.588	.00000639	.00000329	.00312	1.494	-176.	-116.
313.12	.059	-3490.	467.	285290.	86957.	1.516	.00000843	.00000435	.00396	1.898	-186.	-122.
314.20	.064	-3523.	468.	281504.	85802.	1.490	.00000913	.00000471	.00501	2.397	-141.	-96.
315.30	.066	-3558.	469.	277610.	84616.	1.478	.00000931	.00000480	.00614	2.941	-76.	-60.
316.36	.075	-3591.	470.	273821.	83461.	1.438	.00001068	.00000550	.00733	3.509	-60.	-52.
318.49	.118	-3658.	471.	266103.	81108.	1.236	.00001886	.00000972	.01082	5.177	-126.	-88.
319.57	.137	-3691.	472.	262135.	79899.	1.221	.00002177	.00001122	.01334	6.387	-103.	-75.
320.65	.152	-3725.	472.	258130.	78678.	1.210	.00002394	.00001234	.01622	7.764	-65.	-54.
321.73	.169	-3759.	473.	254090.	77447.	1.199	.00002639	.00001360	.01941	9.293	-32.	-36.
322.81	.196	-3793.	474.	250012.	76204.	1.184	.00003045	.00001569	.02305	11.035	-19.	-29.
323.88	.240	-3826.	474.	245937.	74962.	1.167	.00003716	.00001915	.02737	13.104	-31.	-35.
324.96	.314	-3860.	475.	241788.	73697.	1.145	.00004872	.00002511	.03294	15.773	-66.	-55.
326.03	.398	-3893.	476.	237640.	72433.	1.126	.00006176	.00003183	.04012	19.211	-82.	-63.
327.12	.463	-3927.	476.	233379.	71134.	1.114	.00007133	.00003677	.04904	23.481	-60.	-51.
328.20	.534	-3960.	477.	229121.	69836.	1.104	.00008167	.00004209	.05930	28.391	-37.	-39.
330.37	.787	-4027.	478.	220455.	67195.	1.073	.00011980	.00006174	.08649	41.411	-40.	-40.
331.46	.939	-4061.	479.	216048.	65852.	1.059	.00014243	.00007341	.10468	50.120	-32.	-36.
332.54	1.182	-4094.	480.	211645.	64510.	1.041	.00017968	.00009260	.12697	60.792	-48.	-45.
333.64	1.343	-4127.	480.	207125.	63132.	1.031	.00020267	.00010446	.15423	73.846	-17.	-27.
335.80	1.888	-4192.	481.	198142.	60394.	1.005	.00028358	.00014616	.22260	106.581	-3.	-20.
336.90	2.344	-4224.	482.	193514.	58983.	.987	.00035294	.00018190	.26900	128.795	-16.	-27.
341.25	4.858	-4346.	483.	174877.	53302.	.958	.00071275	.00036735	.57089	273.343	7.	-14.
342.34	5.968	-4375.	484.	170125.	51854.	.953	.00086827	.00044751	.68957	330.165	3.	-17.
343.42	7.250	-4402.	484.	165386.	50410.	.949	.00104657	.00053940	.83302	398.852	4.	-16.
344.51	8.919	-4427.	484.	160575.	48943.	.945	.00127870	.00065904	1.00988	483.532	.	-18.
345.61	10.487	-4452.	483.	155692.	47455.	.941	.00149288	.00076943	1.22422	586.154	18.	-8.
346.69	13.206	-4473.	483.	150873.	45986.	.936	.00187301	.00096535	1.48063	708.923	1.	-18.
347.78	16.400	-4492.	482.	145987.	44497.	.931	.00232024	.00119585	1.80481	864.141	-7.	-22.
348.88	19.730	-4507.	481.	141038.	42988.	.926	.00278682	.00143633	2.20531	1055.900	1.	-18.
349.97	24.570	-4518.	479.	136121.	41490.	.921	.00347456	.00179079	2.69287	1289.347	-9.	-23.
351.06	30.020	-4523.	477.	131194.	39988.	.916	.00425899	.00219508	3.29683	1578.522	-9.	-23.
353.24	50.820	-4504.	469.	121356.	36989.	.906	.00734812	.00378722	5.07030	2427.657	-58.	-50.
354.33	62.780	-4477.	464.	116462.	35498.	.906	.00918782	.00473540	6.35409	3042.337	-57.	-50.
355.42	86.340	-4431.	456.	111607.	34018.	.906	.01290200	.00664969	8.04695	3852.878	-97.	-72.
356.52	105.180	-4362.	446.	106771.	32544.	.907	.01621368	.00835653	10.28180	4922.926	-91.	-68.
358.70	147.390	-4157.	418.	97487.	29714.	.911	.02489270	.01282970	16.27758	7793.706	-79.	-62.
360.89	239.420	-3806.	375.	88769.	27057.	.921	.04774271	.02460659	26.04473	12470.215	-142.	-97.
361.98	254.310	-3573.	349.	84749.	25831.	.929	.05709884	.02942874	32.76157	15686.237	-126.	-88.
363.07	283.120	-3316.	320.	80995.	24687.	.937	.07313570	.03769414	40.53550	19408.397	-137.	-94.
364.17	287.490	-3039.	288.	77500.	23622.	.947	.08752751	.04511168	49.48919	23695.422	-131.	-91.
365.26	290.250	-2760.	257.	74341.	22659.	.957	.10602113	.05464329	59.24082	28364.503	-135.	-93.
367.46	283.660	-2202.	177.	68884.	20996.	1.010	.15468560	.07972496	81.73548	39134.948	-152.	-103.
368.55	273.170	-1934.	150.	66630.	20309.	1.010	.19314307	.09954594	94.23282	45118.675	-176.	-116.
369.64	194.260	-1715.	78.	64642.	19703.	1.010	.17539070	.09039636	105.95535	50731.423	-108.	-78.
370.74	186.550	-1541.	67.	62852.	19157.	1.010	.20866850	.10754774	116.93829	55990.053	-134.	-92.
374.02	137.420	-1115.	45.	58498.	17830.	.940	.31548520	.16260107	152.9844	73248.917	-178.	-117.
376.21	114.400	-910.	32.	56282.	17155.	.813	.45665053	.23535768	180.0950	86229.477	-230.	-146.

SM 2.10

ALTITUDE METERS	DENSITY KG/CU METER	PRESSURE DYNES/SQ CM	TEMPERATURE CENTIGRADE
16000.	.44277106	113960.66	-183.5
20000.	.09422814	47702.753	-96.8
24000.	.04225933	22077.168	-91.2
28000.	.01952670	10553.673	-84.9
32544.	.00835653	4922.926	-68.0
36000.	.00447857	2825.298	-53.4
40000.	.00219163	1576.035	-22.7
44000.	.00126302	923.044	-18.6
48000.	.00072700	546.224	-11.5
52000.	.00043743	323.991	-15.2
60000.	.00015535	112.358	-21.2
64000.	.00009515	65.289	-34.2
68000.	.00005494	36.907	-39.1
72000.	.00003285	20.532	-55.4
76000.	.00001644	11.350	-32.7
80000.	.00001092	6.243	-74.1
84000.	.00000520	3.225	-57.2
88000.	.00000323	1.526	-108.4

Note: This is an unedited tabulation of computer calculations. Some points at the highest and lowest altitudes lie outside the valid range of measurement of the sphere instrumentation. See page 24 for a discussion. See the plotted curves for the final edited data of density and temperature vs. altitude.

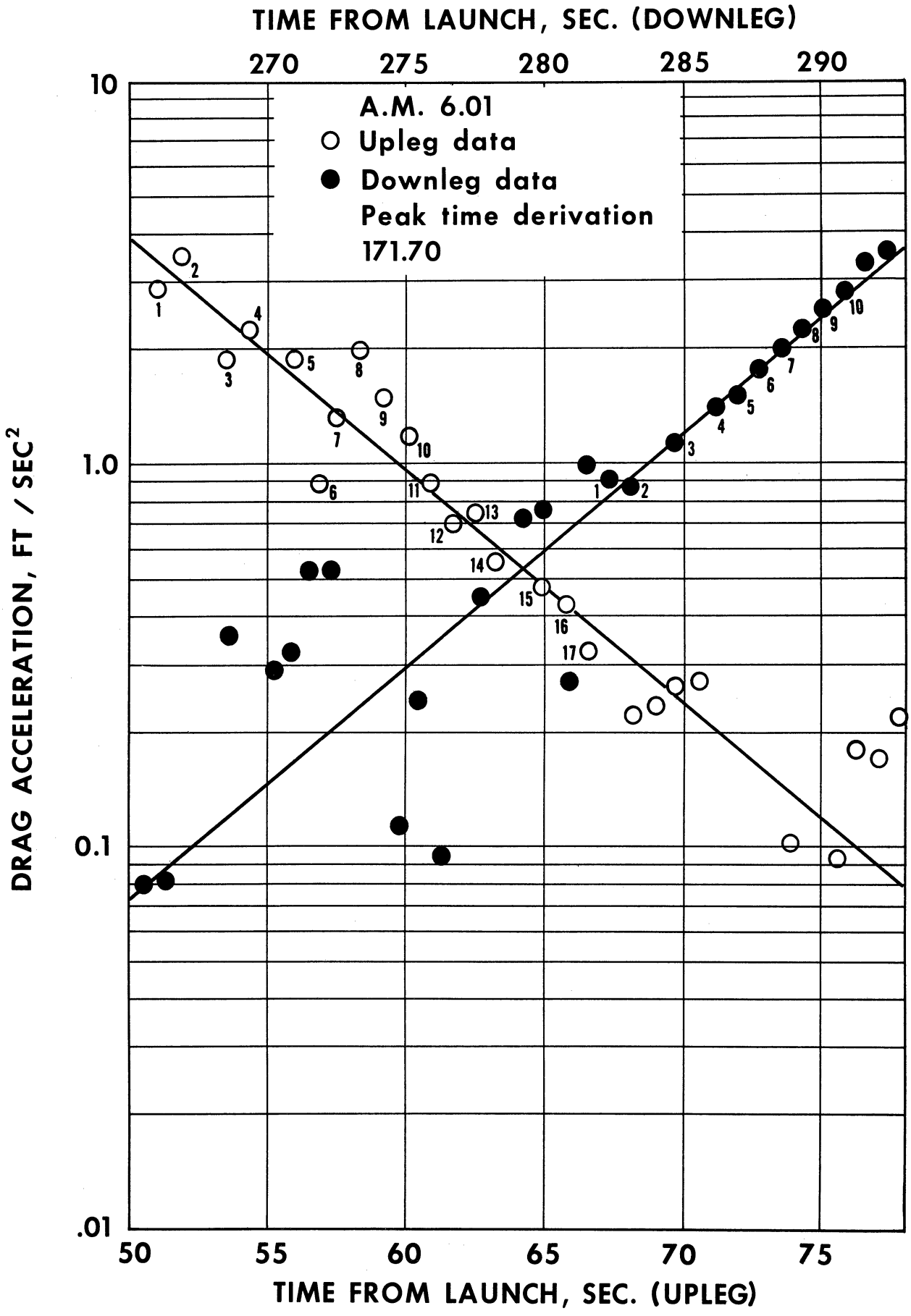

Fig. 34. Drag acceleration vs. time used to obtain peak time (AM 6.01).

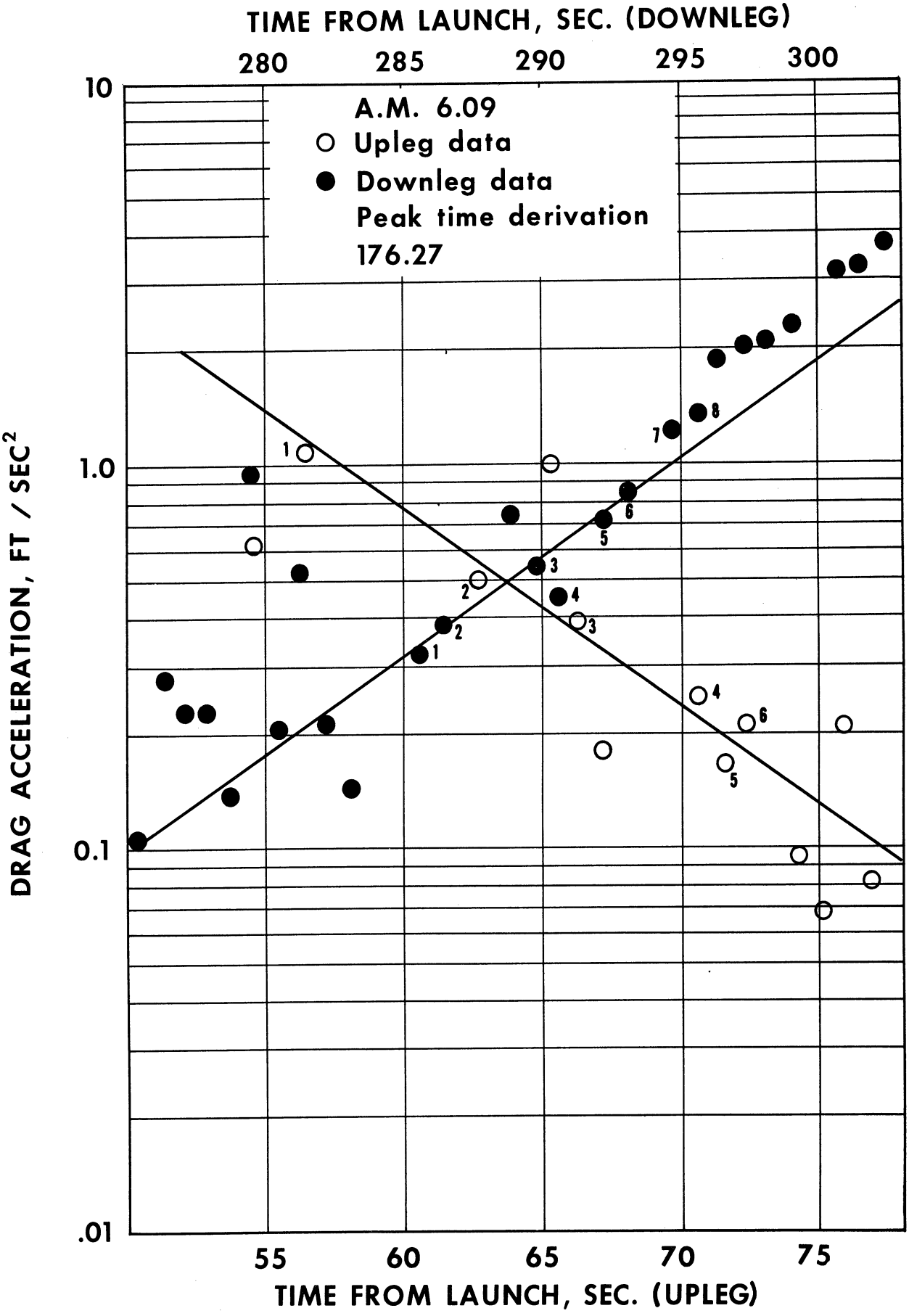

Fig. 35. Drag acceleration vs. time used to obtain peak time (AM 6.09).

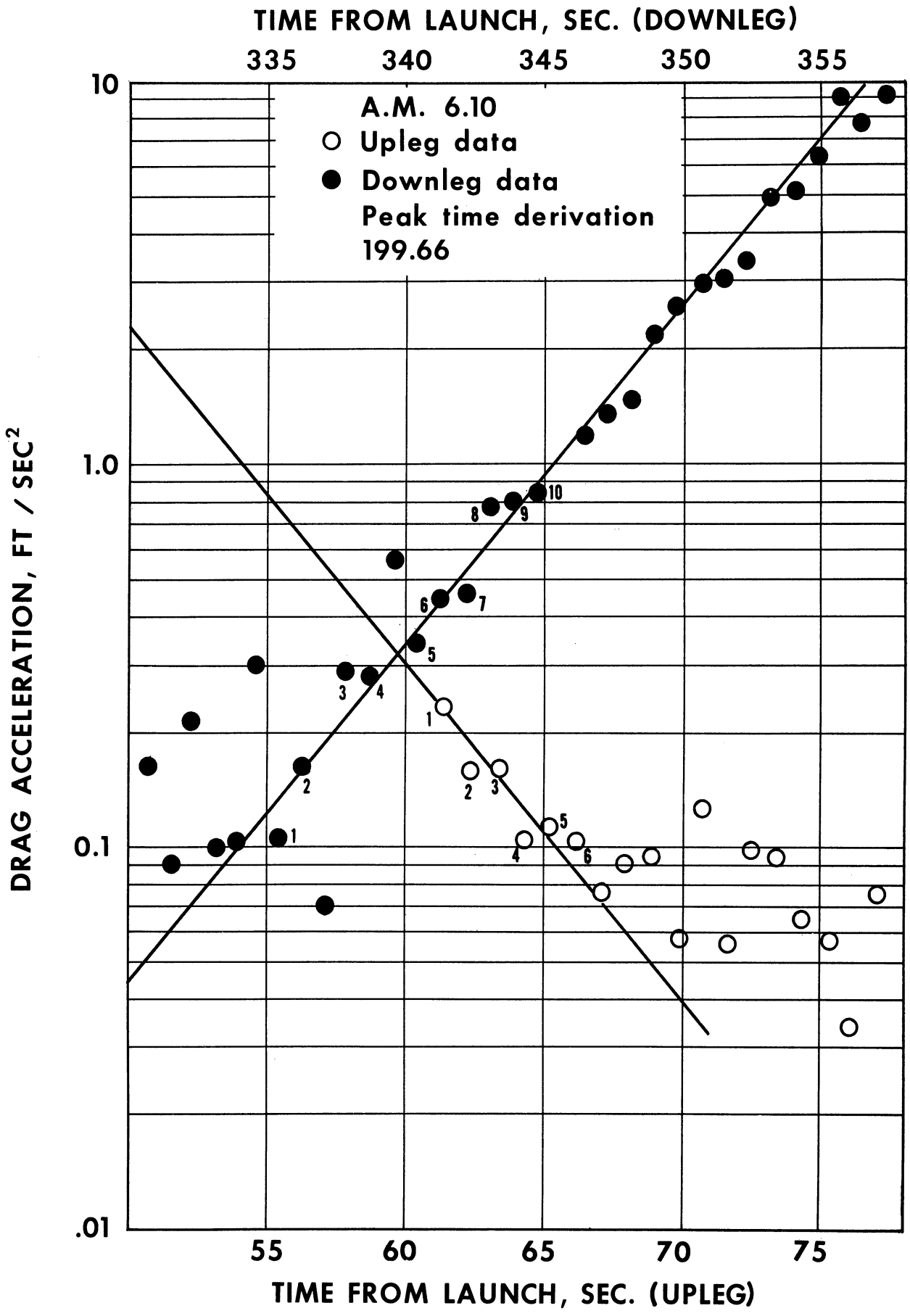

Fig. 36. Drag acceleration vs. time used to obtain peak time (AM 6.10).

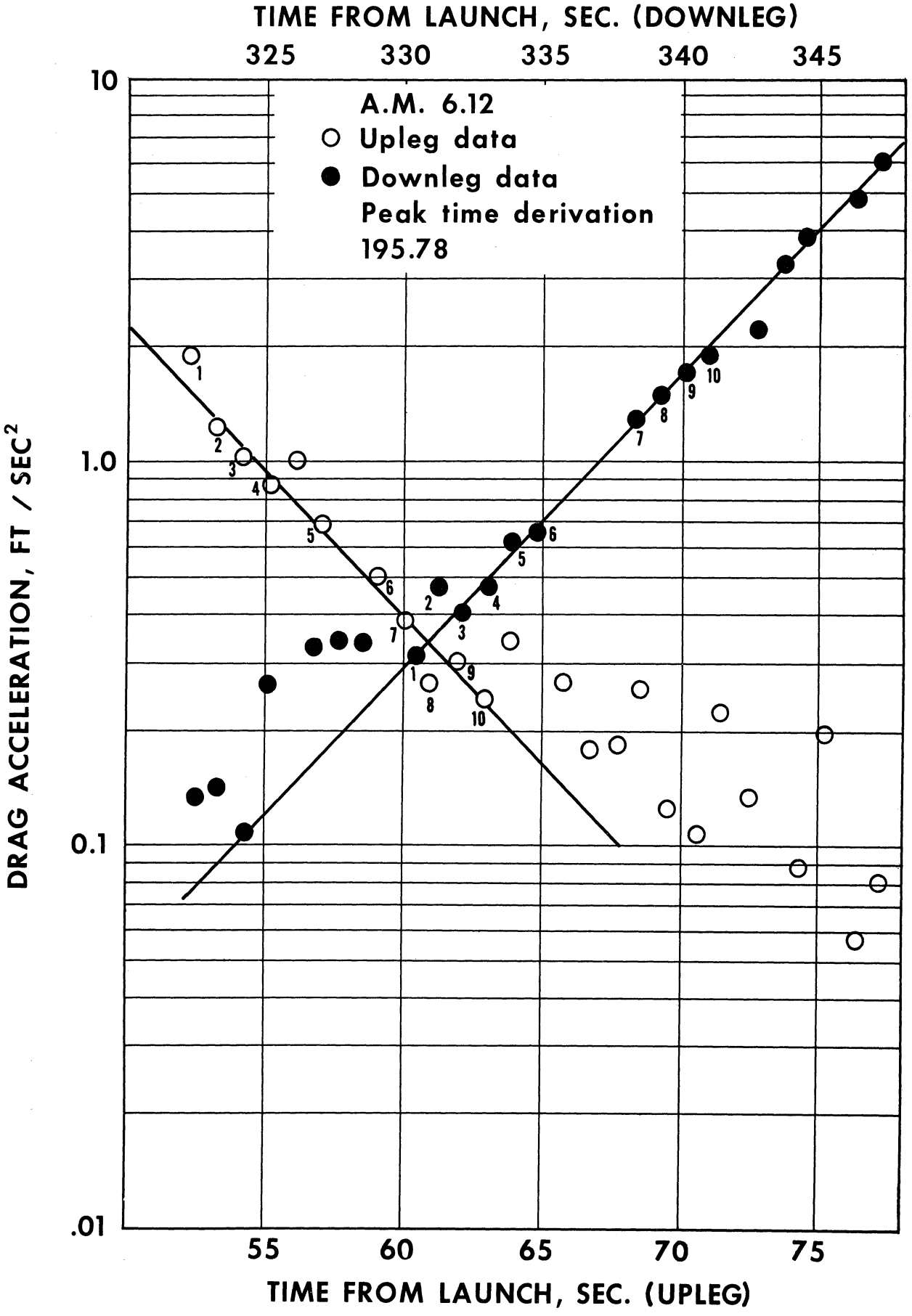

Fig. 37. Drag acceleration vs. time used to obtain peak time (AM 6.12).

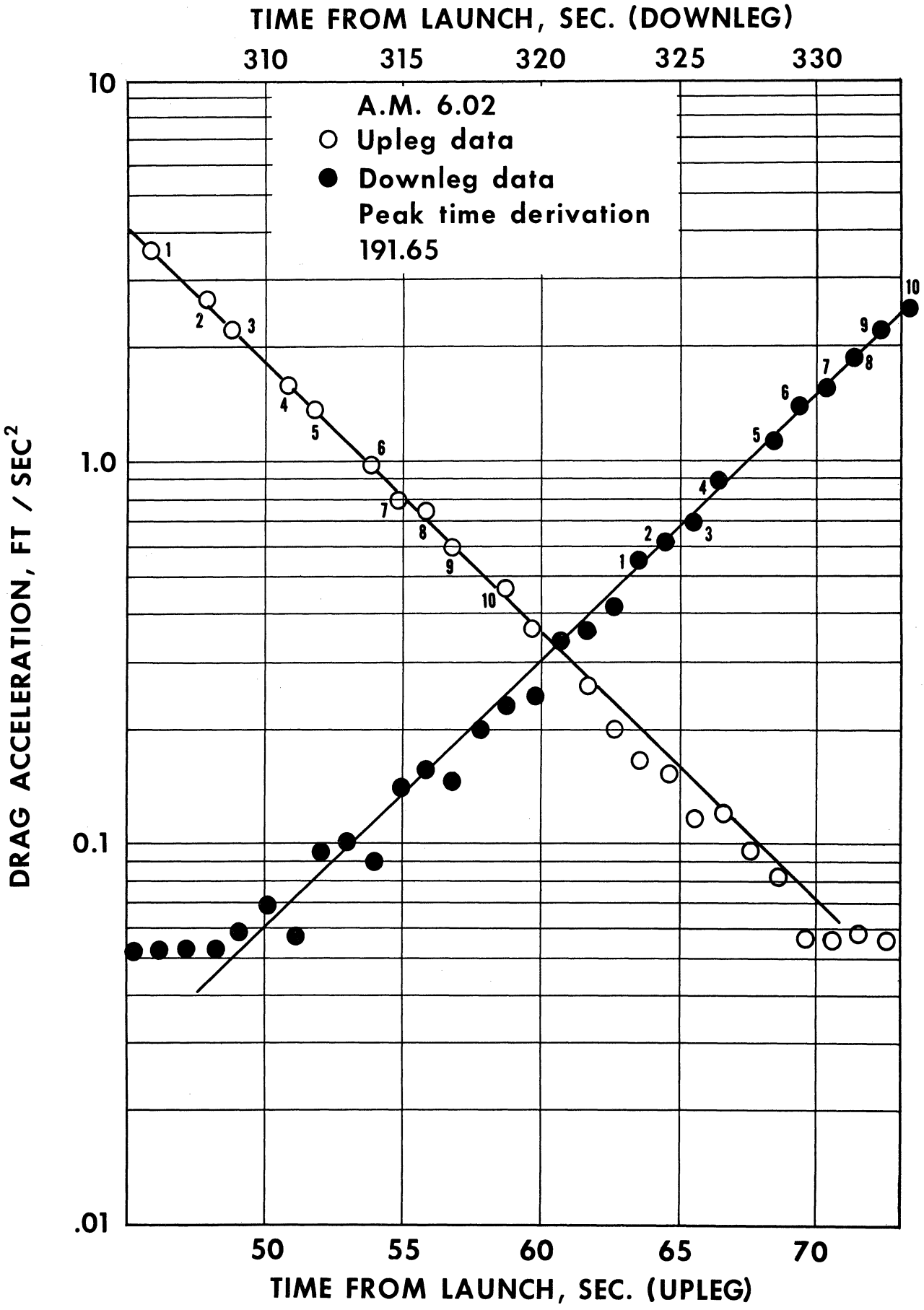

Fig. 38. Drag acceleration vs. time used to obtain peak time (AM 6.02).

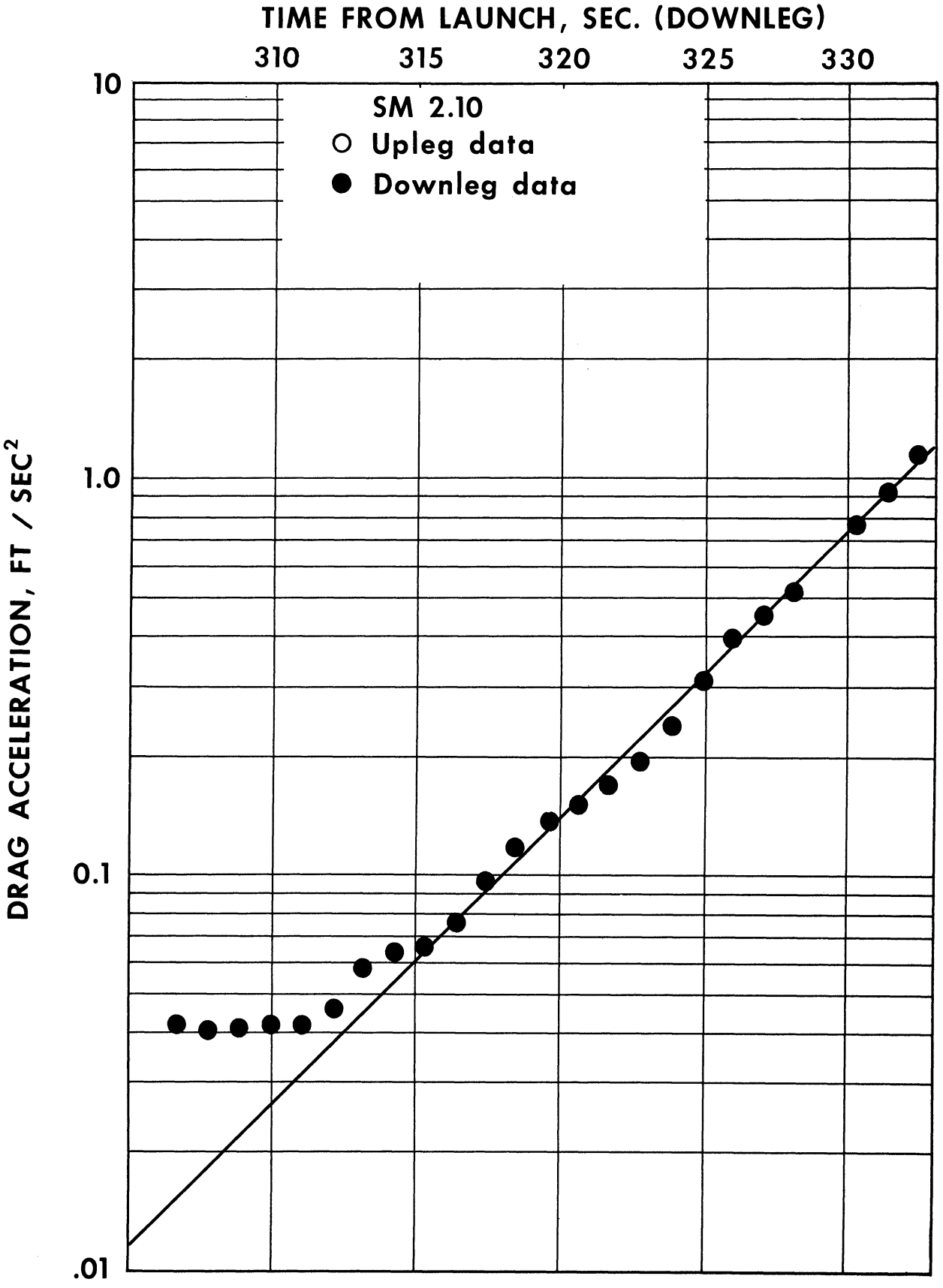

Fig. 39. Drag acceleration vs. time used to obtain peak time (SM 2.10).

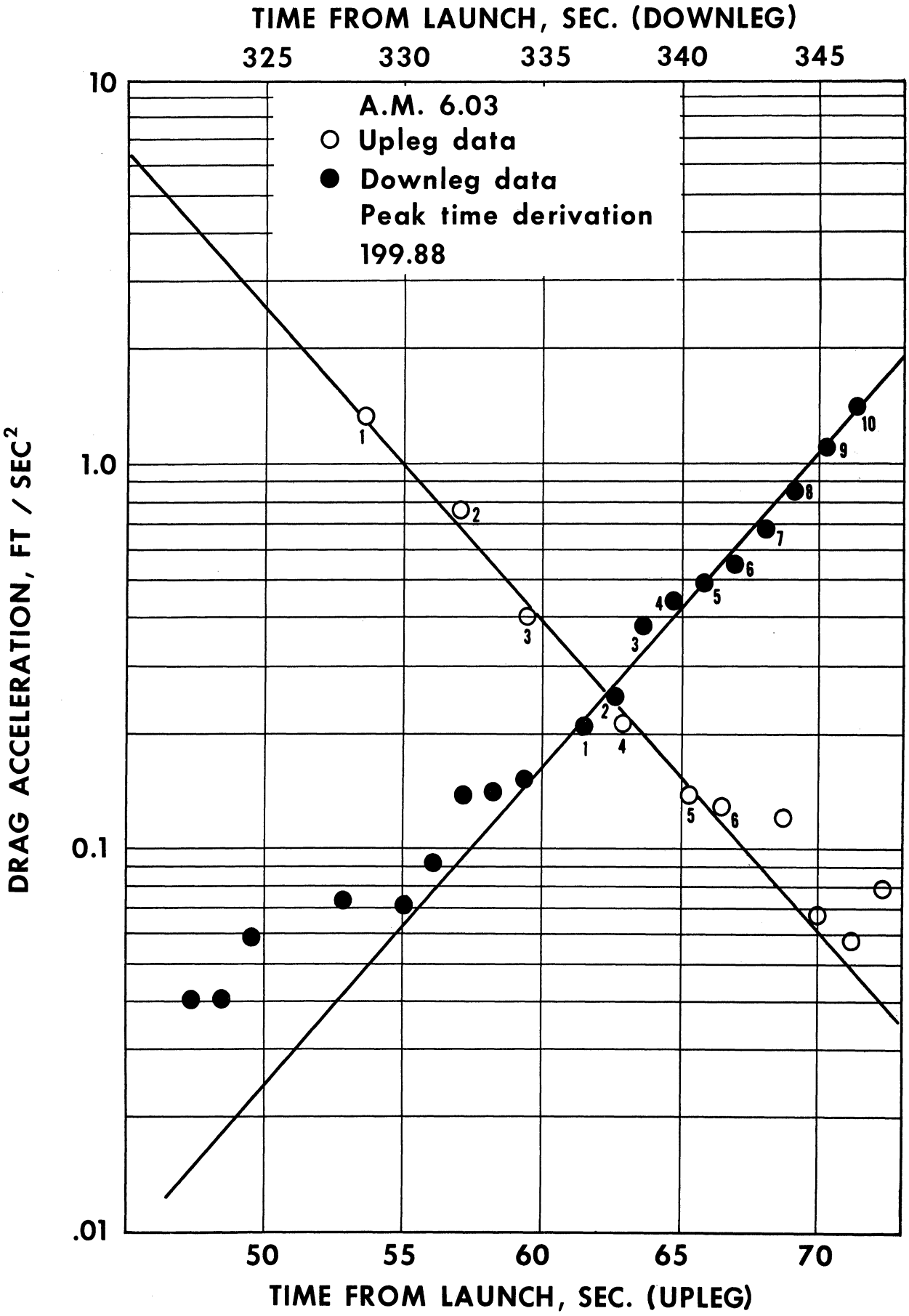

Fig. 40. Drag acceleration vs. time used to obtain peak time (AM 6.03).

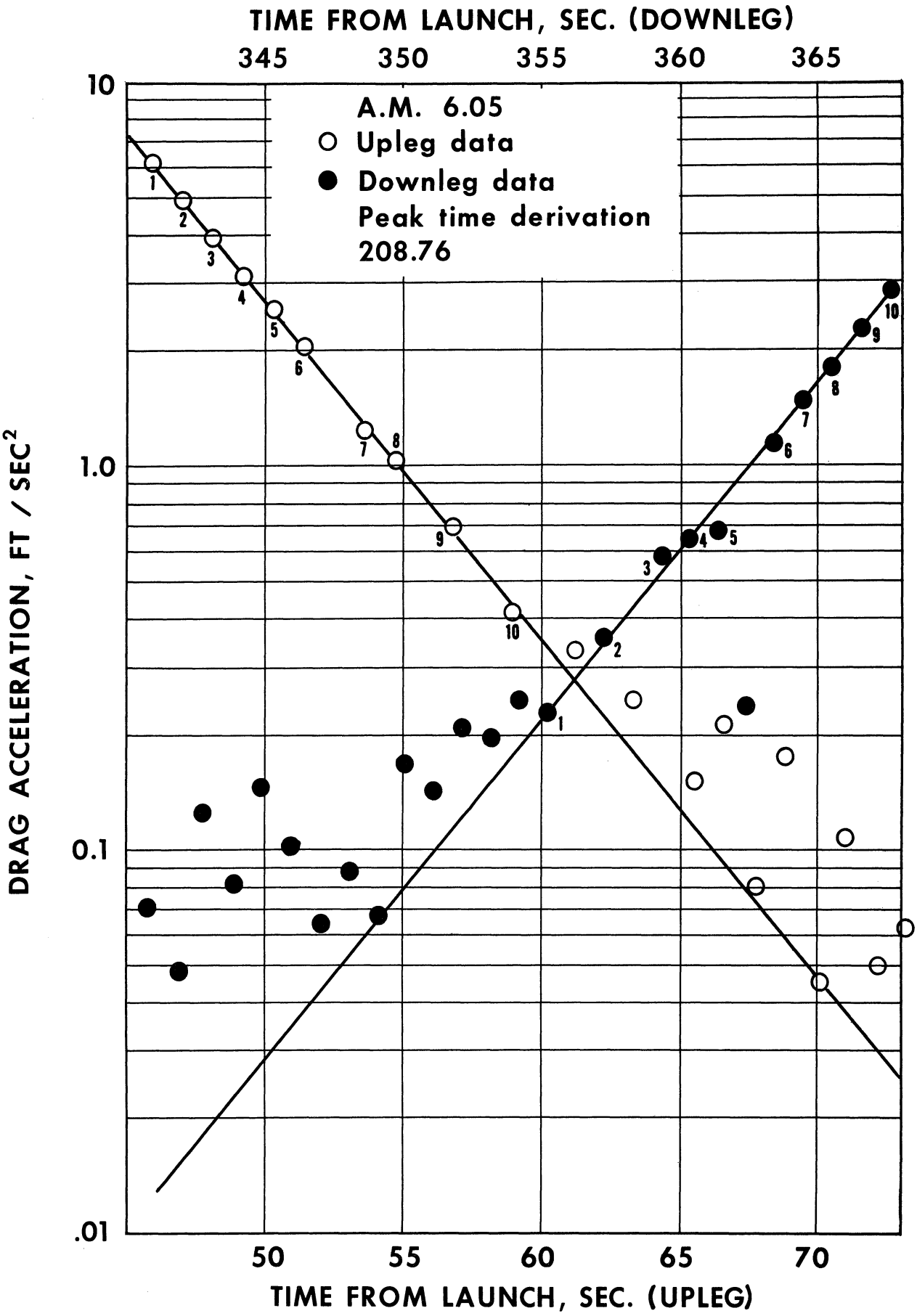

Fig. 41. Drag acceleration vs. time used to obtain peak time (AM 6.05).

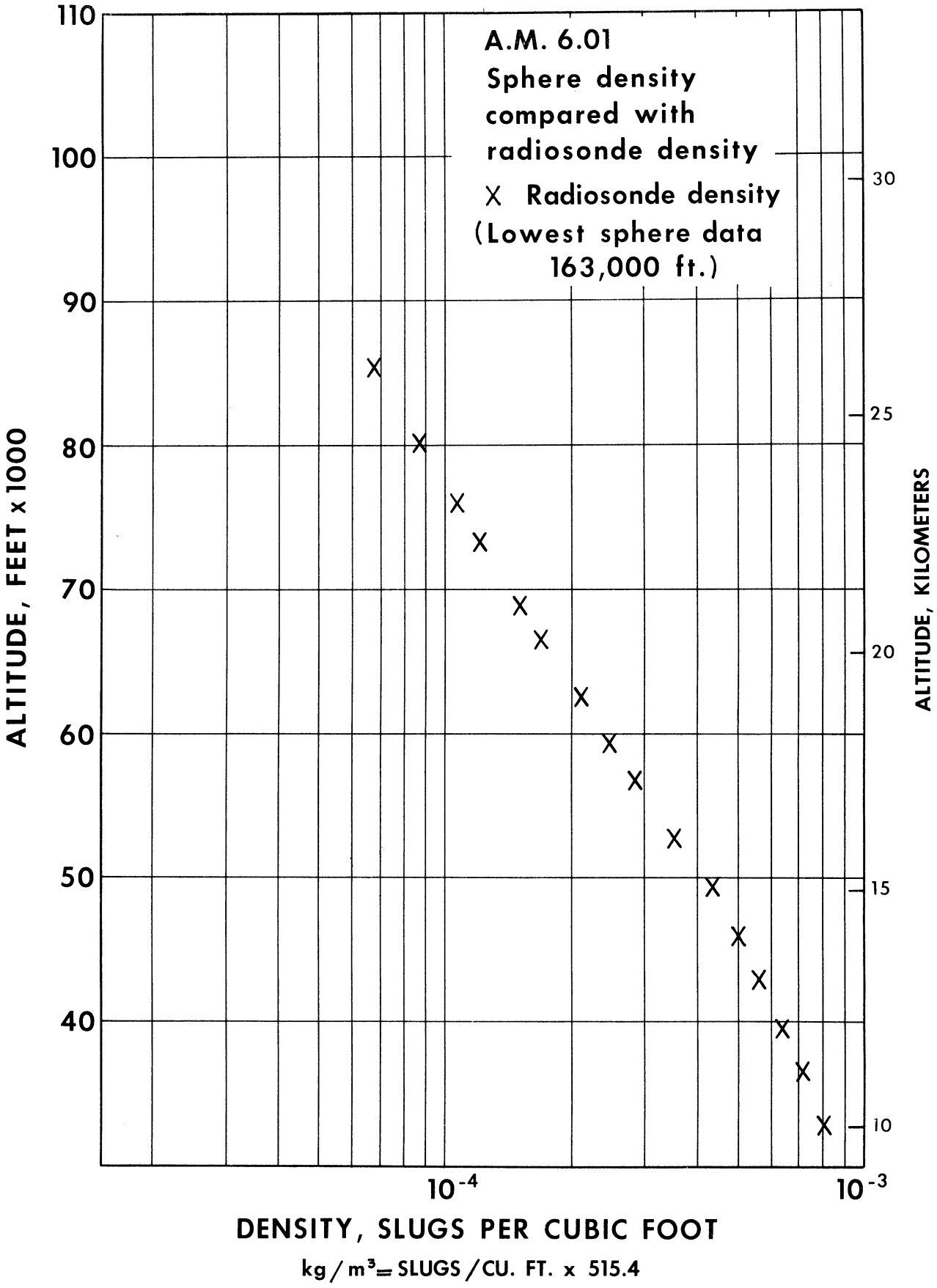

Fig. 42. Sphere and radiosonde densities compared (AM 6.01).

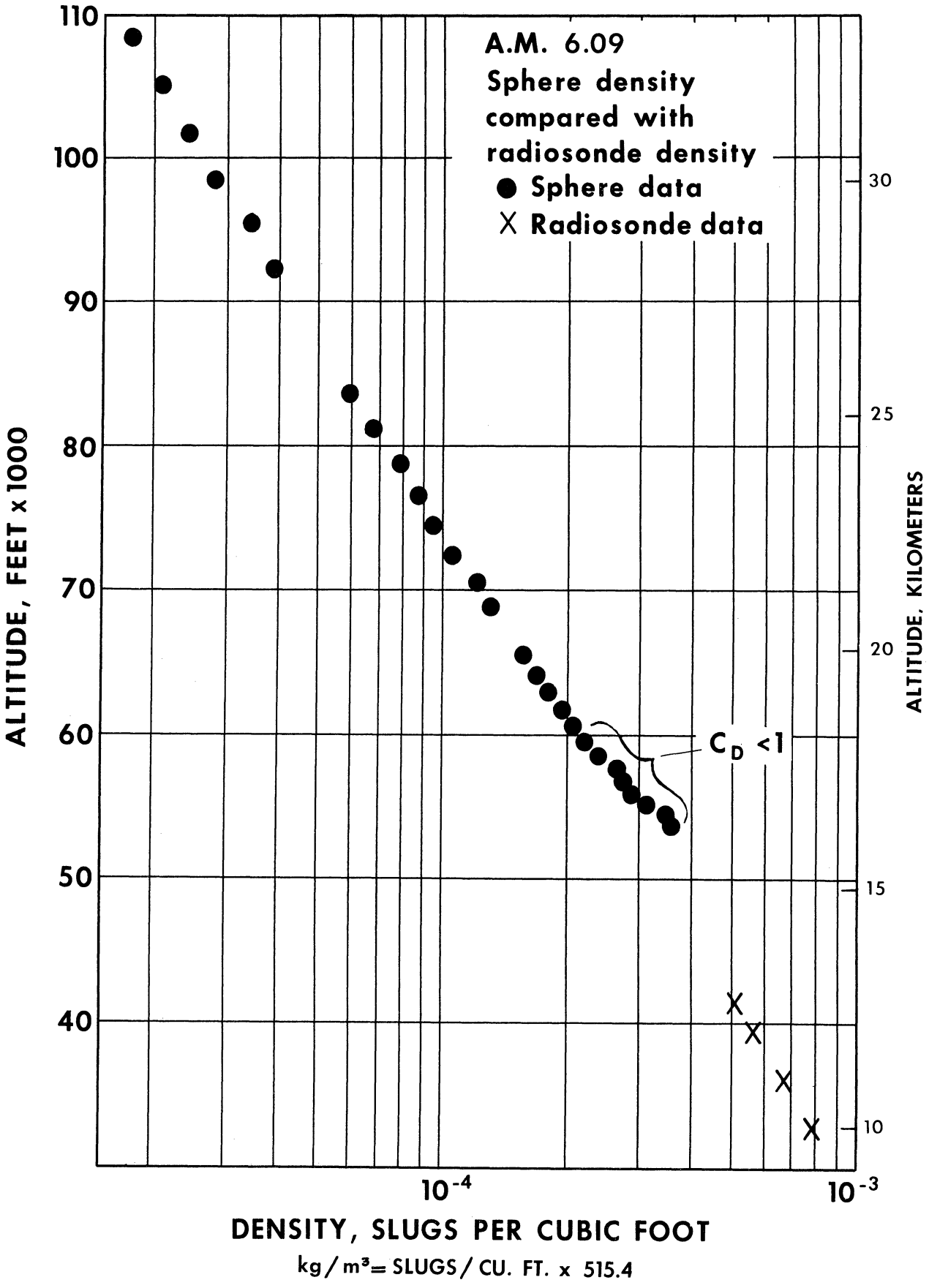

Fig. 43. Sphere and radiosonde densities compared (AM 6.09).

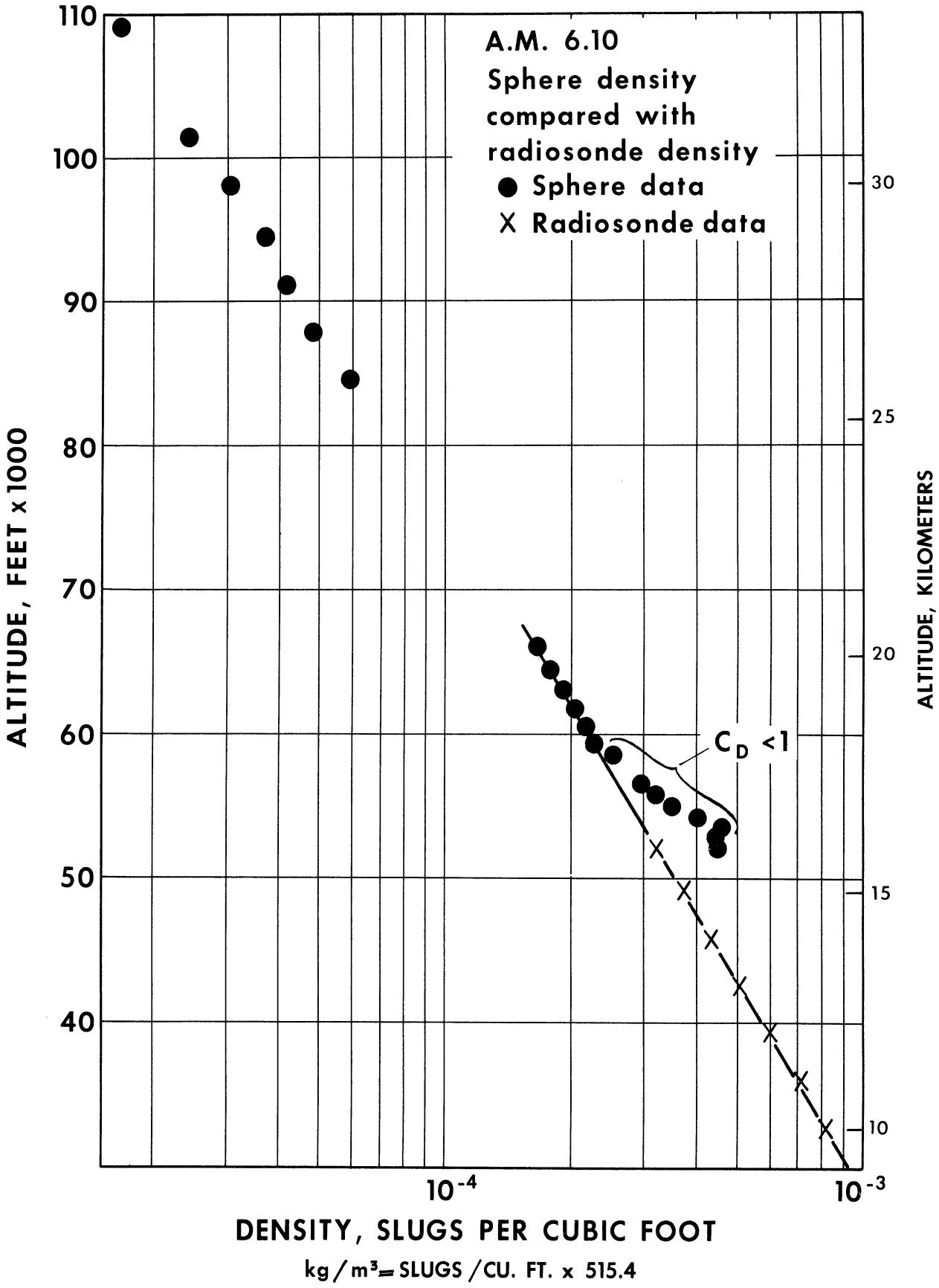

Fig. 44. Sphere and radiosonde densities compared (AM 6.10).

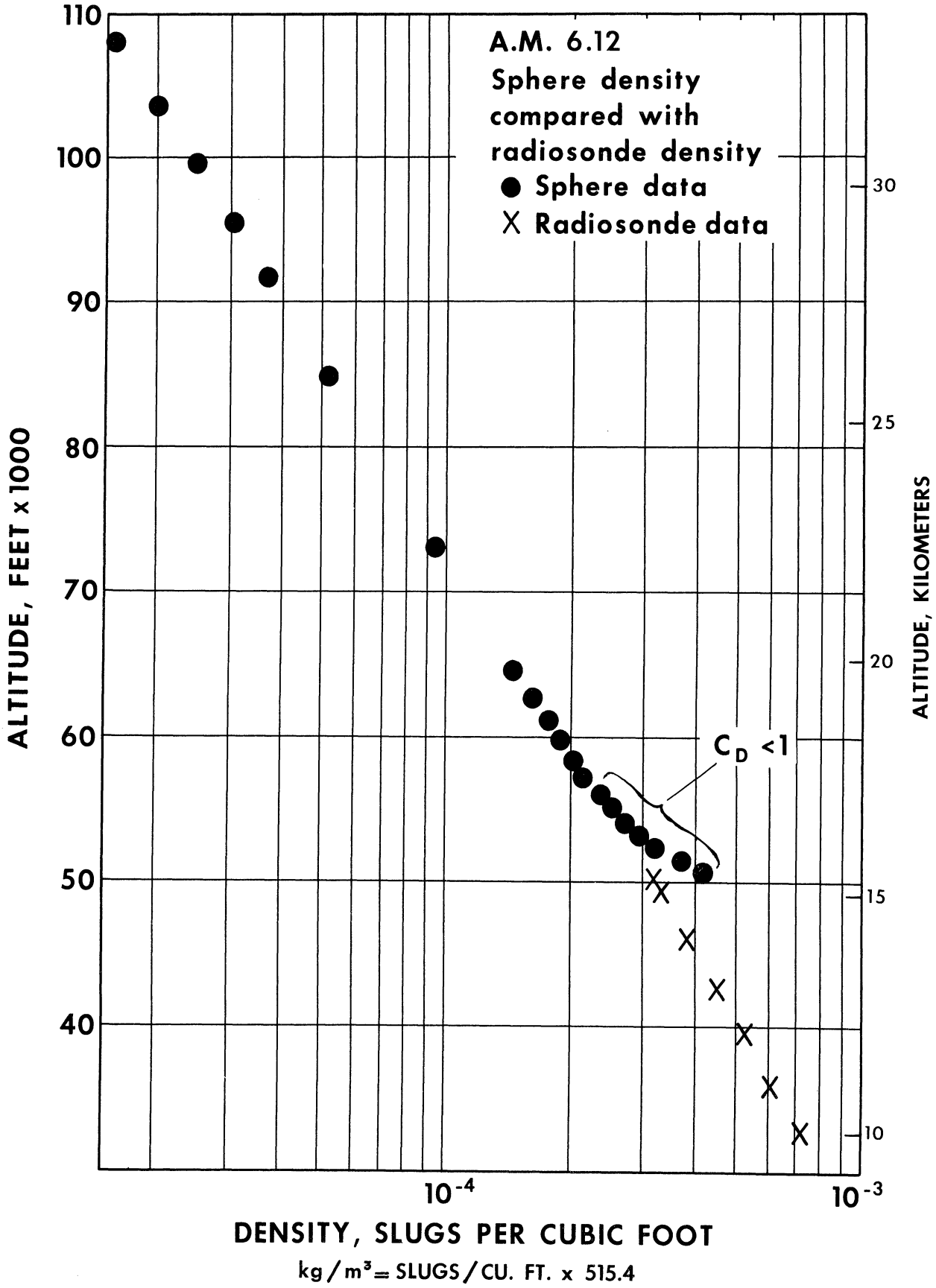

Fig 45. Sphere and radiosonde densities compared (AM 6.12).

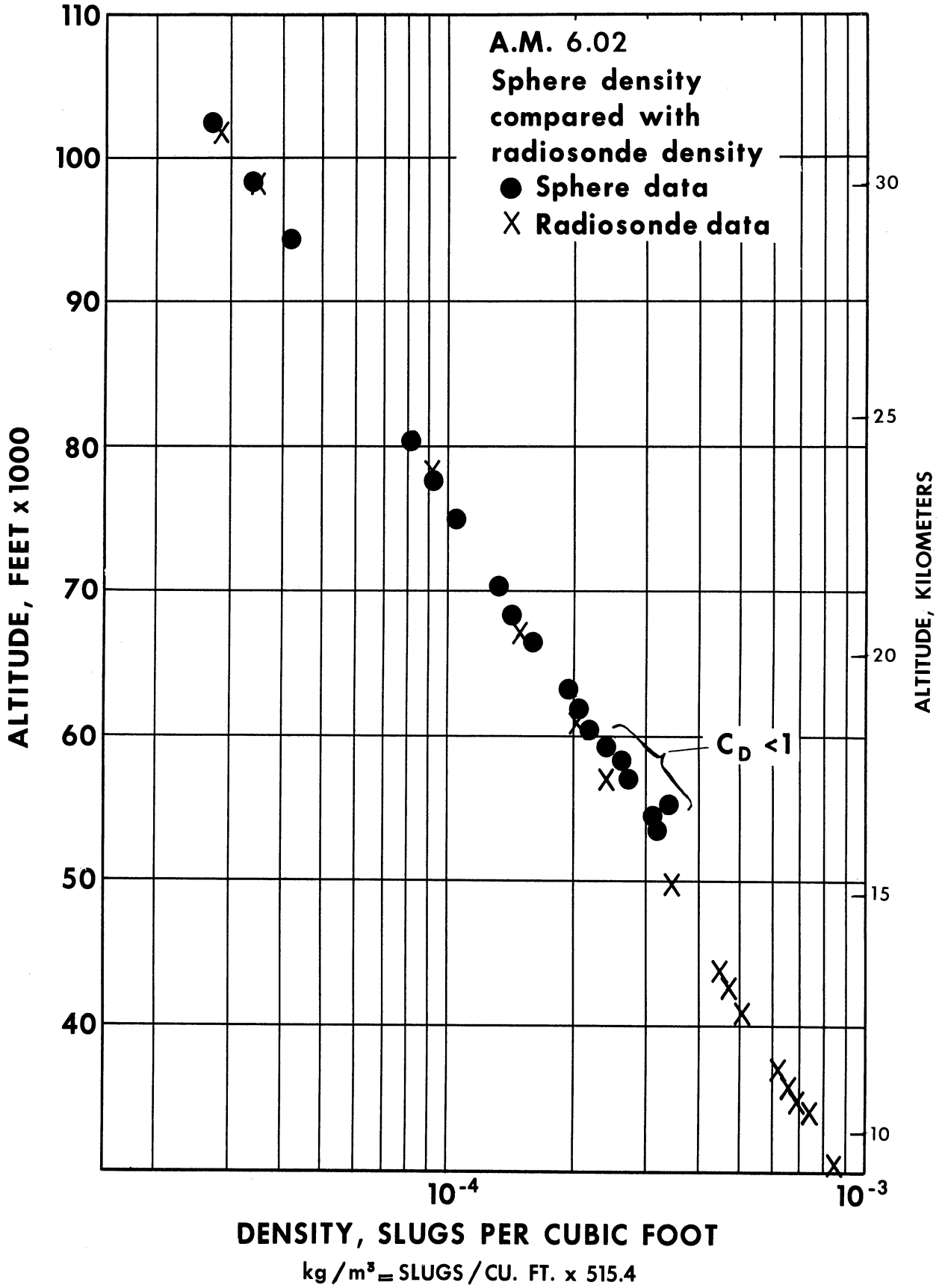

Fig. 46. Sphere and radiosonde densities compared (AM 6.02).

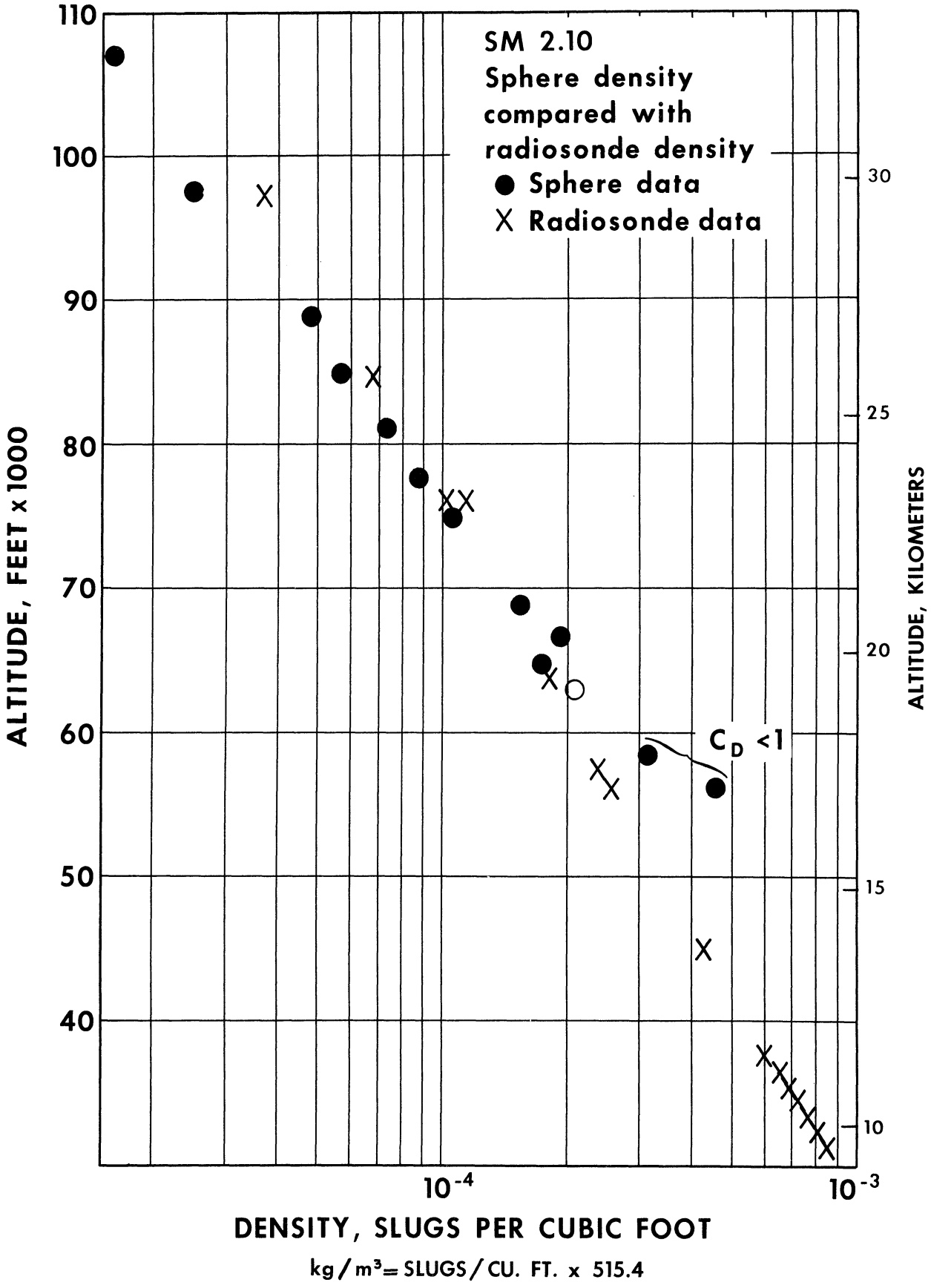

Fig. 47. Sphere and radiosonde densities compared. (SM 2.10).

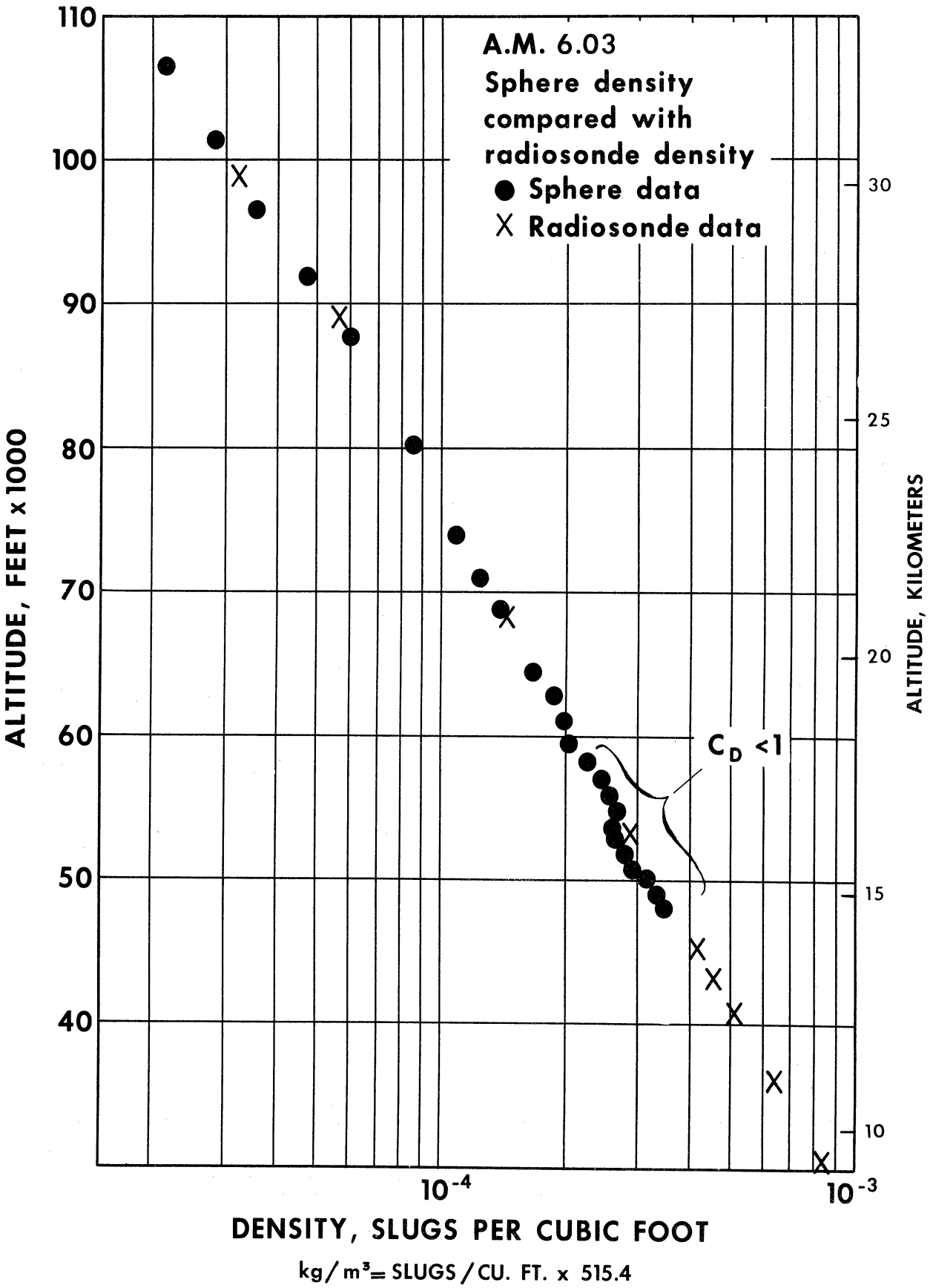

Fig. 48. Sphere and radiosonde densities compared (AM 6.03).

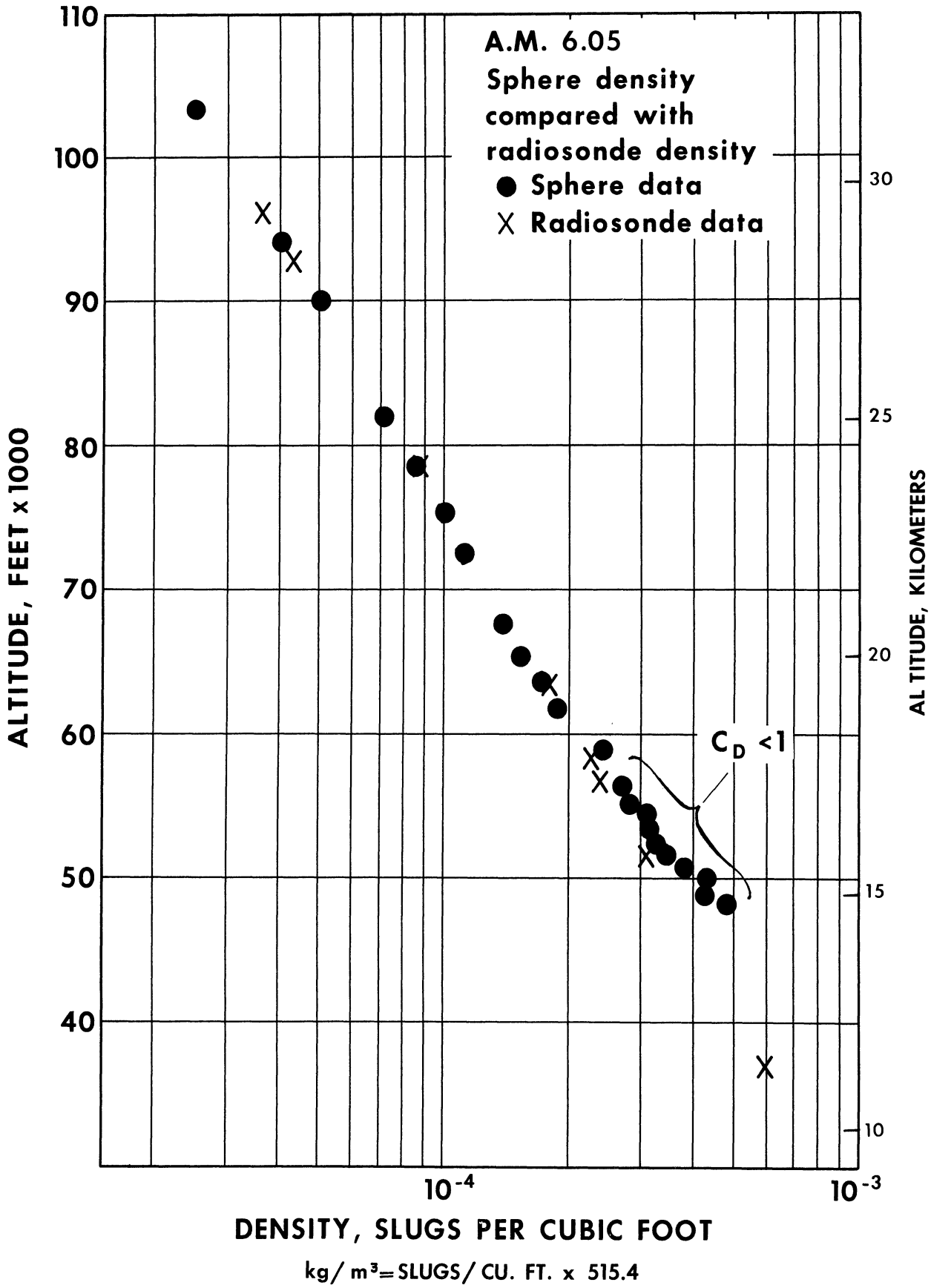

Fig. 49. Sphere and radiosonde densities compared (AM 6.05).

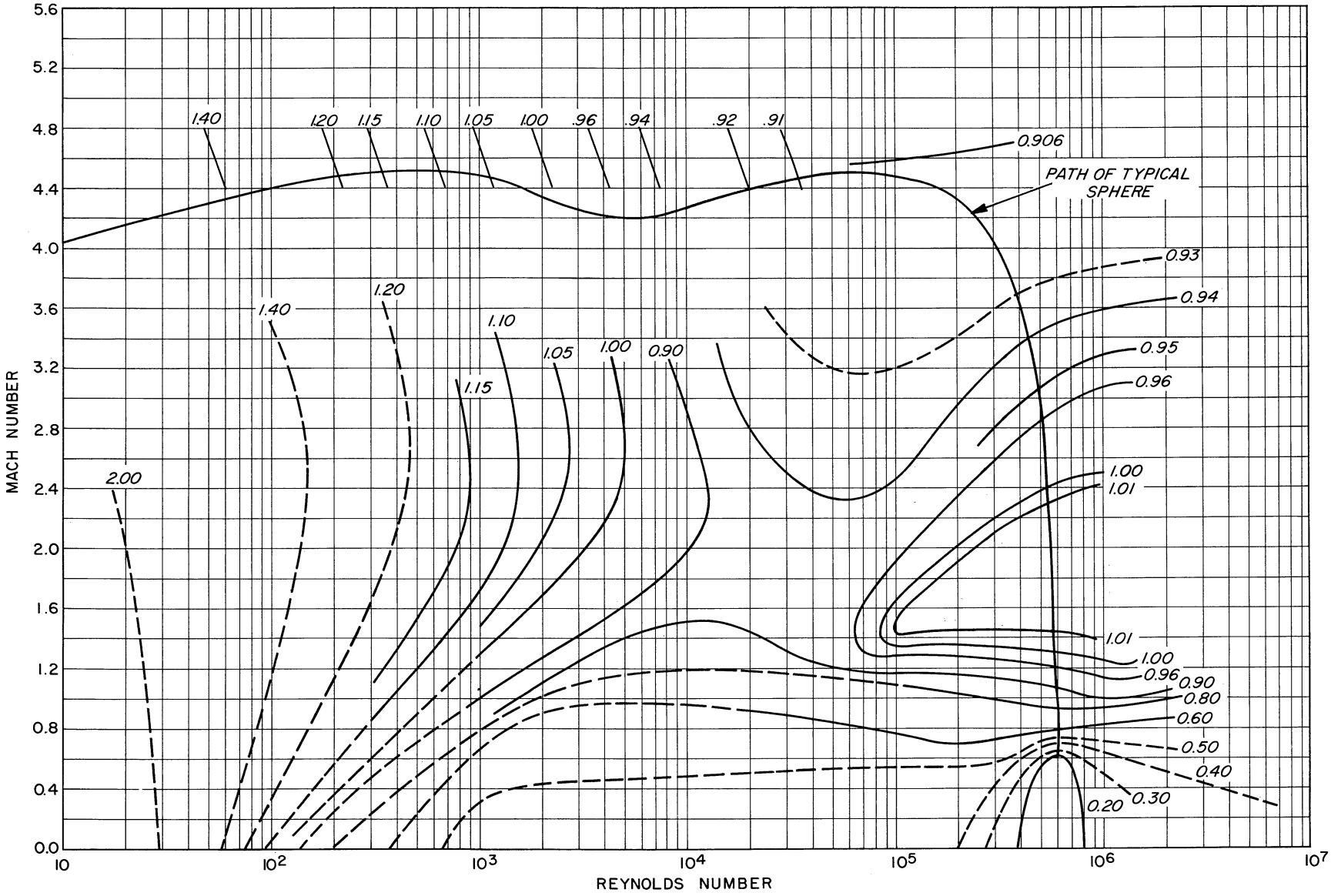

Fig. 50. C_D as a function of Mach number and Reynolds number.

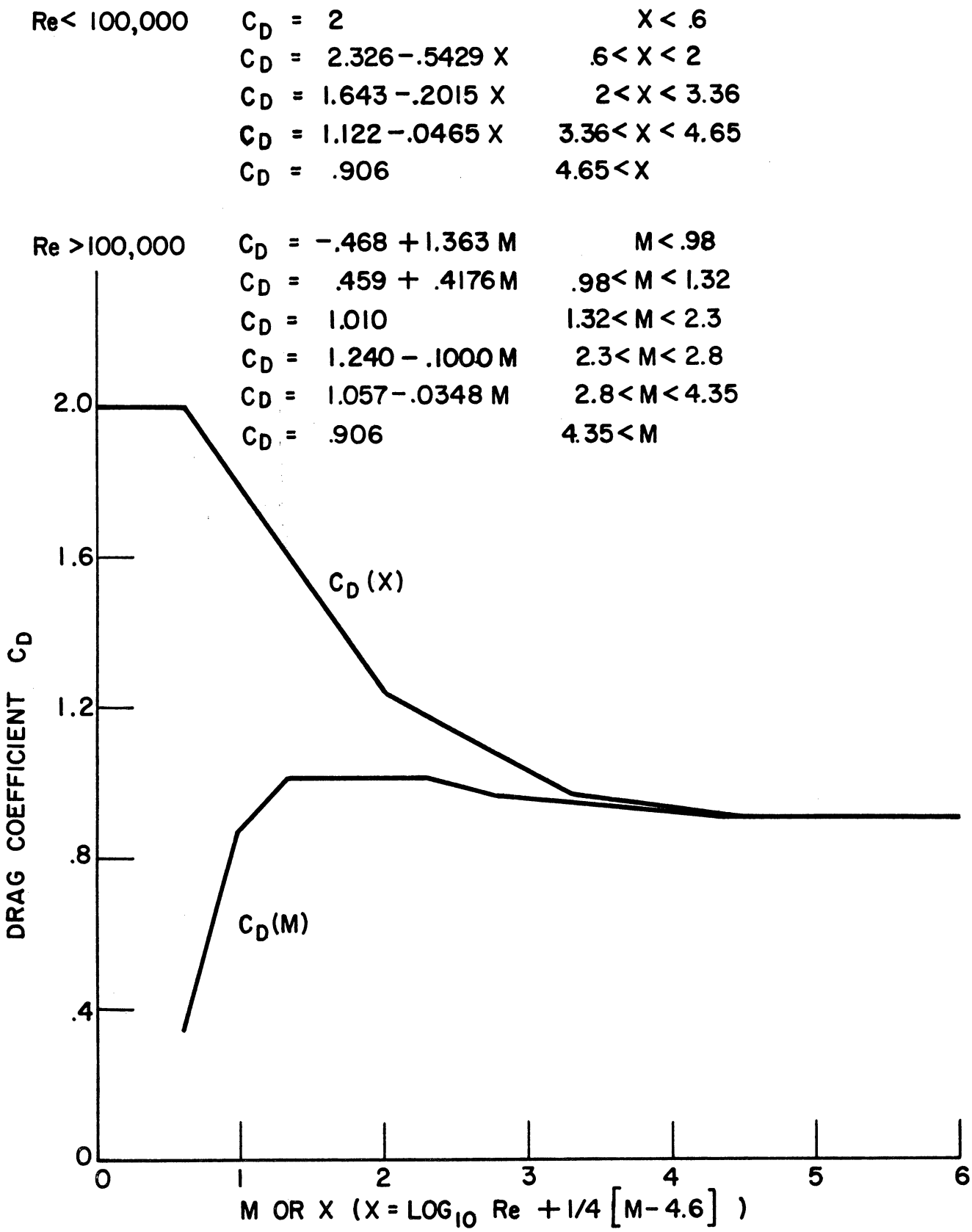

Fig. 51. Empirical drag coefficient functions.

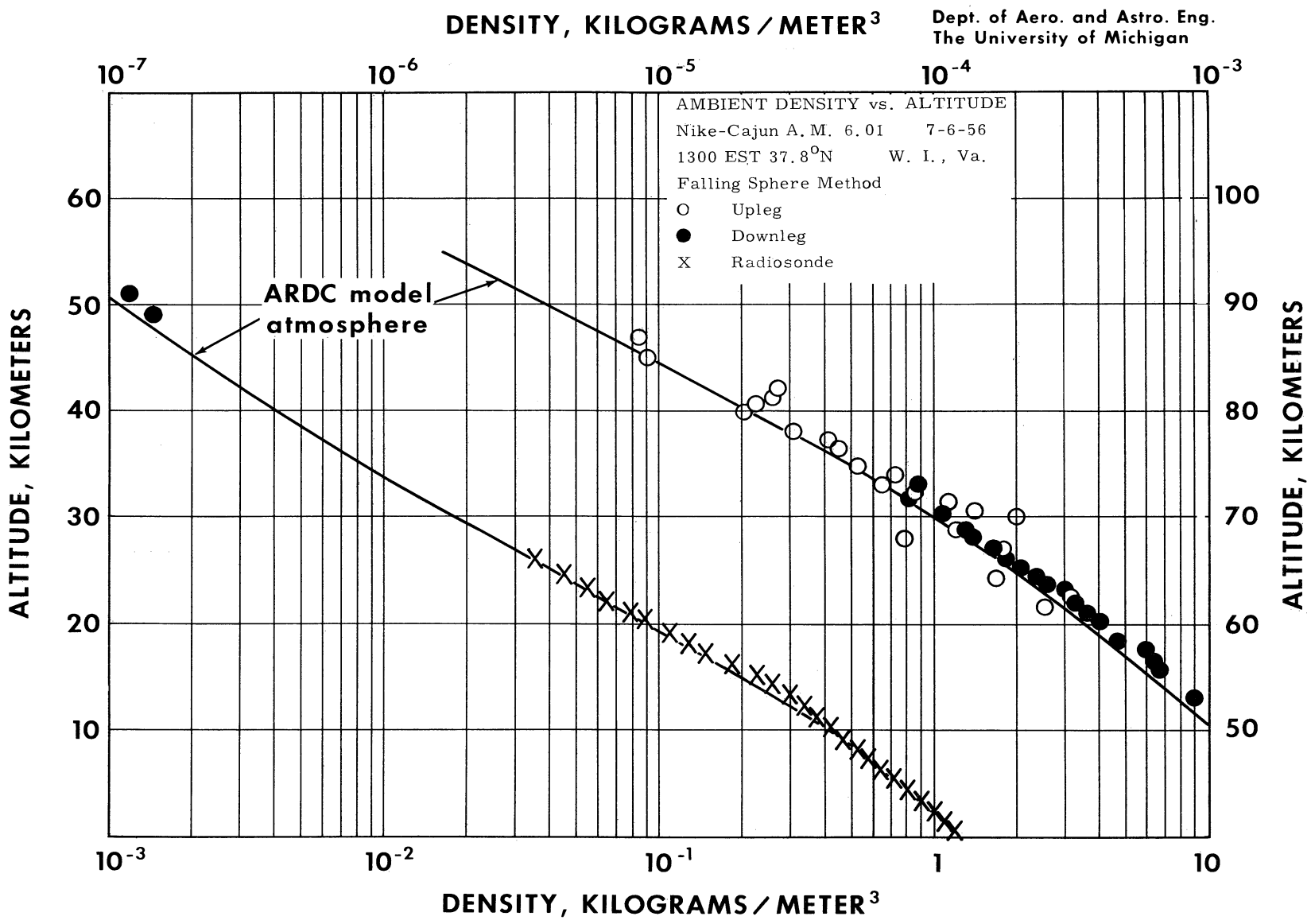

Fig. 52. Ambient density vs. altitude (AM 6.01).

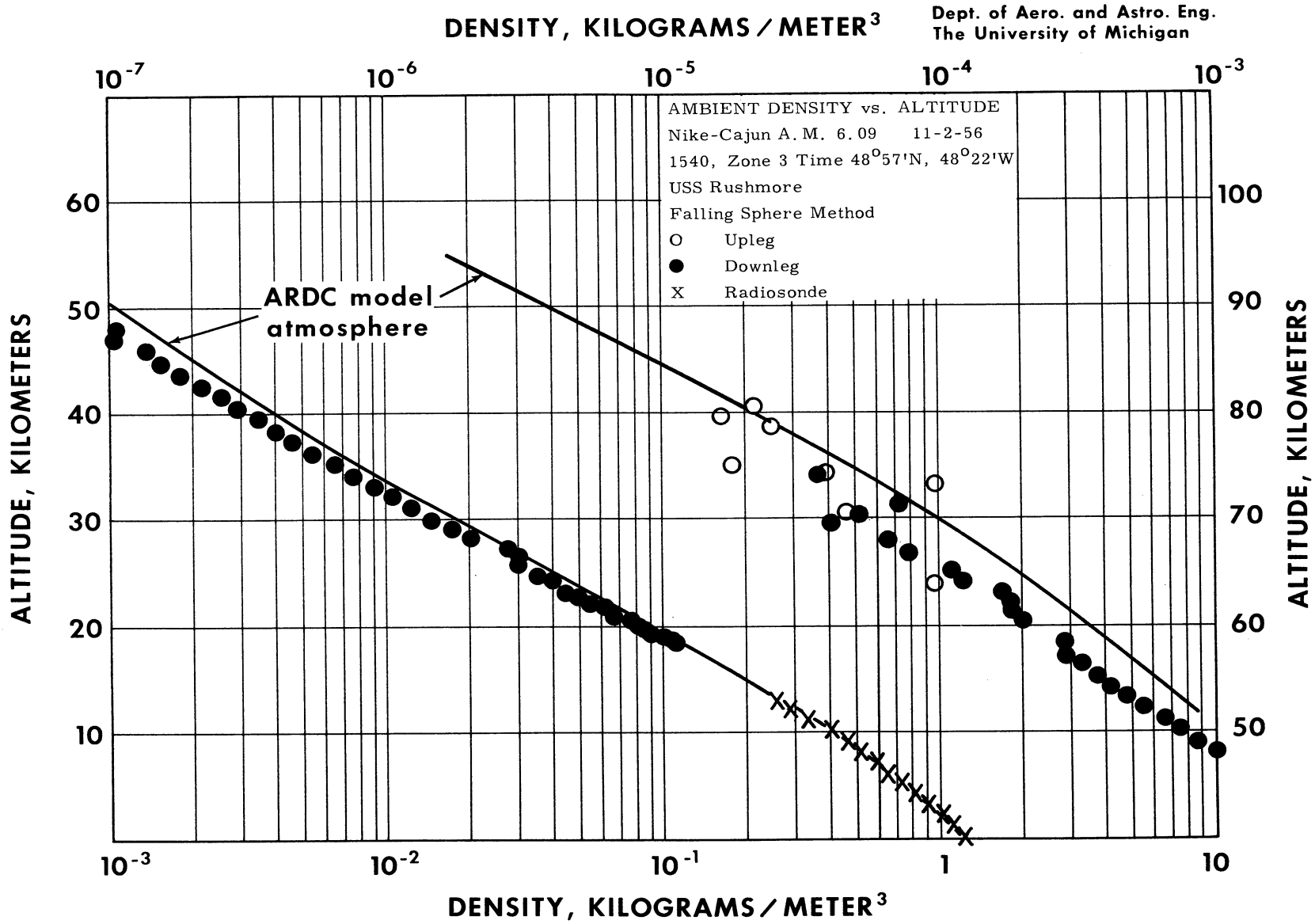

Fig. 53. Ambient density vs. altitude (AM 6.09).

Note pertaining to AM 6.09, AM 6.10, and AM 6.12

As noted in section 7.3 the trajectory calculations for AM 6.09, 6.10, and 6.12 are subject to serious error due to the lack of high-altitude balloon sonde data. After this report was prepared it was found that data from surrounding nearby shore stations and weather ships taken at the time of the firings extended the needed curve to satisfactory altitudes. The first-order effect is that the densities and temperatures for AM 6.09 and 6.10 should be moved upward about 1.0 kilometer and those for AM 6.12 about 0.6 kilometer. Small changes in the values of density and temperature are also to be expected and for complete rigor these should be re-calculated.

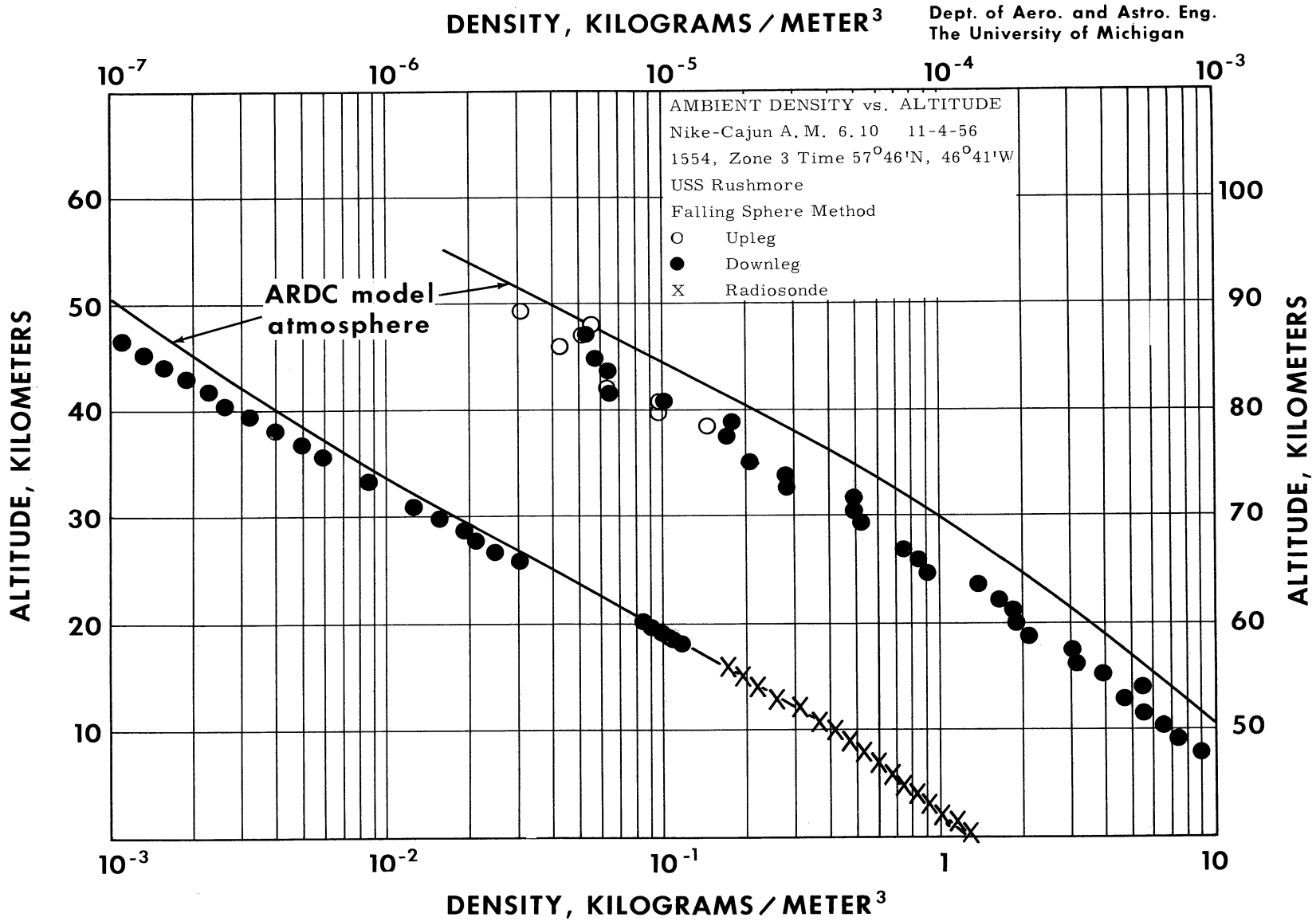

Fig. 54. Ambient density vs. altitude (AM 6.10).

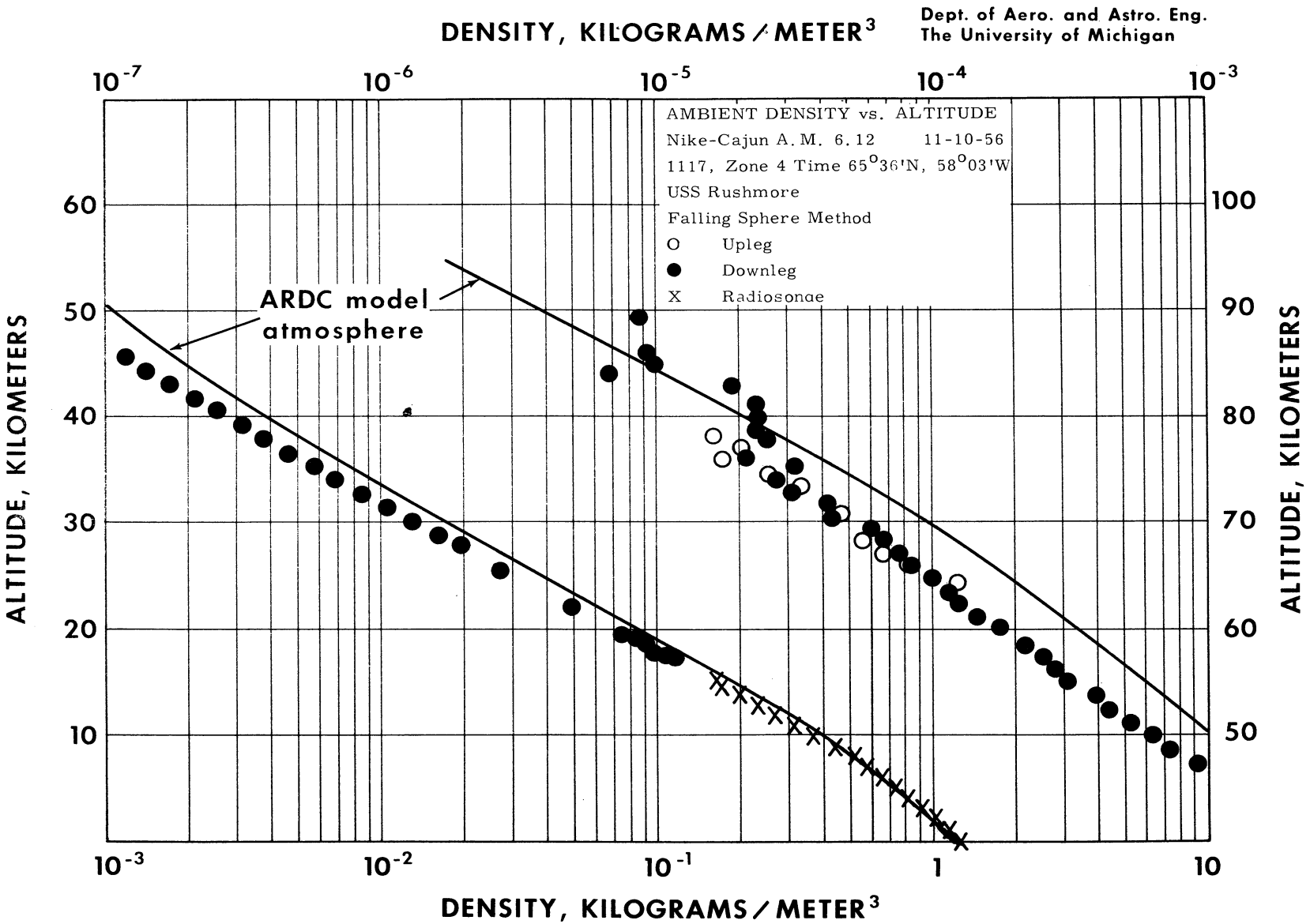

Fig. 55. Ambient density vs. altitude (AM 6.12).

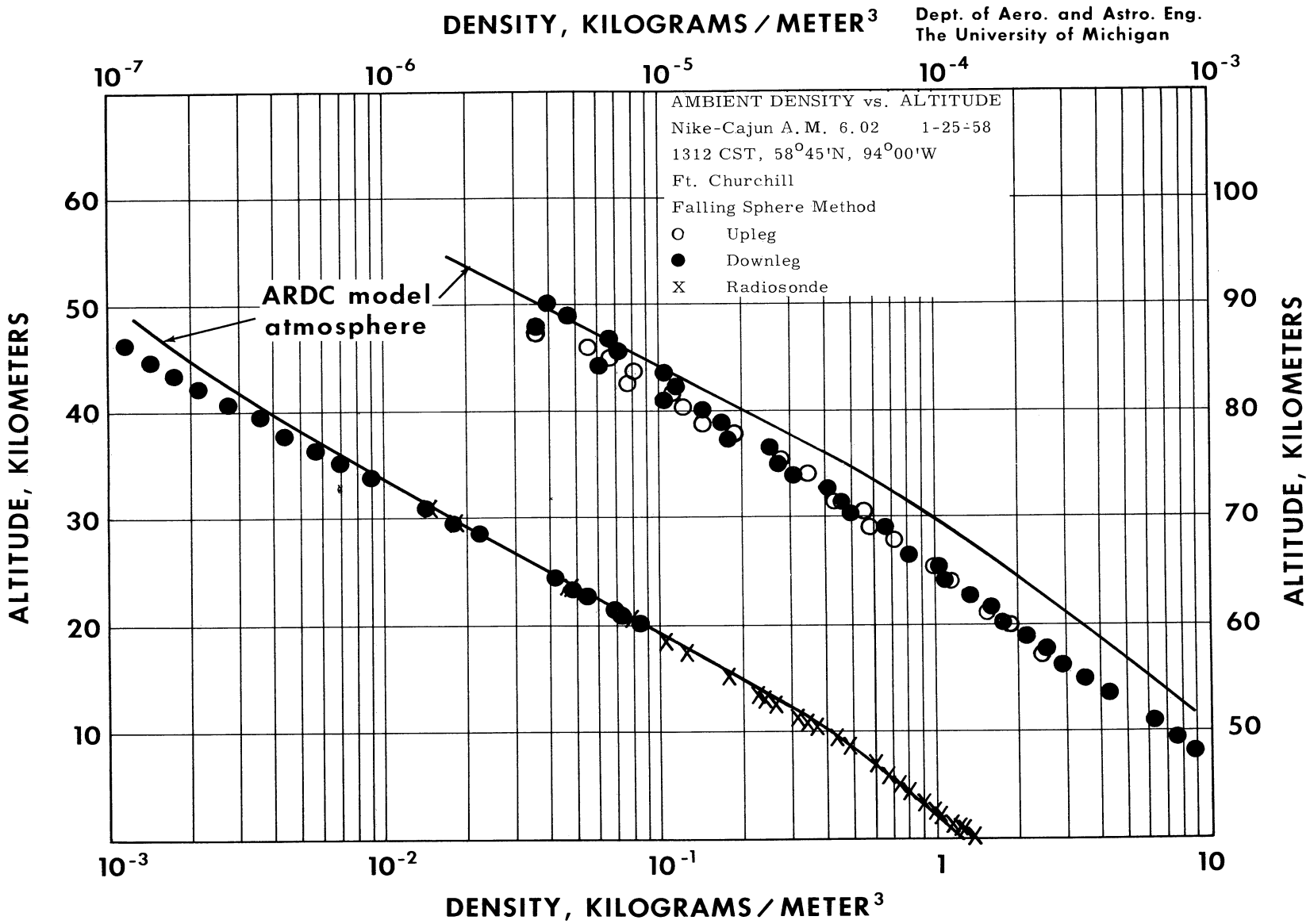

Fig. 56. Ambient density vs. altitude (AM 6.02).

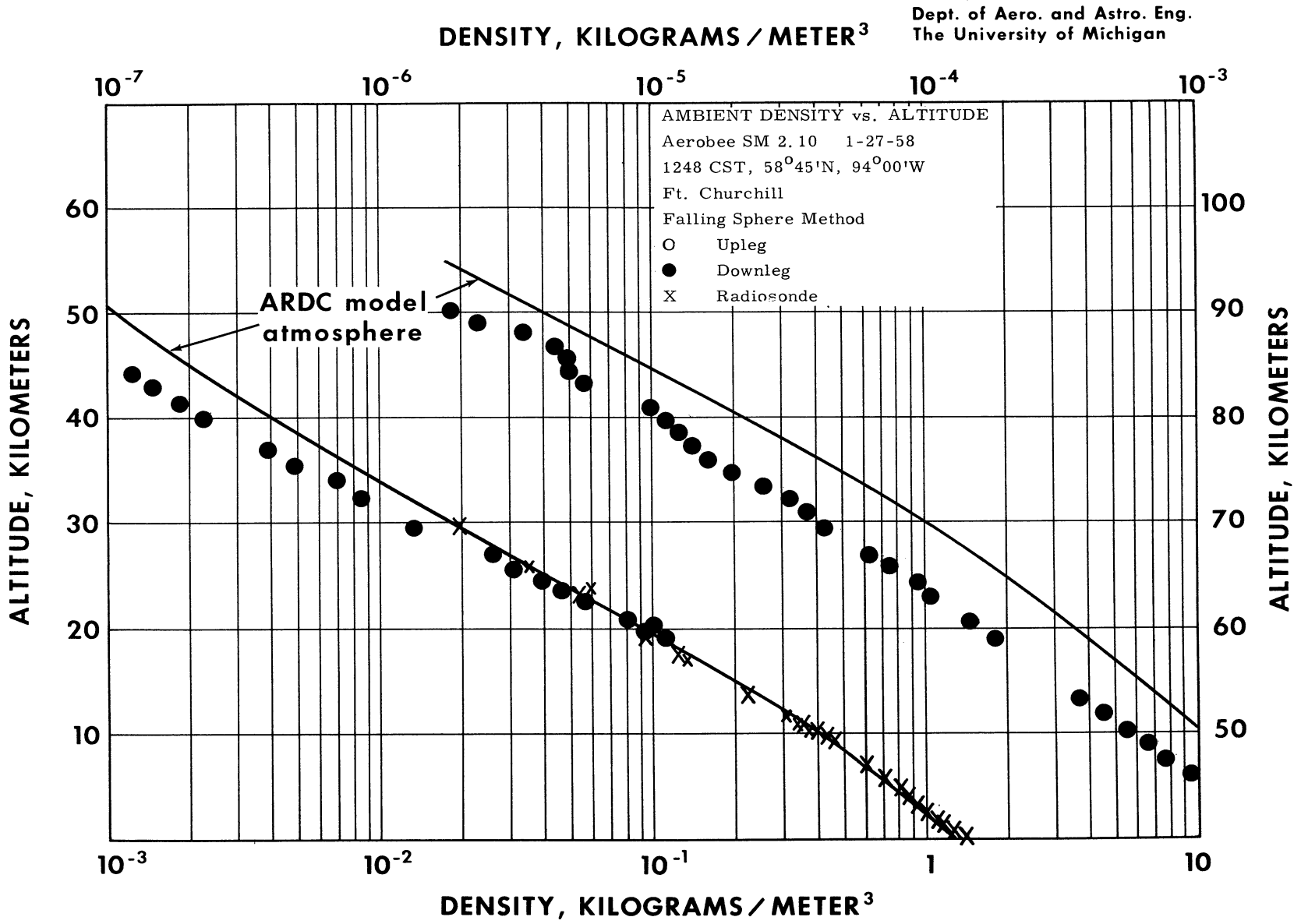

Fig. 57. Ambient density vs. altitude (SM 2.10).

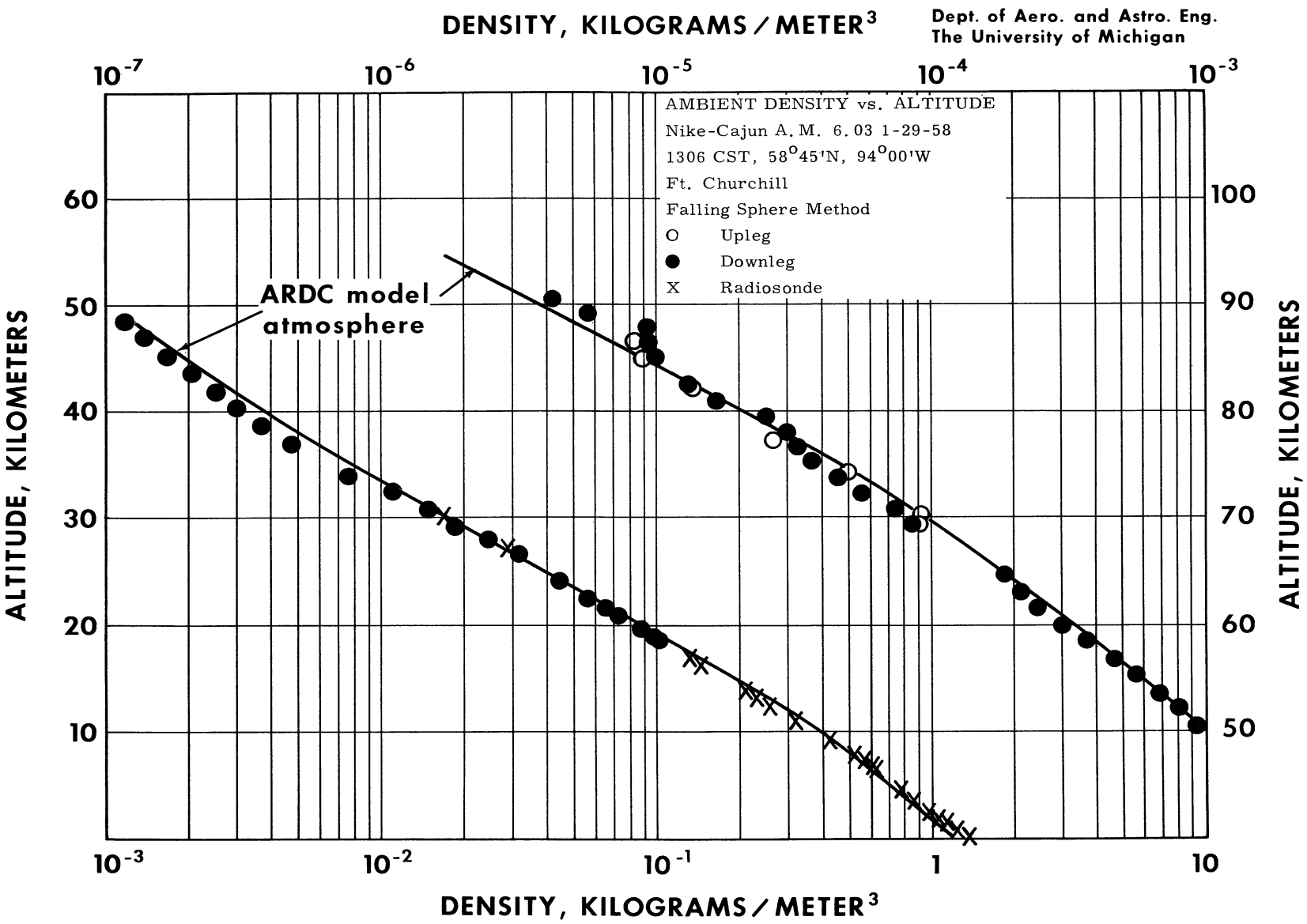

Fig. 58. Ambient density vs. altitude (AM 6.03).

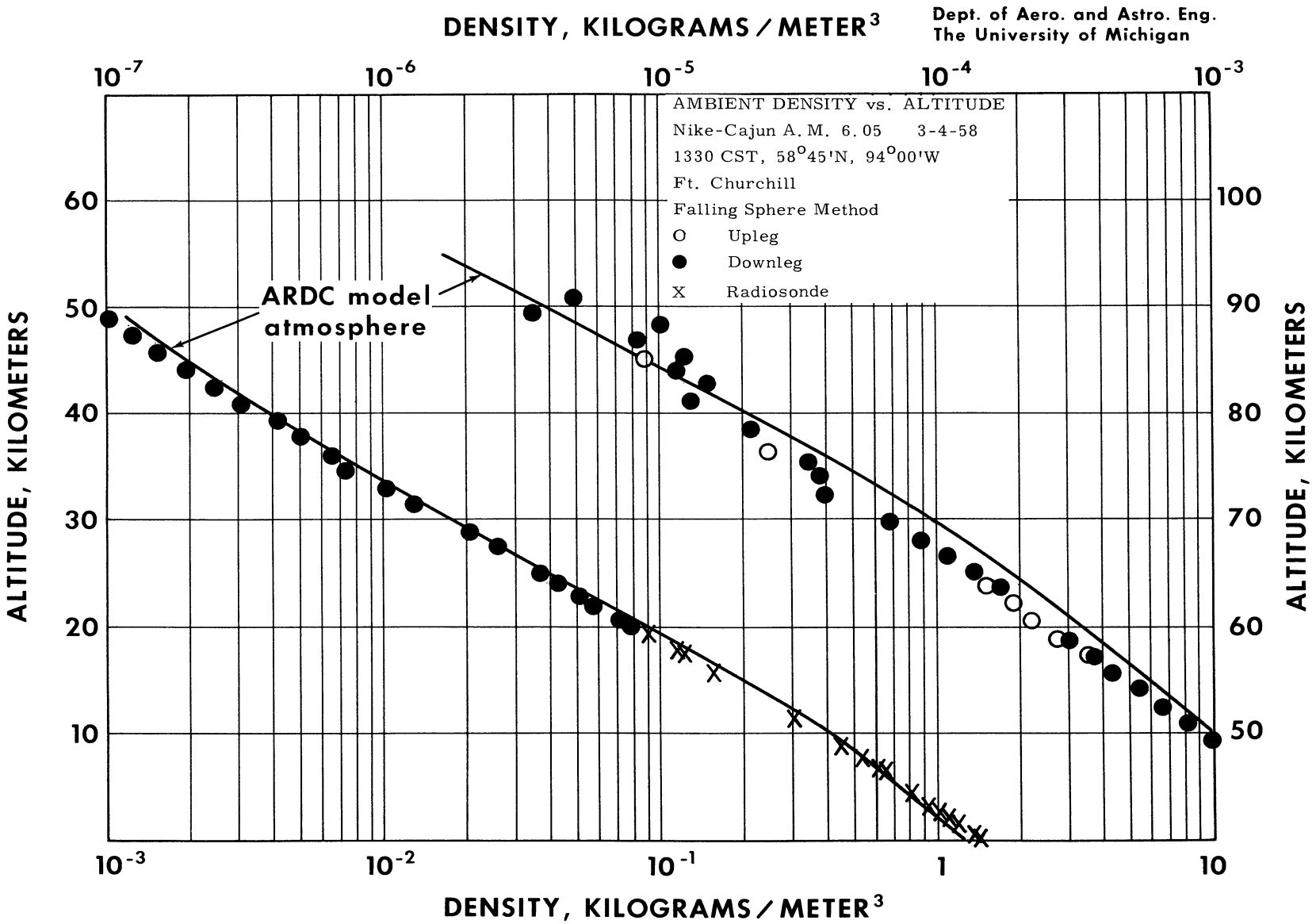

Fig. 59. Ambient density vs. altitude (AM 6.05).

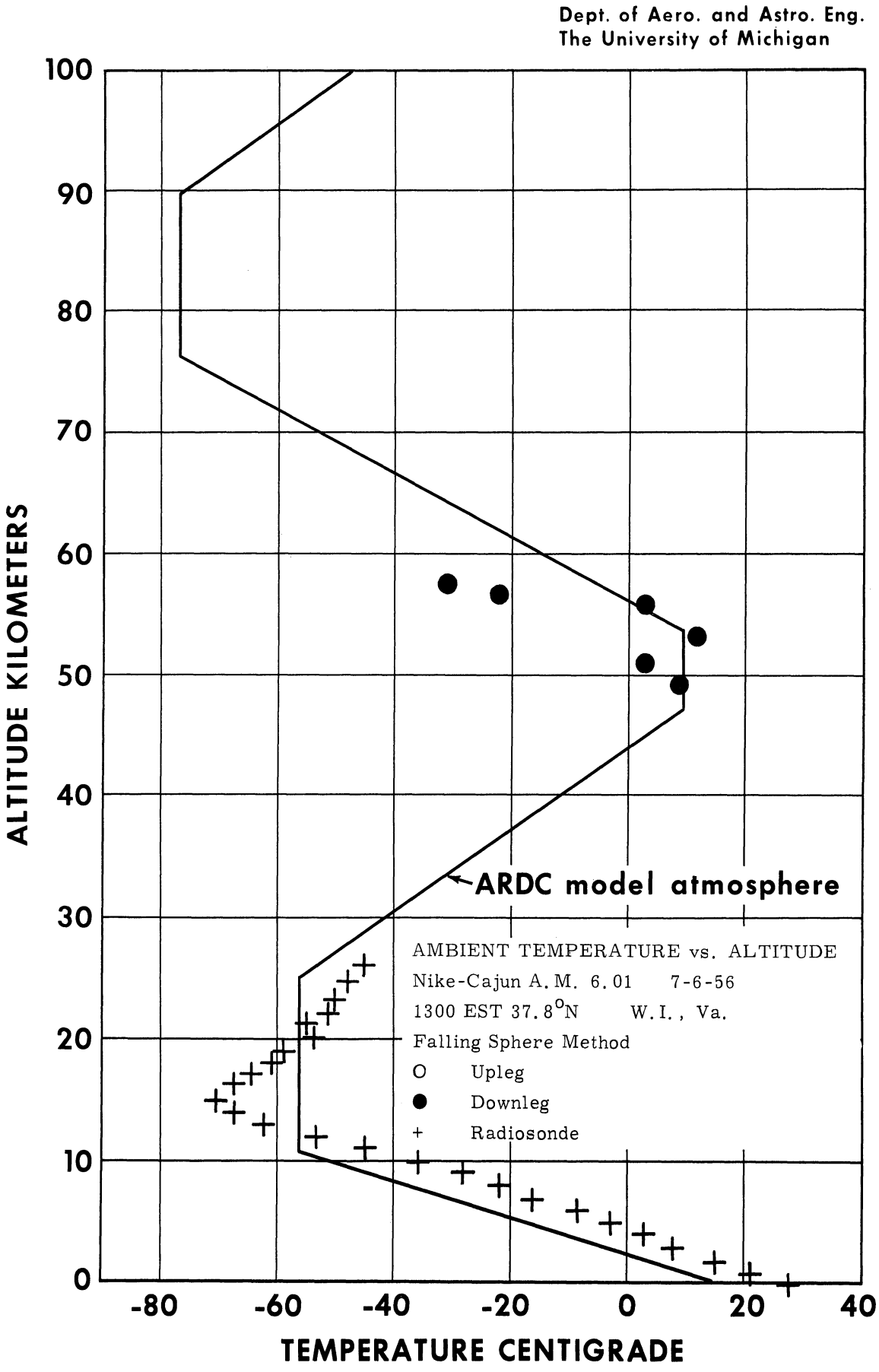

Fig. 60. Ambient temperature vs. altitude (AM 6.01).

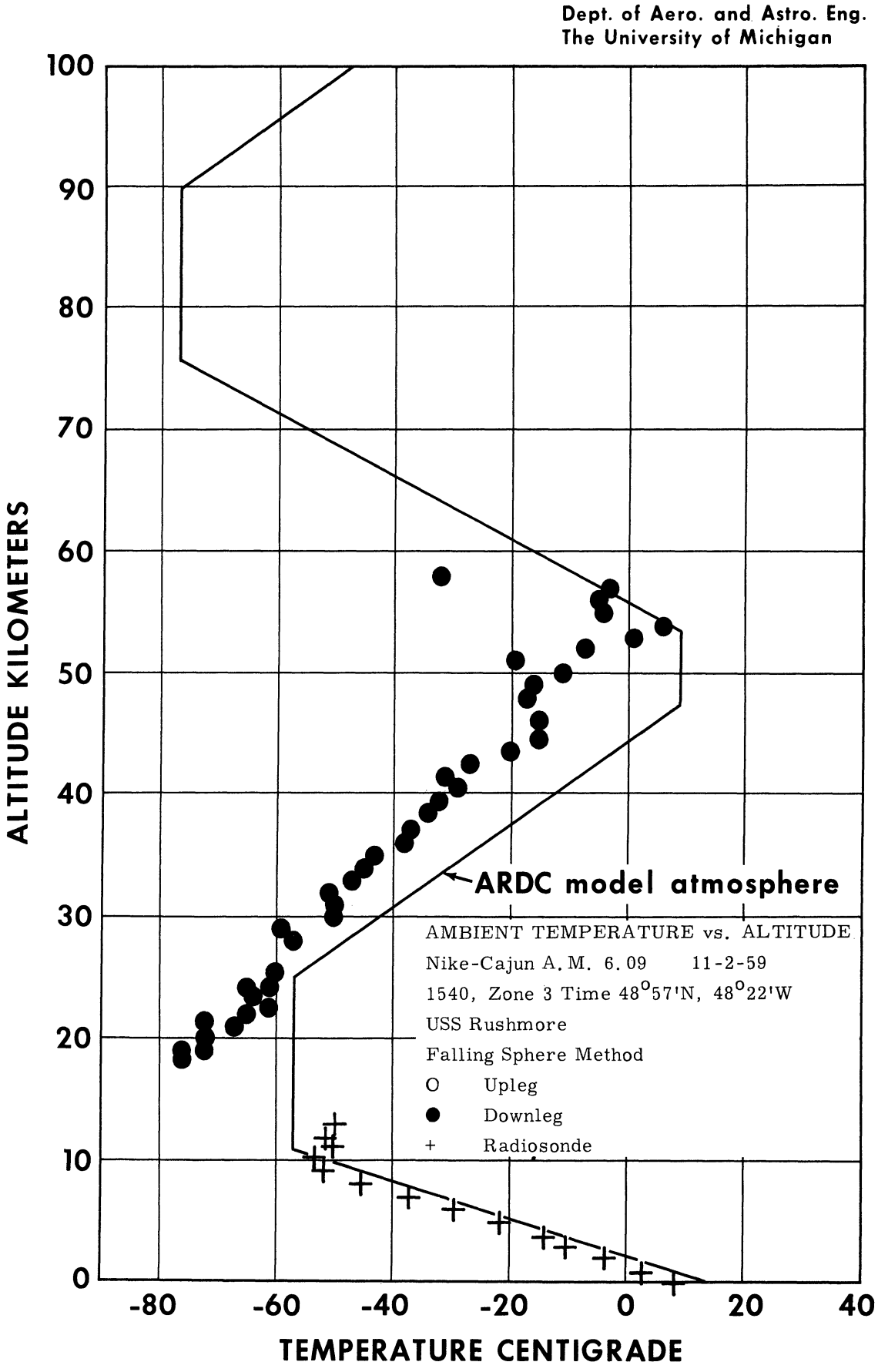

Fig. 61. Ambient temperature vs. altitude (AM 6.09).

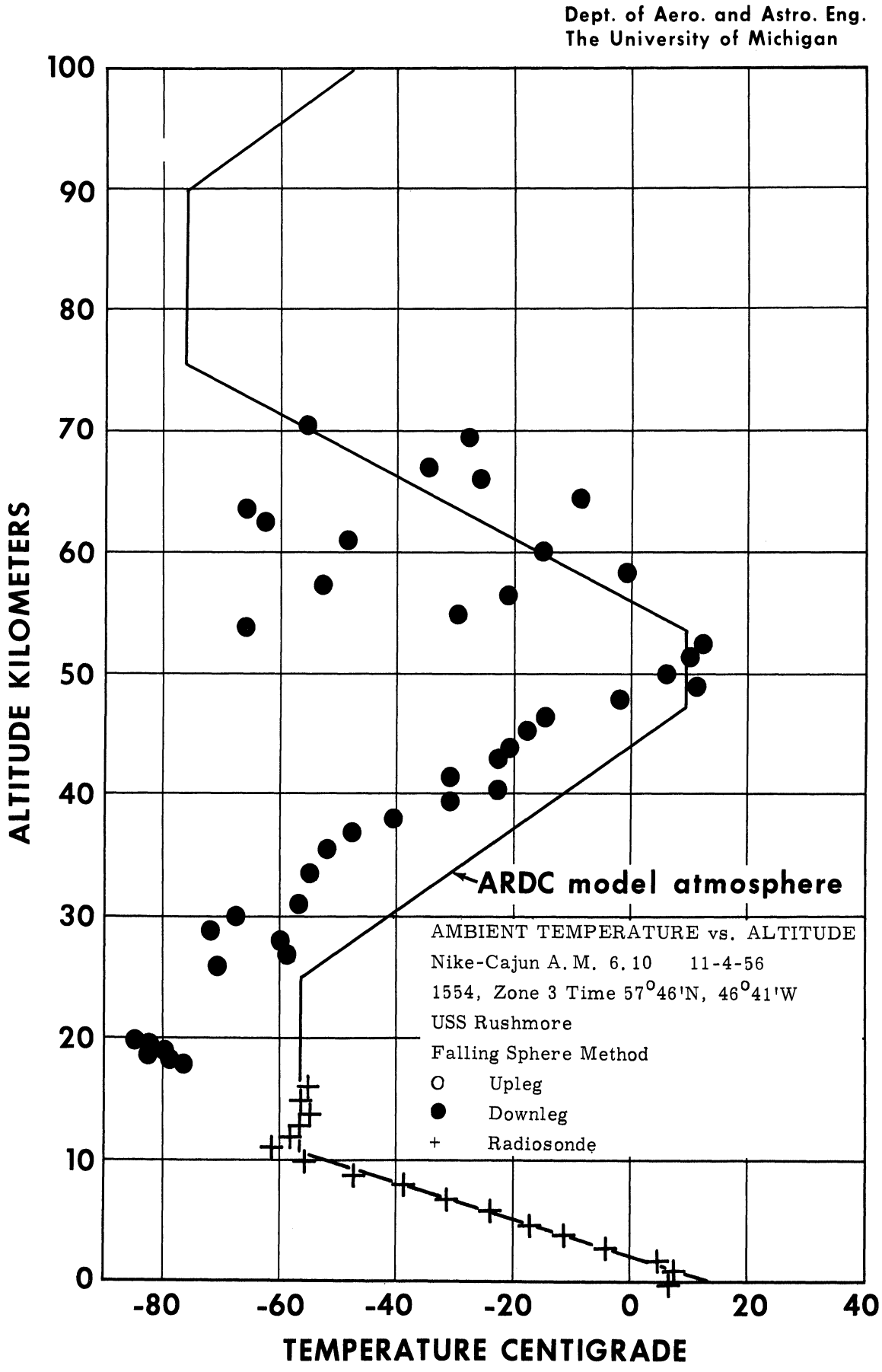

Fig. 62. Ambient temperature vs. altitude (AM 6.10).

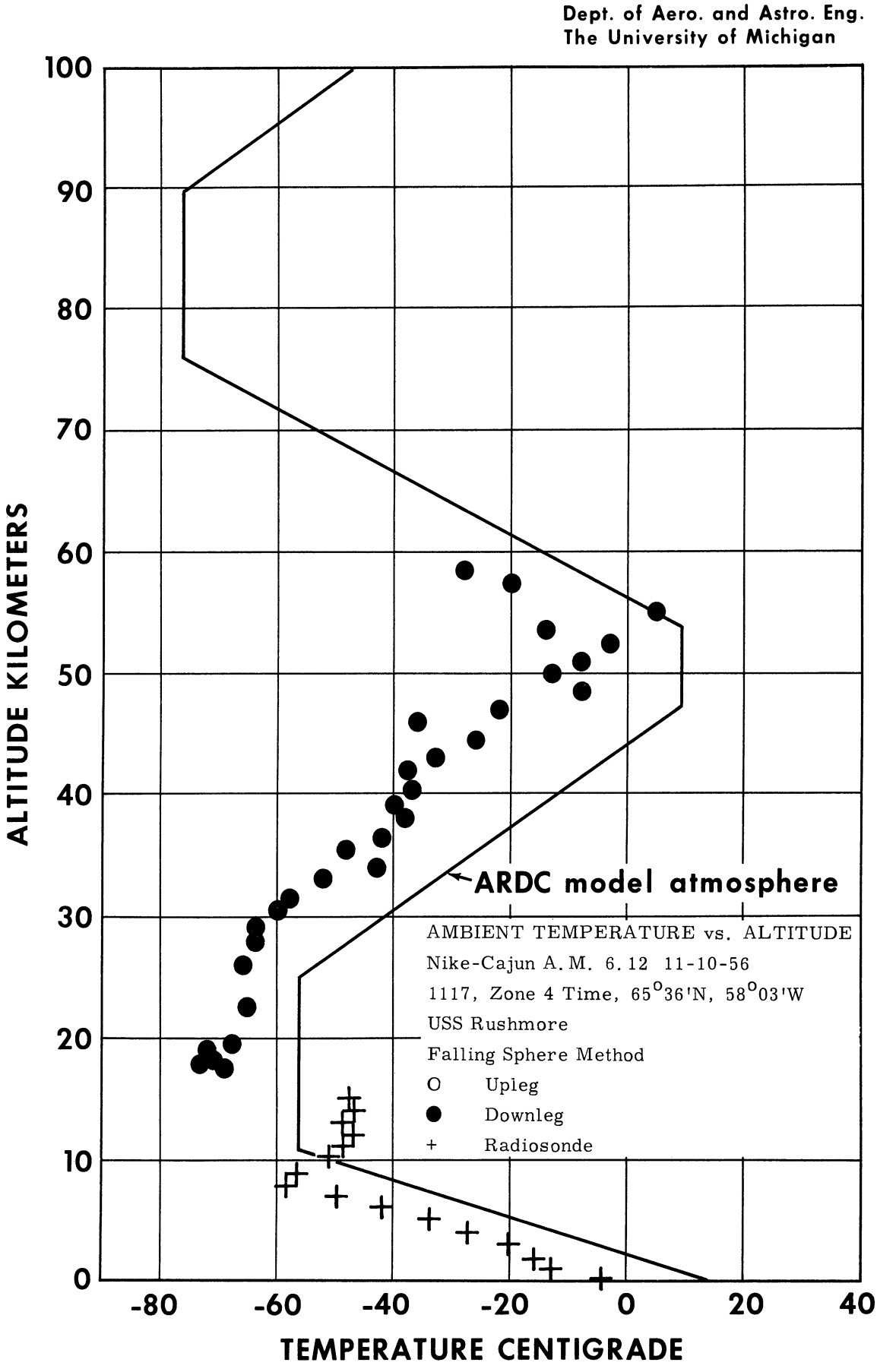

Fig. 63. Ambient temperature vs. altitude (AM 6.12).

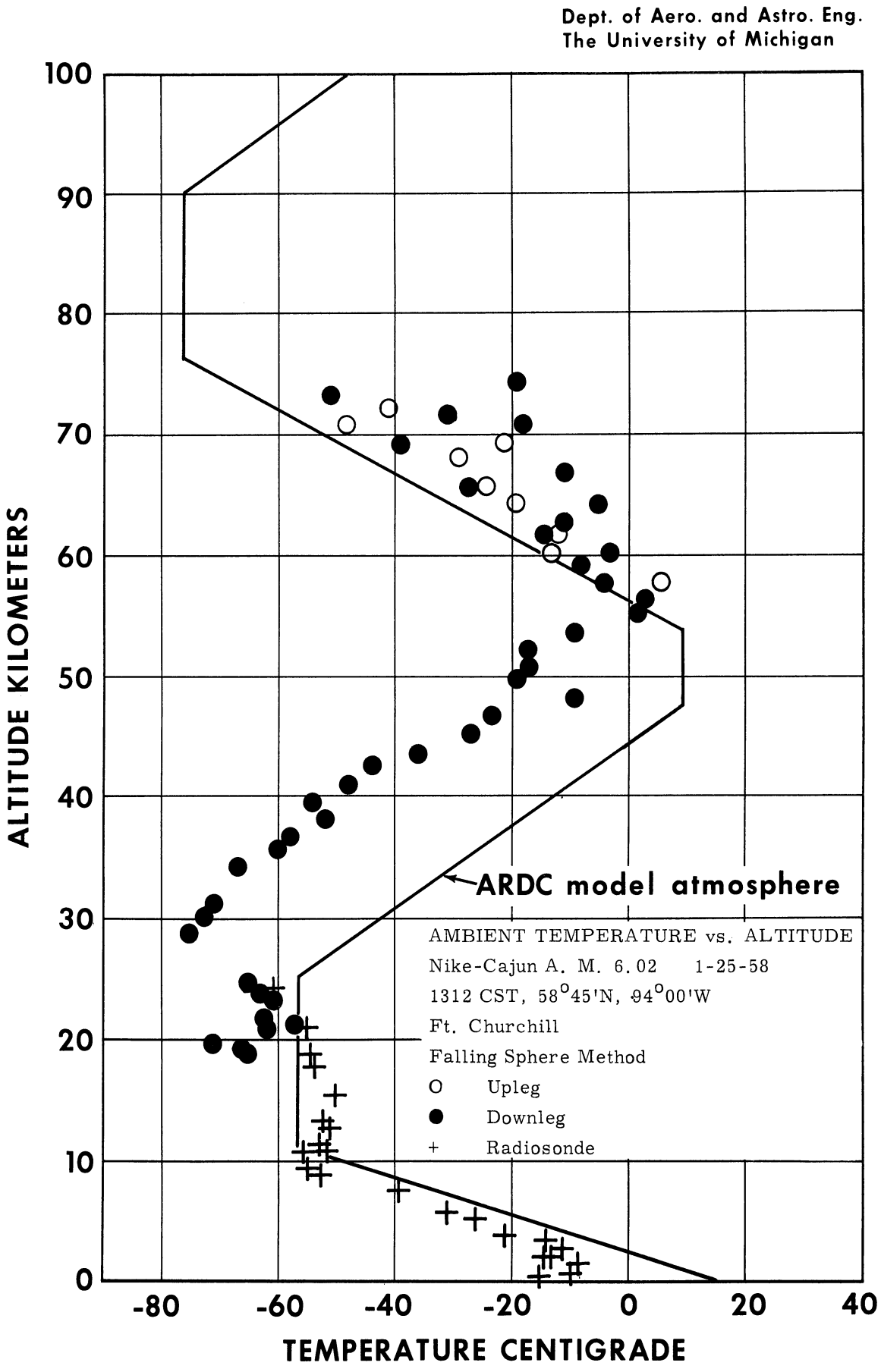

Fig. 64. Ambient temperature vs. altitude (AM 6.02).

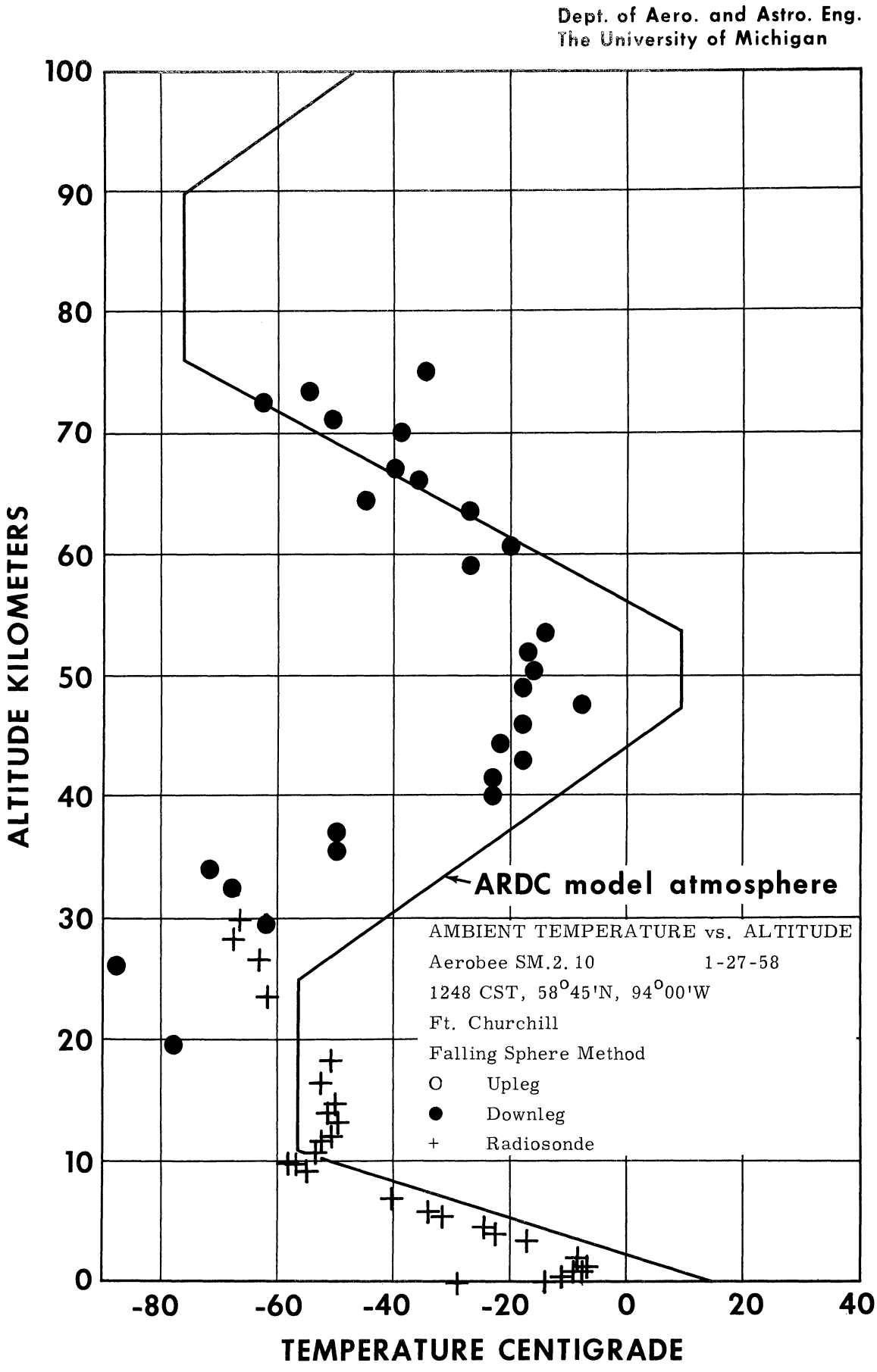

Fig. 65. Ambient temperature vs. altitude (SM 2.10).

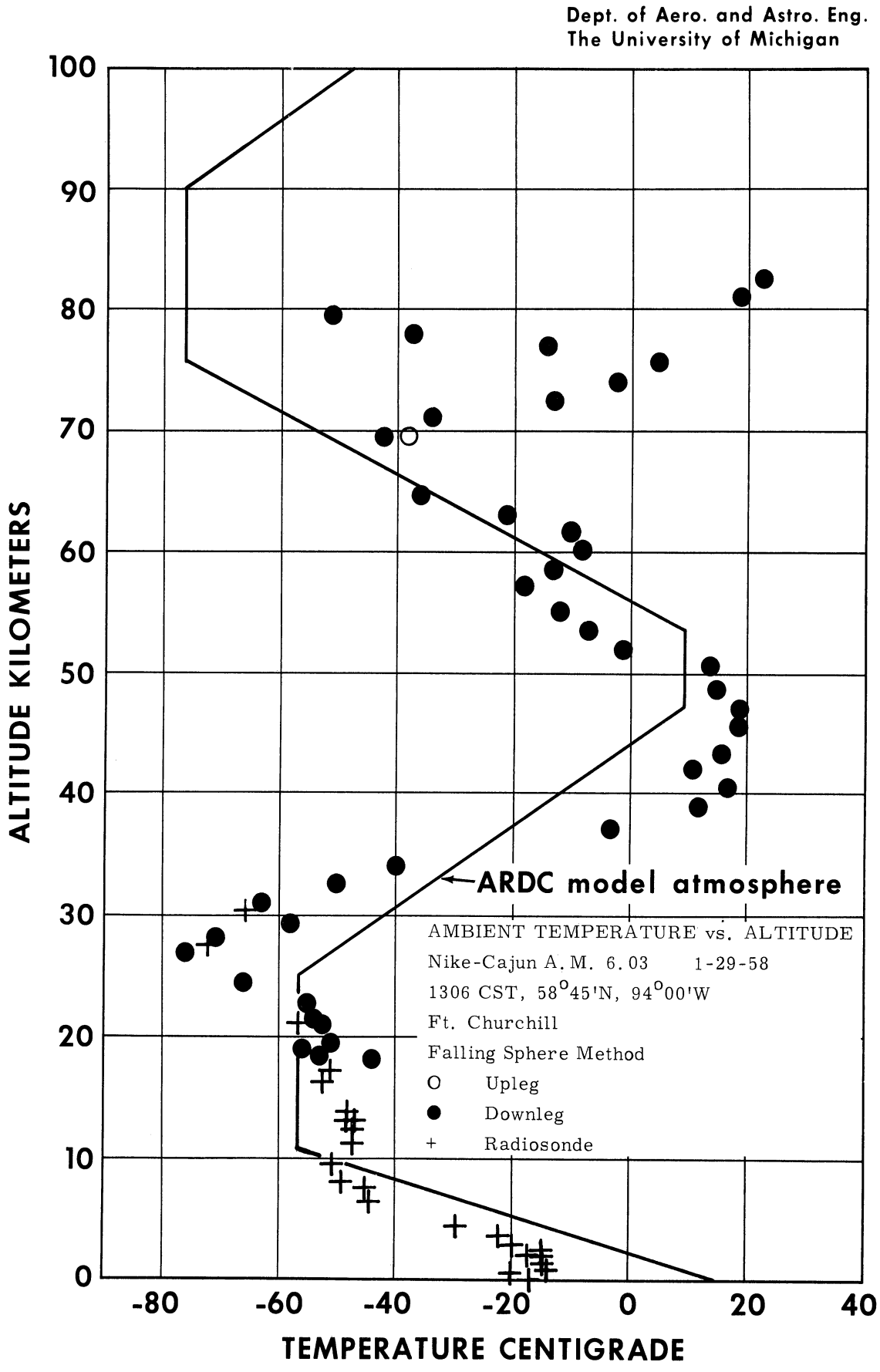

Fig. 66. Ambient temperature vs. altitude (AM 6.03).

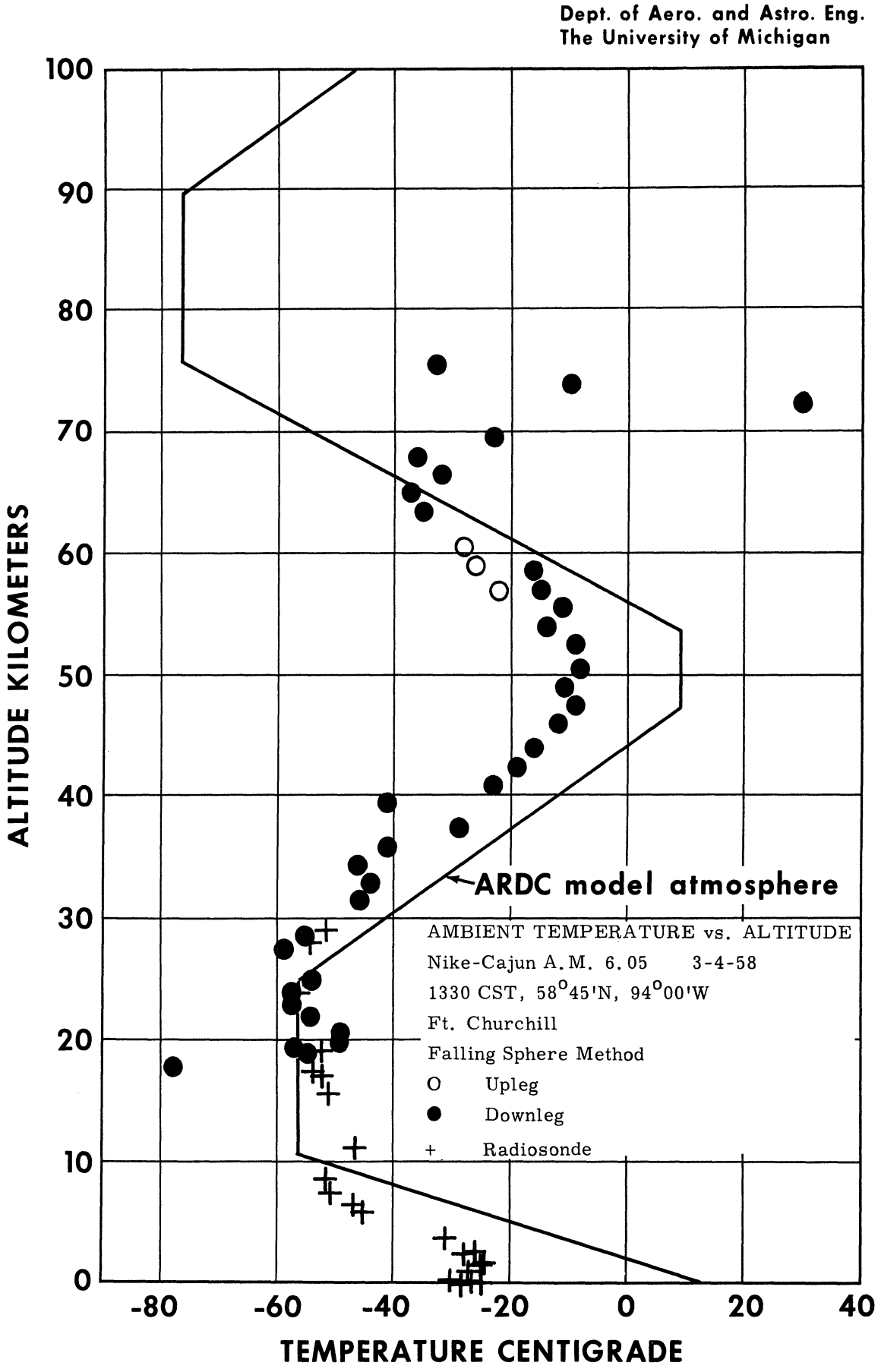

Fig. 67. Ambient temperature vs. altitude (AM 6.05).

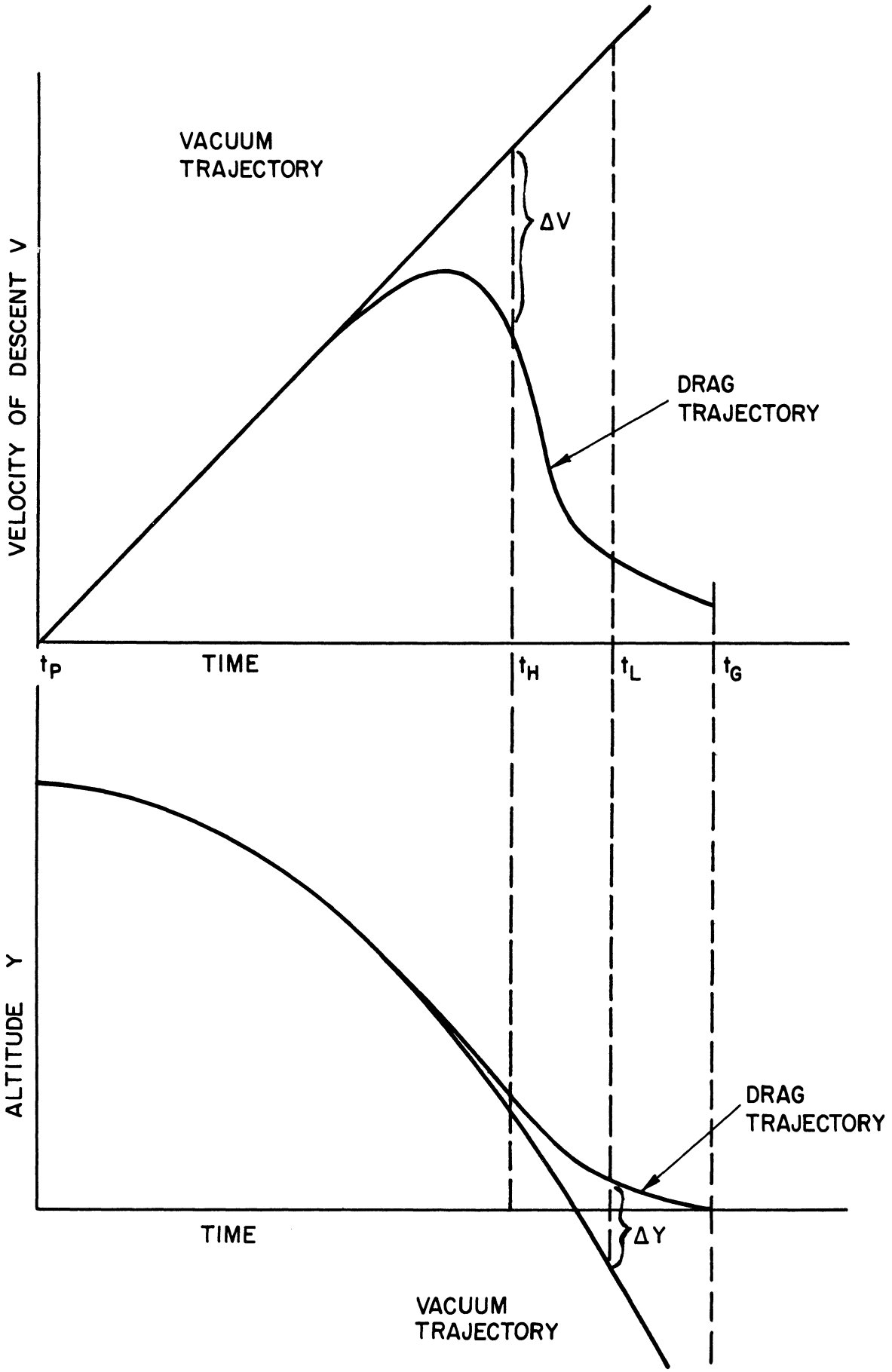

Fig. 68. Typical sphere trajectories compared with vacuum trajectories.

TABLE XI

SUMMARY OF ACCELEROMETER ERROR CALCULATIONS

Parameter	AM 6.09	AM 6.10	AM 6.12	AM 6.02	AM 6.03	AM 6.05
Peak time	176.27	199.70	195.79	191.60	199.85	208.85
Peak altitude, ft	430,600	551,200	529,300	515,100	556,800	593,600
Radiosonde altitude, ft	41,700	52,200	50,100	101,800	98,800	96,100
Time of radiosonde altitude	362.28	393.74	384.12	356.14	373.61	390.28
ΔV ft/sec	5,100	5,300	5,000	860	1,090	1,310
ΔY ft	149,000	83,000	70,000	4,200	5,800	6,600
Accelerometer error assumed	1%	2%	2%	1%	1%	1%
Velocity error, ft/sec	51	106	100	9	11	13
Altitude error, ft	1,490	1,660	1,400	42	58	66

UNIVERSITY OF MICHIGAN
3 9015 03023 7047